

UNIVERSIDADE DE SÃO PAULO

Faculdade de Filosofia, Ciências e Letras de Ribeirão Preto

Departamento de Física

Felipe Rodrigues Barreto

**O acoplamento neurovascular e metabólico do córtex
visual ativado de sujeitos jovens saudáveis durante a
disponibilidade reduzida de oxigênio**

Ribeirão Preto – SP

2016

Felipe Rodrigues Barreto

O acoplamento neurovascular e metabólico do córtex visual ativado de sujeitos jovens saudáveis durante a disponibilidade reduzida de oxigênio

Tese apresentada à Faculdade de Filosofia, Ciências e Letras de Ribeirão Preto da Universidade de São Paulo. Como parte das exigências para a obtenção do título de Doutor em Ciências.

Área de Concentração:

Física Aplicada à Medicina e Biologia

Orientador:

Prof. Dr. Carlos Ernesto Garrido Salmon

Co-orientador:

Profa. Dra. Silvia Mangia

Versão Corrigida

Versão original disponível na FFCLRP

Ribeirão Preto – SP

2016

Autorizo a reprodução e divulgação total ou parcial deste trabalho, por qualquer meio convencional ou eletrônico, para fins de estudo e pesquisa, desde que citada à fonte.

FICHA CATALOGRÁFICA

Barreto, Felipe R.

O acoplamento neurovascular e metabólico do córtex visual ativado de sujeitos jovens saudáveis durante a disponibilidade reduzida de oxigênio / Felipe Rodrigues Barreto; orientador Prof. Dr. Carlos Ernesto Garrido Salmon. Ribeirão Preto - SP, 2016.

70 p.:il,

Tese (Doutorado – Programa de Pós-graduação em Física Aplicada à Medicina e Biologia) – Faculdade de Filosofia, Ciências e Letras de Ribeirão Preto da Universidade de São Paulo, 2016.

1. Acoplamento neurovascular; 2. Metabolismo energético; 3. Hipóxia; 4. fMRI; 5. fMRS

Nome: Felipe Rodrigues Barreto

Título: O acoplamento neurovascular e metabólico do córtex visual ativado de sujeitos jovens saudáveis durante a disponibilidade reduzida de oxigênio

Tese apresentada à Faculdade de Filosofia, Ciências e Letras de Ribeirão Preto da Universidade de São Paulo, como parte das exigências para a obtenção de Doutor em Ciências.

Aprovado em: ____/____/____.

Banca Examinadora

Prof. Dr.: _____ Instituição: _____

Julgamento: _____ Assinatura: _____

Prof. Dr.: _____ Instituição: _____

Julgamento: _____ Assinatura: _____

Prof. Dr.: _____ Instituição: _____

Julgamento: _____ Assinatura: _____

Prof. Dr.: _____ Instituição: _____

Julgamento: _____ Assinatura: _____

Prof. Dr.: _____ Instituição: _____

Julgamento: _____ Assinatura: _____

Dedico este trabalho aos meus pais, Maria Inêz e Joaquim, por todo o apoio e motivação incondicionais neste e em muitos outros passos de minha jornada.

AGRADECIMENTOS / ACKNOWLEDGEMENTS

Ao meu orientador Prof. Carlos Garrido, que desde o primeiro projeto de iniciação científica em 2008 sempre demonstrou uma enorme disposição em transmitir ensinamentos e contribuir para minha formação acadêmica. Obrigado por todo conhecimento e confiança que depositou em mim ao longo destes anos.

To my co-mentor Prof. Silvia Mangia, my deepest gratitude for accepting and supporting me for one year at CMRR. To work in one of the best NMR research facilities in the world was a fantastic experience and an amazing opportunity to enrich my thesis and career. Thanks for all the discussions and encouraging me to always push further.

To Petr Bednařík, for his endless patience and always being available to provide assistance, from teaching me how to operate the scanner all the way to sharing the know-how of fMRS data analysis. Thanks for your guidance and it was a great pleasure to work with you!

To our collaborators from the School of Kinesiology, Donald Dengel and Nicholas Evanoff, for embracing the idea of using RespirAct to generate hypoxia. Your participation and commitment were essential for the execution of the MRS study, and your good humor and disposition always made scanning sessions much more fun.

To the spectroscopy group from CMRR, which includes Ivan Tkac and his invaluable knowledge on MRS, Dinesh for all technical assistance, Gülin Oz and Pierre-Gilles Henry for the early discussion of the experiments and results. In addition, all colleagues from CMRR present in my routine and made my stay at Minneapolis enjoyable.

Ao pessoal da Ressonância do Hospital das Clínicas da Faculdade de Medicina de Ribeirão Preto: Prof. Antônio Carlos e Luciana pela flexibilidade e disponibilidade nos agendamentos das sessões; e Luciano, Mario, Leo, Natália, Adriana e Carol pela assistência durante a realização dos experimentos. Em especial, agradeço a Cecílio pela assistência na montagem experimental para a distribuição dos gases.

Agradeço aos meus amigos e colegas do laboratório InBrain, tanto os de longa data (Marcio, Brunão, Thiago, Kelley e Fabi) e também os de mais curta data: Jeam, Gustavo, Luciana, Prof. Renata Leoni, Maira, Bruno, Cassiano, Ícaro, Carlo e Milton por todos os momentos compartilhados. Em especial, agradeço o amigo Danilo Maziero pela amizade e companheirismo desde os meus primeiros dias em Ribeirão Preto.

Aos amigos do Departamento de Física, em especial os alunos dos laboratórios Biomag e GIIMUS. Obrigado por tornarem o ambiente trabalho muito mais divertido e saudável, pela participação em diversas sessões de ressonância e pelos diversos projetos paralelos. Aos funcionários da secretaria do departamento, pela assistência em diversos assuntos ao longo destes quatro anos de doutorado.

Por último e não menos importantes, agradeço aos meus pais, Maria Inêz e Joaquim. Obrigado por me apoiarem em cada desafio que escolhi enfrentar. Por toda compreensão e por entenderem o motivo de minha ausência em diversos momentos nesses quase nove anos de Ribeirão Preto que se passaram. Agradeço também minha namorada Lais, por todo companheirismo, suporte e carinho, mesmo que muitas vezes a distância.

RESUMO

Barreto, Felipe R. **O acoplamento neurovascular e metabólico do córtex visual ativado de sujeitos jovens saudáveis durante a disponibilidade reduzida de oxigênio.** 2016. 68 f. Tese (Doutorado – Programa de Pós-graduação em Física Aplicada à Medicina e Biologia) – Faculdade de Filosofia, Ciências e Letras de Ribeirão Preto, Universidade de São Paulo, Ribeirão Preto – SP, 2016.

O tecido cerebral é altamente dependente de uma complexa rede vascular e um suprimento adequado de oxigênio, uma vez que o metabolismo oxidativo é a principal via de produção de ATP. Entretanto, durante o aumento da atividade neuronal existe uma relação não linear entre fluxo sanguíneo cerebral e consumo de oxigênio, verificado por tomografia de emissão de pósitrons e posteriormente por técnicas quantitativas de ressonância magnética nuclear. O aumento mais pronunciado do fluxo sanguíneo em comparação com o consumo de oxigênio levanta questões sobre a possibilidade de o oxigênio atuar como um fator limitante. Apesar dos efeitos devastadores da privação completa de oxigênio ao tecido cerebral dentro de minutos, a redução da disponibilidade de oxigênio por curtos períodos de tempo é comum em pacientes com apneia do sono e está associada como fator de risco à hipertensão e acidentes vasculares. Acreditamos que a obtenção de novas informações sobre o efeito da disponibilidade de oxigênio na regulação da resposta vascular e do metabolismo energético no cérebro humano *in vivo* é crucial para um melhor entendimento de aspectos básicos do metabolismo energético cerebral e sua relação com o sistema neurovascular. Nesta tese foi avaliado o impacto da redução da disponibilidade de oxigênio no acoplamento neurovascular e metabólico do cérebro humano saudável. Dois estudos foram realizados na presença de hipóxia moderada, com saturação sanguínea entre 80 a 85%, e normóxia como condição de controle. O primeiro utilizou técnicas quantitativas de ressonância magnética funcional (*fMRI*) em 3T para caracterizar a resposta vascular evocada de 9 sujeitos saudáveis perante a estimulação visual. O segundo visou caracterizar as concentrações metabólicas em repouso e também as alterações induzidas pela estimulação visual em 11 sujeitos, utilizando a técnica de espectroscopia de ressonância magnética funcional (*fMRS*) em 7T. Os dados de *fMRI* mostraram reduções significativas das áreas corticais recrutadas durante a hipóxia moderada, embora as áreas comuns às três

técnicas que continuaram ativas demonstraram respostas com amplitude de fluxo e volume sanguíneos similares a normoxia. Além disto, a variação de consumo de oxigênio devido à estimulação visual foi menor durante a hipóxia. Tais achados potencialmente poderiam indicar diminuição da extensão do recrutamento neuronal, porém um novo desacoplamento entre atividade neuronal e a resposta vascular, ou seja, aumento da atividade neuronal sem uma mesma resposta vascular durante a hipóxia moderada não poderia ser descartado. O estudo de *fMRS* demonstrou alterações metabólicas (glutamato e lactato) induzidas pela estimulação similares em ambas as condições gasosas. Entretanto, alterações significativas nas concentrações de aspartato, glutamato e glutamina foram observadas entre as condições no repouso. A combinação dos achados de ambos os estudos aqui apresentados sugere que a hipóxia moderada não resulta na diminuição do recrutamento neuronal, pois variações similares de glutamato e lactato, considerados fortes marcadores do aumento de atividade neuronal, foram observadas durante hipóxia moderada. Entretanto, há evidências de que a disponibilidade reduzida de oxigênio leva a alterações no mecanismo do acoplamento vascular e também no metabolismo basal. Análises futuras serão necessárias para verificar se existe um mecanismo fisiológico que explica as alterações vasculares e metabólicas aqui observadas.

Palavras-chave: 1. Acoplamento neurovascular; 2. Metabolismo energético; 3. Hipóxia; 4. fMRI; 5. fMRS.

ABSTRACT

Barreto, Felipe R. **The neurovascular and metabolic coupling of activated visual cortex in healthy young adult subjects during reduced oxygen availability.** 2016. 68 p. Thesis (PhD – Physics Applied to Medicine and Biology Graduation program) – Faculty of Philosophy, Sciences and Letters of Ribeirao Preto, University of Sao Paulo, Ribeirao Preto – SP, 2016.

The cerebral tissue is highly dependent on a complex vascular network and a tight regulated supply of oxygen, since oxidative metabolism is the primary source of ATP synthesis. Increased neuronal activity leads to a well-established mismatch between CBF and $CMRO_2$, measured by PET and nuclear magnetic resonance techniques. The much larger CBF evoked response as compared to $CMRO_2$ response raises questions about the role played by oxygen as a potential limiting factor. Despite the devastating effects of intense hypoxia to cerebral tissue, moderate oxygen deprivation through short periods of time is frequent in chronic disorders such as obstructive sleep apnea and has been suggested to be a risk factor for morbidities such as hypertension and stroke. Identifying the impact of mild hypoxia on functional brain metabolism in the healthy human brain is a crucial step for understanding basics aspects of cerebral bioenergetics and its relationship with the neurovascular system. In this thesis we evaluate the impact of reduced oxygen availability in the neurovascular and metabolic coupling of the healthy human brain. Two studies were performed in the presence of mild hypoxia, with 80 to 85% arterial blood oxygen saturation, and normoxia as the control condition. The first study utilized functional Magnetic Resonance Imaging techniques (fMRI) at 3T to characterize the vascular response to visual stimulation in 9 subjects. The second study aimed at characterizing the neurochemical profile of the human brain and quantifying the stimulus-induced metabolic changes as measured by fMRS at 7T in 11 subjects. The fMRI data showed significant reductions in the recruited cortical areas during mild hypoxia, although activated areas in all three imaging modalities showed responses with similar amplitude of blood flow and volume from normoxia. In addition, the variation of oxygen consumption due to stimulation was smaller during mild hypoxia. These findings could potentially suggest

decreased neuronal recruitment, although a new decoupling between neuronal activity and vascular response (i.e. similar neuronal recruitment with different vascular response) could not be discarded. The fMRS study showed similar stimulus-induced glutamate and lactate changes during both gas conditions. However, significant concentration differences were observed in aspartate, glutamate and glutamine during rest conditions. Finally, the combination of the data from the two studies herein presented suggests that mild hypoxia does not result in reduced neuronal recruitment despite the altered vascular response, as shown by the similar glutamate and lactate stimulus-induced responses, known to be strong markers of increased neuronal activity. However, there are evidences that support altered neurovascular coupling and metabolic concentrations during reduced oxygen availability at rest. Further analysis will be necessary to elucidate how the new steady state concentrations of aspartate, glutamate and glutamine could be linked to physiological mechanism that potentially alters the neurovascular response.

Key-words: 1. Neurovascular coupling; 2. Energetic metabolism; 3. Hypoxia; 4. fMRI; 5. fMRS.

LIST OF FIGURES

Fig. 1.1. Description of dynamic physiology changes induced by increased neuronal activity. Adapted from Buxton et al. (2004).....	2
Fig. 2.1. Schematic representation of a cell and main energetic pathways distribution.....	10
Fig. 3.1. Graphical representation of an estimate of temporal/spatial resolution and degree of invasiveness of different techniques that allow the functional study of the central nervous system or its components. MEG: magnetoencephalography; ERP: event-related potential from EEG measurements; PET positron emission tomography; 2-deoxyglucose: a specific tracer for PET. Adapted from Jezzard et al (2001).....	14
Fig. 3.2. Basic EPI pulse sequence diagram (a) and k-space trajectory generated (b).....	19
Fig. 3.3. Representation of a typical BOLD response to stimulation and its temporal characteristics. The initial dip, the stimulus overshoot and the post stimulus undershoot are often seen features of the BOLD response. Adapted from Jezzard et al. (2001)	21
Figure 3.4. A simplified schematic representation of the events during the acquisition of control and labeled images from ASL and the subtraction for the perfusion weighted image. First line contains the magé label acquisition events, whereas control image is shown in the second line. The third line shows a representation of the subtraction between control and labeled images and an example of perfusion-weighted image. The image slices positioning is represented by white bars; the labeling band is represented as a yellow rectangle in the neck; arrows indicate the spins and those whose magnetization was inverted are painted in red.	27
Fig. 3.5. Schematic representation of a single voxel PRESS pulse sequence.	36
Fig. 3.6. Schematic representation of a single voxel STEAM pulse sequence.	37
Fig. 3.7. Schematic representation of a single voxel Semi-LASER pulse sequence.....	38
Fig. 5.1. Timeline diagram of events during an experimental session after subject positioning in the scanner.....	45
Fig. 5.2. BOLD, ASL and VASO images from a subject in normoxia.	49
Fig. 5.3. Example of activation masks from BOLD, ASL and VASO from a single subject during normoxia (blue), mild hypoxia (red) and the overlap between areas (pink). Note that the hypoxia mask is almost entirely contained within normoxia mask, and red areas are practically absent.....	49

Fig. 5.4. Time courses of BOLD (N=9), CBF (N=9) and CBV (N=7) from the overlapping area between the 3 techniques for each gas condition averaged across trials and subjects. Data shown as mean \pm standard deviation. Areas in gray represent periods of stimulation 50

Fig. 6.1. Representation of VOI positioning in the occipital lobe..... 58

Fig. 6.2. Timeline diagram of events during an experimental session. 59

Fig. 6.3. Example of mean water peaks from a single subject exhibiting different linewidths due to BOLD and susceptibility effects generated by mild hypoxia during normoxia at rest (normREST), normoxia during visual stimulation (normSTIM), mild hypoxia at rest (hypREST) and mild hypoxia during visual stimulation (hypSTIM)..... 62

Fig. 6.4. LCModel quantification of a typical representative spectra from normoxia 63

Fig. 6.5. Example of spectra acquired at normoxia during rest (normREST, in blue) and during mild hypoxia at rest (hypREST, in red) from a single subject. LCModel analysis of the difference spectrum (N=10, normREST – hypREST, in cyan), LCModel fit components: aspartate (Asp, red), glutamine (Gln, orange) and glutamate (Glu, black). Fit residue (green). Concentrations are given as mean \pm CRLB. Gaussian filter ($\sigma=0.15$ Hz) was applied on the difference spectrum and fit residue for display purposes. 64

Fig. 6.6. Average metabolic concentrations during fMRS paradigm over subjects (N=11). P-values were calculated using paired two-tailed t-test. Error bars represent the standard deviation. Asp, aspartate; Glc, glucose; Glu, glutamate; Gln, glutamine; Lac, lactate. NormREST, mild hypoxia during normoxia at rest; NormSTIM, normoxia during visual stimulation; HypREST, mild hypoxia at rest; HypSTIM, mild hypoxia during visual stimulation. 66

Fig. 6.7. LCModel analysis of the difference spectrum (STIM - REST) from normoxia (A) and mild hypoxia (B). From top to bottom: difference spectrum (blue) to be fitted in LCModel. LCModel fitted components: aspartate (red), glucose (green), glutamate (black), lactate (magenta) and the fit residue (cyan). Concentrations given as mean \pm CRLB. Gaussian filter ($\sigma=0.15$ Hz) was applied on the difference spectrum and the residue for display purposes. 67

LIST OF TABLES

Table 5.1. Constants used in Lu et al. (2004) methodology for CMRO ₂ calculation.....	47
Table 5.2. Amplitude of evoked vascular changes due to visual stimulation	50
Table 6.1. Absolute metabolic concentrations during baseline	63
Table 6.2. Absolute metabolic concentration differences (STIM-REST) due to stimulation	65

ABBREVIATIONS

ADP	Adenosine Diphosphate
ATP	Adenosine Triphosphate
AFP	Adiabatic Full Passage
AMARES	Advanced Method for Accurate, Robust and Efficient Spectral Fitting
ASL	Arterial Spin Labeling
ATP	Adenosine Triphosphate
BOLD	Blood Oxygenation Level Dependent
CASL	Continuous Arterial Spin Labeling
CBF	Cerebral Blood Flow
CBV	Cerebral Blood Volume
CK	Creatine Kinase
CMR _{Glc}	Cerebral Metabolic Rate for Glucose
CMRO ₂	Cerebral Metabolic Rate for O ₂
CNR	Contrast-to-Noise
EEG	Electroencephalography
EPI	Echo Planar Imaging
EPISTAR	Echo Planar Imaging and Signal Targeting with Alternating Radiofrequency
FID	Free Induction Decay
fMRI	Functional Magnetic Resonance Imaging
fMRS	Functional Magnetic Resonance Spectroscopy
GABA	γ -Aminobutyric Acid
GE	Gradient Echo
GLM	General Linear Model
IR	Inversion Recovery
MEG	Magnetoencephalography
MNI	Montreal Neurological Institute
MR	Magnetic Resonance

MRI	Magnetic Resonance Imaging
MRS	Magnetic Resonance Spectroscopy
MRUI	Magnetic Resonance User Interface
MT	Magnetization Transfer
NAD	Nicotinamide Adenine Dinucleotide
NADH	Reduced form of Nicotinamide Adenine Dinucleotide
NMR	Nuclear Magnetic Resonance
OEF	Oxygen Extraction Fraction
OVS	Outer Volume Suppression
PASL	Pulse Arterial Spin Labeling
pCASL	Pseudo-continuous Arterial Spin Labeling
PCr	Phosphocreatine
PD	Proton Density
PET	Positron Emission Tomography
P_{ETCO_2}	End-tidal partial pressure of CO_2
P_{ETO_2}	End-tidal partial pressure of O_2
Pi	Inorganic Phosphate
pO_2	Partial Pressure of O_2
PRESS	Point Resolved Spectroscopy
RF	Radiofrequency
SE	Spin Echo
SNR	Signal-to-Noise
STEAM	Stimulated Echo Acquisition Mode
SWI	Susceptibility Weighted Imaging
TCA	Tricarboxylic Acid
TE	Echo Time
TI	Inversion Time
TM	Mixing Time
TR	Repetition Time
VAPOR	Variable Pulse Power and Optimized Relaxation Delays
VASO	Vascular Occupancy Dependent

VOI	Volume of Interest
RR	Respiratory Rate
HR	Heart Rate
CRLB	Cramèr-Rao Lower Bounds

SUMMARY

ABSTRACT	x
LIST OF FIGURES	xii
LIST OF TABLES.....	xiv
ABBREVIATIONS	xv
CHAPTER 1 - THE NEUROVASCULAR COUPLING	1
CHAPTER 2 - ENERGY METABOLISM AND HYPOXIA	6
2.1 Bioenergetics of human brain	6
2.2 Reduced oxygen availability and hypoxia	11
CHAPTER 3 - FUNCTIONAL MRI AND MRS TECHNIQUES FOR BRAIN STUDY ..	14
3.1 Functional experiments.....	14
3.2 A brief introduction to MRI physics.....	16
3.3 Functional MRI: Blood Oxygen Level Dependent contrast	20
3.4 fMRI: Vascular Space Occupancy contrast	23
3.5 Arterial Spin Labeling.....	26
3.6 Oxygen consumption estimation.....	30
3.7 Magnetic Resonance Spectroscopy.....	34
CHAPTER 4 - MOTIVATION AND OBJECTIVES	42
CHAPTER 5 - CHARACTERIZATION OF THE VASCULAR RESPONSE DURING HYPOXIA USING FMRI EXPERIMENTS.....	44
5.1 Methodology.....	44
5.1.1 Participants.....	44
5.1.2 Experimental design.....	44
5.1.3 Data acquisition.....	45

5.1.4 Data analysis	46
5.1.5 Statistical analysis	48
5.2 Results.....	48
5.2.1 Physiological variables.....	48
5.2.2 Functional MRI	48
5.2.3 Quantification of CMRO ₂	50
5.3 Discussion.....	51
5.4 Conclusion	54
CHAPTER 6 - CHARACTERIZATION OF THE METABOLIC RESPONSE DURING HYPOXIA USING FMRS EXPERIMENTS.....	56
6.1 Methodology	56
6.1.1 Participants.....	56
6.1.2 Experimental design.....	56
6.1.3 Data acquisition.....	57
6.1.4 Data analysis	59
6.1.5 Statistical analysis	60
6.2 Results.....	61
6.2.1 Physiological variables.....	61
6.2.2 MRS findings	61
6.3 Discussion.....	67
6.4 Conclusion	69
CHAPTER 7 - CONCLUSIONS AND OUTLOOK.....	70
WORK AND PUBLICATIONS	71
REFERENCES	73
APPENDIX A – ETHICS COMMITTEE APPROVAL – UNIVERSITY OF SÃO PAULO	87

APPENDIX B – ETHICS COMMITTEE APPROVAL – UNIVERSITY OF MINNESOTA 88

APPENDIX C – GRANT AWARD LETTER..... 89

CHAPTER 1 - THE NEUROVASCULAR COUPLING

The human brain is the main organ of the central nervous system and has a high energetic demand. It represents only 2% of the body mass, but it consumes approximately 20% of the total oxygen and 25% of glucose utilized by the body (1). The high energetic cost is mainly generated by excitatory post-synaptic synapses and action potential propagation, which requires 52% and 33% of the total adenosine triphosphate (ATP) produced (2), respectively. Neurotransmitter release and recycling consume 5% and 4% of the produced ATP, respectively (2). Due to the lack of reservoirs for essential nutrients and oxygen, an efficient transport system is crucial for proper brain function (3), which is provided by a complex vascular network responsible for the distribution of nutrients and removal of catabolites through the cerebral blood flow (CBF). Blood vessels, neurons and glial cells forms the so-called “neurovascular unit” (4), which constitutes a functional unit responsible for maintaining homeostasis. The interactions between the components of the neurovascular unit allow CBF distribution through areas according to their activity and metabolic demand. Here we define as the neurovascular coupling the regulatory relationship of neuronal activity through the neurovascular over the vascular system.

The increase in neuronal activity, and consequently in the energetic demand, is followed within 1-2 seconds by a cascade of vascular changes which defined the so-called hemodynamic response, characterized by dynamic changes in CBF and cerebral blood volume (CBV), as shown by theoretical curves in Fig. 1.1. Extra-cerebral arteries at the surface of the brain, such as the pial arteries in the cortex, are the main source of resistance and control the blood flow. The vasodilation in the activation site is associated with dilation in pial arteries for an adequate regulation of perfusion. The vasodilatation propagates from the active area to the surface through the transmission of intramural signals, sustaining pressure equilibrium on the vascular tree that does not allow blood flow to shift from active regions to others also irrigated by the same vessel branch (3).

In 1890, the physiologist Charles Sherrington demonstrated that stimulation of the brain caused a local increase in blood flow (5). Even though it has been known for more than a century that increases in brain activity result into CBF increases, the metabolic mechanisms that govern the relationship between neural activity and blood flow are not

fully understood (6). Among different metabolic changes that are induced by increased neuronal activity, local increase in CO_2 , changes in K^+ , Ca^{2+} and adenosine concentrations are known to be capable of triggering the hemodynamic response (3).

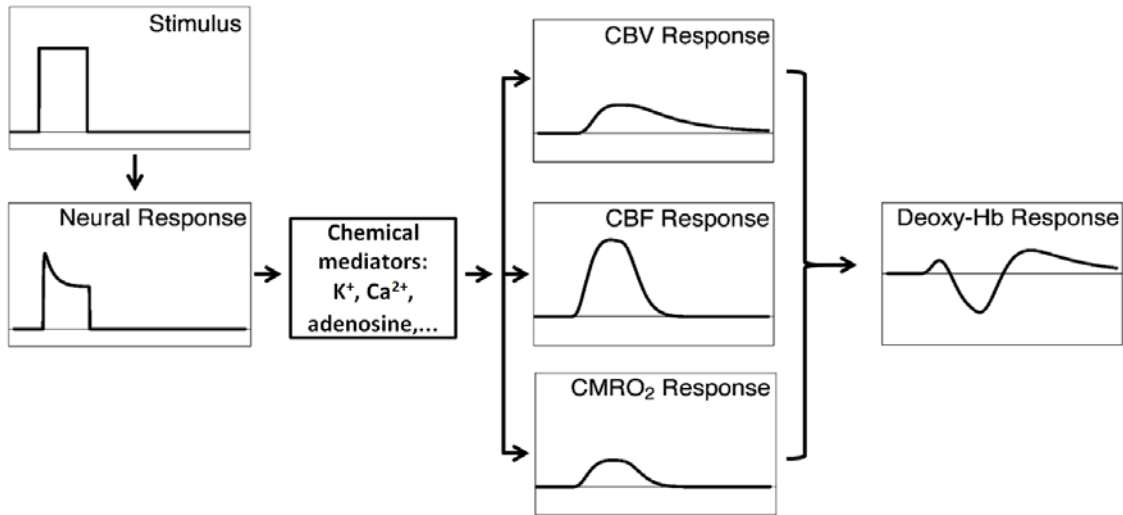


Fig. 1.1. Description of dynamic physiology changes induced by increased neuronal activity.
Adapted from Buxton et al. (2004).

The main function of the hemodynamic response is to deliver essential molecules (e.g. glucose, oxygen, lipids and hormones) and clear waste products through the blood flow. Considering that the adult human brain has a typical basal cerebral metabolic rate for glucose (CMR_{Glc}) of 0.3 mM/min (7) and the concentration of glucose in the cerebral tissue is 2 mM (8), in the event of a complete interruption of nutrient transportation, it would take minutes for total depletion of glucose in the tissue. This basic calculation suggests that the hemodynamic response on the time scale of seconds is not necessary to sustain glucose metabolism (9). However, considering the normal baseline cerebral metabolic ratio for O_2 (CMRO_2) of 1.6 mM/min (10) and a typical O_2 concentration of 0.3 mM in the brain tissue, the time for O_2 depletion is in the same time scale of the hemodynamic response. The relationship between CMRO_2 and O_2 concentrations in the tissue is a strong indication that O_2 availability is the reason why the hemodynamic response is shortly after the increase in neuronal activity. As a matter of fact, glucose availability in the blood has no effect on the CBF response after sustained visual stimulation (11).

The hypothesis that CBF and the CMRO_2 are coupled during rest (here defined as the condition without the presence of a stimulus) is widely accepted, since 80 to 92% of the

ATP consumed in the brain is produced through oxidative metabolism of glucose (11). If the hemodynamic response was directly regulated for supplying the demands of the tissue, a linear relationship between CBF and $CMRO_2$ would be observed during increased neuronal activity (here defined as “activation”). However, Fox et al. (1986, 1988) utilizing Positron Emission Tomography (PET) showed a 30 to 50% increase of CBF in the visual cortex due to visual stimulation, whereas $CMRO_2$ increased 5 to 10%. Subsequent studies using PET and functional Magnetic Resonance Imaging (fMRI) techniques confirmed the mismatch between ΔCBF (30-65%) and $\Delta CMRO_2$ (5-30%) (9,12–19), and there is a consensus that the $\Delta CBF/\Delta CMRO_2$ ratio varies from 2 to 4 among different brain regions (16,20–22). Thus, it is likely that CBF and $CMRO_2$ are not linearly coupled during activation. A recent hypothesis suggests that the CBF increase in response to a stimulus is not driven by the change in energy metabolism, but rather by signals related to the neuronal activity itself (23). Instead of direct link between CBF and $CMRO_2$, Buxton et al. (2010) showed through a theoretical framework that observed $\Delta CBF/\Delta CMRO_2$ coupling ratio is approximately what is required to maintain the partial pressure of O_2 (pO_2) constant in the tissue during increased neuronal activity. The authors showed with a theoretical model that a $CMRO_2$ increase of 20% with a constant CBF would lead to a 30% drop of tissue pO_2 . However, a CBF increase approximately 2.5 times higher than $CMRO_2$ would be able to keep tissue pO_2 of 25 mmHg constant. The brain tissue has a low oxygen concentration, but an excess of oxygen delivery as compared to utilization at rest, given that the effective O_2 partial pressure that limits $CMRO_2$ through cytochrome oxidase is below 1 mmHg and the oxygen surplus diffuses back to the capillary (24). However, during activation it may be used for oxidation without a necessary fast early increase in CBF (11).

Fig. 1.1. shows typical theoretical waveforms of evoked CBV, CBF, $CMRO_2$ and resulting deoxyhemoglobin (dHb) in a volume of cerebral tissue after a stimulus with duration in the seconds range. An early increase in neuronal activity prior to the signaling that triggers the vascular response leads to the small hump observed in the deoxyhemoglobin curve. A fast CBF response (larger than $CMRO_2$ increase) carrying fresh blood decreases the relative concentration of deoxyhemoglobin in the blood, as shown by the depression in the curve. After the end of the stimulus, a slower return of total CBV as compared to CBF originates the overshoot observed in the curve. The dynamics of relative

deoxyhemoglobin concentration is a key factor for understanding the dynamics and the mechanism behind the origin of the Blood Oxygen Level Dependent (BOLD) signal, to be discussed on Section 3.3. The relative concentration of deoxyhemoglobin is directly linked to the Oxygen Extraction Fraction (OEF), given by equation 1.1, where Hct is the hematocrit and Y_a the arterial blood oxygen saturation.

$$OEF = \frac{CMRO_2}{CBF \cdot Hct \cdot Y_a} \quad (1.1)$$

Several different factors can alter the neurovascular coupling and contribute for the variability of $\Delta CBF/\Delta CMRO_2$ ratio. It has been shown that the level of stimulation (22), the degree of attention (25), adaptation to a sustained stimulus (26) and even the effects of drugs (27,28) are capable of altering the vascular coupling. In a very interesting study, Griffeth et al. (2011) used the calibrated BOLD methodology (29) to reveal changes in the neurovascular coupling before and after the intake of caffeine. The main findings were a decrease in baseline CBF due to caffeine while baseline $CMRO_2$ was increased, and absolute $CMRO_2$ in response to visual stimulation was 60% increased post-caffeine. The authors argue that the balance of CBF and $CMRO_2$ changes may vary depending on specific aspects of neuronal activity. While an increase in $\Delta CMRO_2$ due to stimulation is consistent with an increase in excitability promoted by caffeine, the decrease in CBF is explained by the inhibition of vasodilatory effects of adenosine by caffeine. Thus, the use of caffeine is clearly capable of alter the coupling between CBF and $CMRO_2$. The normal healthy aging is also another important variable that affects the neurovascular coupling (30). It has been shown that the magnitude of $CMRO_2$ and CBF declines in large parts of the brain, but primary motor and sensory areas are relatively spared (30), and OEF increases in frontal and parietal cortex. Such findings might indicate a possible mechanism of transformation from the healthy to unhealthy aging, since most regions affected are the most vulnerable to neurodegenerative diseases (30).

Most functional studies focused in the visual cortex, which is accepted to embody the general properties of cortical brain function (31). The visual system is arguably the most important pathway for input of information to the human brain, which yields higher levels of intrinsic neuronal activity and energy consumption, as proven by higher blood flow in the occipital lobe as compared to other regions of the brain (32).

In order to fuel the many mechanisms and processes described in this chapter, neurons and astrocytes rely in a complex group of chemical reactions that are part of the energy metabolism and are responsible for providing the necessary energy from substrates such as glucose, as discussed in chapter 2. Since oxidative metabolism of glucose is the main source of energy to cerebral cells at rest, oxygen plays an essential role in the bioenergetics of the human brain.

CHAPTER 2 - ENERGY METABOLISM AND HYPOXIA

2.1 Bioenergetics of human brain

It is important to consider the nature of the energy expenditure in the cerebral tissue. Neurons form elaborate networks through which action potentials (altered membrane potentials) propagate. The major role of the human brain is to transfer and process information through the propagation of an action potential and through the release of chemical neurotransmitters. Both processes are heavily dependent on ion transportation across the nervous cell membrane. The three main energy consuming processes in neuronal cells are: maintenance of the electrochemical membrane potentials, restoration of the membrane potential after neuronal excitation and neurotransmitter release and cycling.

Brain cells actively maintain electrochemical membrane potentials through the regulation of specific ion channels in the membranes that exchange free ions (e.g. Na^+ , K^+ , Cl^-) between intra and extracellular compartments. A stable membrane potential is maintained when the conductance for each ion matches the active ion transport against the concentration gradient (33). Pumping ions against an electrochemical gradient is an energy demanding process. The $\text{Na}^+\text{K}^+\text{ATPase}$ enzyme hydrolyses ATP in order to induce conformational changes in its structure that translocate K^+ in and Na^+ out of the intracellular space. Brain metabolism associated with transport of Na^+ and K^+ represents approximately 40% of normal energy consumption, shown through the complete inactivation of $\text{Na}^+\text{K}^+\text{ATPase}$ (34–36).

Neuronal excitation occurs when membrane channels with voltage-dependent conductance open to allow passive flow of Na^+ ions into the cytoplasm from the extracellular space and K^+ in the opposite direction, leading to a steady depolarization that can trigger spontaneous neuronal discharge when a threshold is reached. Thus, neuronal excitation leads to energy consumption due to the necessity of reestablishing the electrochemical gradient through active transport. Not surprisingly, the energy metabolism of brain tissue in conditions of low activity (e.g. coma, persistent vegetative state, anesthesia) can exhibit nearly half of the normal level (37,38) of approximately 40% of total energy consumption (1).

While the signal propagation occurs through the nervous cell membrane similarly to an electrical impulse, the equivalent current propagation cannot travel through the synaptic cleft (i.e. between neurons), which acts as a physical barrier. Neurotransmitters are chemical messengers responsible to transfer the signal propagation from one neuron to another. Glutamate is the main excitatory neurotransmitter found in the human brain and approximately 80% of neuronal glucose consumption at rest accounts for glutamatergic synaptic activity (39). Another fraction of approximately 13% of glucose consumption is utilized for sustaining predominant inhibitory neurotransmitter γ -aminobutyric acid (GABA) synaptic activity (40). Thus, neurotransmission is primarily represented by excitatory glutamatergic synaptic activity and a smaller fraction of inhibitory gabaergic neurons. In addition, 5 to 10% of cellular energy production is dedicated to protein and other molecule synthesis, as part of the “housekeeping” functions.

The glutamate-glutamine cycle (Glu-Gln) is a recycling process that replenishes glutamate used in the excitatory neurotransmission process. A quick removal of glutamate from the synaptic cleft is necessary to enable the next action potential and also prevent glutamate neurotoxicity (41). The Glu-Gln cycle takes place partially in the in neurons, where glutaminase is located, and in the astrocytes, where glutamine synthetase occurs. After an action potential, the released glutamate is removed from the synaptic cleft by the astrocytes surrounding the synaptic area. The glutamate is then converted to glutamine and moved from the astrocytes to neurons by glutamine transporters. Finally, glutamine is converted by glutaminase to glutamate in the neuron (42). The Glu-Gln cycle consumes approximately 10% of the total ATP consumption (2), thus it has a relative small energetic demand as compared to membrane potential maintenance and action potential propagation.

During increased neuronal activity induced by sensory stimulation in awake humans, the glucose consumption increases between 12 to 20% (17,43). The execution of cognitive tasks tends to demand additional 5 to 15% of baseline CMR_{Glc} (44). Thus, glucose requirement increment due to stimulated activation is relatively small as compared to the demand under rest condition. Therefore, it seems reasonable that increased neuronal activity does not require additional physiological mechanisms, but an up-regulation of the same biochemical processes that are present in rest condition (39).

The ATP molecule is considered the energy currency for brain cells and is the link between energy utilizing and energy producing processes. The brain energy metabolism is adapted to maintain ATP concentration constant, since the processes that are responsible for restoring ATP levels are directly or indirectly sensitive to ATP utilization. Heart and brain data suggests that rapid variations of energy demand by as much as 10-fold can be sustained with minimal variation of ATP concentration (45–48), which can be achieved due to the fact that biochemical pathways responsible for ATP synthesis are regulated by factors that are linked to its rate of utilization. Short and long term regulatory mechanisms are used to maintain stable ATP levels throughout different energetic demand levels.

A short-term mechanism for ATP production (within the first minutes range) is the hydrolysis of phosphocreatine (PCr), unique to cerebral and muscle tissue. The enzyme creatine kinase (CK) plays an essential role on early buffering of ATP concentration, catalyzing the interconversion of ADP (adenosine diphosphate) and PCr to ATP and creatine. CK is active in the cytosol and maintains the ADP/ATP interconversion near equilibrium (i.e. $[ADP][PCr]=[ATP][creatine]$ at constant pH) (49,50) shown by equation 2.1. Therefore, as ADP concentration (1-2 orders of magnitude small than ATP) rises, PCr decreases to maintain ATP approximately constant.



One advantage of this mechanism for high energy phosphate bonds transport is that PCr diffuses over the cytosol an order of magnitude faster than ATP (51), hence it provides a fast ATP source for cellular sites with increased energy demand. However, homeostasis cannot be maintained during prolonged high energetic demand due to the slow replenish of PCr in the muscle tissue (51). Despite the presence of CK in the brain, much smaller PCr concentrations are found in the brain tissue. Functional experiments have shown variable results with either reduction (52,53) or stable (54,55) PCr or PCr/Pi levels. ^{31}P Magnetic Resonance Spectroscopy (MRS) studies combined with magnetization transfer technique allowed the quantification of in vivo turnover rates of PCr-ATP interconversion, and it has been suggested that during the increased neuronal activity, the $ATP \rightarrow PCr$ synthesis ratio increases by 34% without significant changes of steady-state concentration changes (56). Therefore, PCr as an energy source during increased energetic demand in the cerebral tissue might not be as relevant as it is in the muscle tissue.

A more sustained increase in ATP utilization rate is balanced by increase in rates of glycolysis, which is consisted of a series of enzyme-catalyzed reaction necessary for energy-release breakdown of glucose to pyruvate, resumed in equation 2.2. In the absence of oxygen, anaerobic glycolysis occurs until the conversion of pyruvate to lactate and lactate removal from the cell is no longer possible, but under aerobic conditions the production of pyruvate is linked to their oxidation in the mitochondria. Glycolysis reactions can respond in the order of a few milliseconds (57,58), which is critical for maintaining bioenergetics homeostasis in response to rapid cell energy utilization.



Glucose is transported into brain cells by membrane proteins belonging to the GLUT family (57). Since the rate of transport is proportional to the difference between serum and cytoplasmic concentrations (59). However, under normal circumstances, glucose transport is not a rate-limiting factor for glycolysis.

As a long term mechanism with the highest ATP production efficiency available to brain cells, the oxidative phosphorylation is a complex chain of reactions that requires pyruvate and oxygen as substrate. The enzyme lactate dehydrogenase buffers changes in the concentration of pyruvate, which is a key intermediate linking glycolysis to oxidative metabolism. Pyruvate can be substrate for either oxidative metabolism in the mitochondria or reduced in the cytosol with conversion to lactate. At steady state the brain cells almost completely oxidizes glucose via aerobic glycolysis (60–62), thus almost all pyruvate produced by glycolysis is subsequently oxidized in the mitochondria. Mitochondrial oxidative metabolism (i.e. oxidative phosphorylation) that follows aerobic glycolysis is tightly regulated at two basic levels. First, the amount of substrate provision to key enzymes of the tricarboxylic acid (TCA) cycle responsible for oxidizing the three carbon atoms in the pyruvate molecule into CO₂. A second level of control is in the transfer of the electrons resulting from these oxidation reactions to the oxygen molecule, their final acceptor. The electrons produced with the oxidation of pyruvate release substantial amount of energy that is used to synthesize ATP when transferred to an electron acceptor. This process occurs in the second stage of the oxidative phosphorylation, known as electron transport chain. The most important terminal enzyme from the chain is cytochrome c oxidase, which serves as the ultimate electron receptor. The transfer of electrons to oxygen

by the enzyme complexes is linked to the pumping of protons across the mitochondrial membrane, which created an electrochemical potential (i.e. proton motive force) that is used to synthesize ATP by the enzyme ATP synthase that is located in the inner mitochondrial membrane. Despite the complexity of oxidative metabolism, its efficiency is much larger as compared to anaerobic glycolysis: the net amount of ATP molecules generated through complete oxidation of one molecule of glucose is approximately 30 versus 2 molecules generated by anaerobic glycolysis (63). A schematic representation of the location where the previously described energetic pathways take place in a simplified cellular structure is shown in (Fig. 2.1.).

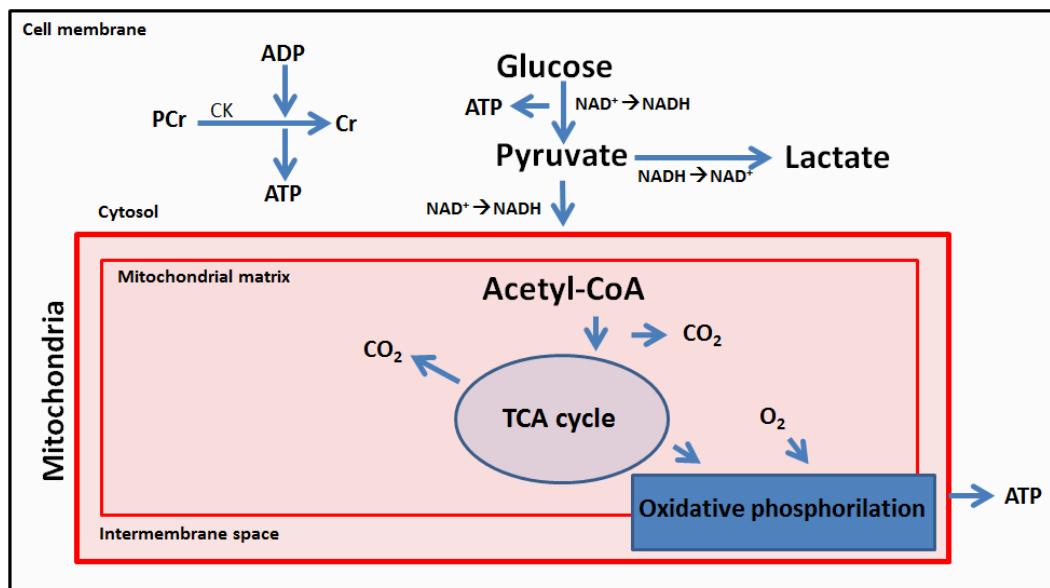


Fig. 2.1. Schematic representation of a cell and main energetic pathways distribution.

Up to this point, brain bioenergetics was demonstrated with respect to a single generic cell, but brain tissue has a diversity of cell populations (e.g. neurons, astrocytes, oligodendrocytes and microglia cells). From the energy consumption perspective, the most relevant cells are the neurons and astrocytes. While the TCA cycle activity is higher in neuronal cells, suggesting higher ATP synthesis, it still remains unclear whether glucose is preferentially taken up by neurons or by glial cells (64,65). In addition, glucose can be stored as glycogen in astrocytes to be used as an energy buffer and eventually converted back to glucose through glycogen phosphorylation (66).

During the first seconds of increased neuronal activity (i.e. up to 10 s), intracellular Na⁺ and Ca²⁺ starts to build up and K⁺ is released from neurons whereas mitochondrial

intermediates are rapidly oxidized together with oxygen for extra ATP generation (67). Increases in intracellular and mitochondrial Ca^{2+} are signaling mechanisms responsible for stimulating the TCA cycle through the enhance of enzymatic activity, which also results in increased release of free radicals and reactive oxygen species. Reduced Nicotinamide Adenine Dinucleotide (NADH) coenzyme levels decrease when oxidative pathways for ATP synthesis rates are stimulated (68) and influx of glucose and lactate to neurons result in a transient decrease in lactate and glucose concentrations in the extracellular space (69). The neuronal increased activity also creates a transient drop in oxygen concentration due to increased oxidative phosphorylation (70), which stimulates a series of reactions to locally increase CBF. During the recovery phase after increased neuronal activity, the metabolic needs can persist as well as delayed enhancement of CBF. NADH remains elevated temporarily (70) due to persistent dehydrogenase activity (71) while short-term intermediate molecules within the mitochondria are depleted.

2.2 Reduced oxygen availability and hypoxia

As the final receptor for high energy electrons, oxygen has an essential role in oxidative metabolism. In the absence of oxygen, the electron carriers NADH and FADH_2 are not recycled in the electron transport chain. Since both molecules are also used in the TCA cycle, the lack of the non-reduced forms will eventually stop the TCA cycle, making the oxidative metabolism not sustainable and hence reducing the efficiency of bioenergetic metabolism. In addition, the lack of acceptors for the high energy electrons generate high levels of free radicals that attack proteins and membranes causing severe cellular damage (72).

The efficiency of bioenergetics of human brain is highly dependent on oxygen, thus a tight regulation and distribution of blood through the vascular network aims at protecting cerebral tissue from the lack of oxygen. Hypoxia is characterized as a condition in which the body or a specific tissue does not receive the normal oxygen supply for maintenance of metabolism. According to the cause of oxygen availability reduction, hypoxia can be classified as (73): hypemic hypoxia, due to the reduction of the oxygen carrying capacity of the blood (e.g. anemia, carbon monoxide poisoning); stagnant hypoxia, caused by low oxygen perfusion or diffusion (e.g. weak cardiac output, venous pooling during high G

force); histotoxic hypoxia, due to lack of capacity to metabolize oxygen (e.g. alcohol and cyanide poisoning); hypoxic hypoxia, caused by reduced oxygen availability in the medium (e.g. low oxygen supply in the air, decreased lung ventilation). In this work, the term “hypoxia” will always refer more specifically to hypoxic hypoxia.

A variety of molecular pathway responses have been observed in the presence of hypoxia, although hypoxia sensing in higher organisms remains poorly understood (73). The traditional mechanism for hypoxia sensing involves a heme protein that contains iron atoms in a heme site (74). The reversible binding of O₂ in the heme site causes an allosteric shift in the protein. Many potential hypoxia sensitive molecules have been studied, but no good candidate has been found (74). Another hypothesis involves specific ionic channels that are inhibited during hypoxia. However, certain channels that inhibited or stimulated during hypoxia can present different response in other types of cells and yet, it is not known how O₂ interact with channels (75,76).

As mentioned before, the lack of oxygen stops ATPase since the proton motive force is not sustained, hence oxidative metabolism is blocked. Inadequate levels of ATP affect ionic homeostasis of the cell as ionic pumps do not perform active transport without ATP. Finally, the excessive Na⁺ ion in the cytosol leads to osmosis and hence an inflow of water from the medium towards the interior of the cell, which potentially causes cell death. In the event reperfusion (i.e. reestablishment of oxygen supply) before cell death, mitochondrias perform intensive oxidative phosphorylation and generate a large quantity of free radicals that attack proteins and membranes causing severe cellular damage and potentially cell death (72).

At a larger scale in the body, peripheral vessels dilate in response to low oxygen, whereas vessels of the pulmonary vasculature constrict to shunt blood away from the poorly ventilated region, matching ventilation and perfusion (77). Airway neuroepithelial bodies are the structures responsible for sensing changes in inspired oxygen, whereas arterial blood oxygen levels are monitored by the carotid bodies located at the bifurcations of the common carotid arteries. Both respond to decreased O₂ supply by initiating activity in efferent chemosensory fibers to increase heart and respiratory rates during exposure to low pO₂ (75,78).

Adaptation to hypoxia at the cellular level happens by increasing the ratio of energy producing pathways, mainly through increased anaerobic glycolysis activity, but also decreasing energy consuming process (79). At the organism level, increased ventilation and cardiac output are accompanied over longer period of time (weeks/months) with improved vascularization and O₂ carrying capacity of the blood through the regulation of gene expression, for more information refer to Michiels et al. (2004).

Despite the deadly effects of complete oxygen deprivation within minutes, partial reduction of oxygen availability is frequent in chronic disorders such as obstructive sleep apnea, which affects 2 to 4% of adult population, and has been suggested to be a risk factor for morbidities such as hypertension and stroke (Nieto2000, Epstein2009, Parra2000). Between pulmonary hypertension and sleep apnea, there are millions of people living with a mild level of hypoxia, and yet little is known about its effects in the human brain physiology. Functional MRI and MRS experiments offer a unique non-invasive window to in vivo physiology of the vascular system and the neurochemical profile of approximately 20 human brain metabolites. The combination of functional experiments simultaneously to mild hypoxia exposure can potentially provide new insights into the neurovascular coupling during reduced oxygen availability.

CHAPTER 3 - FUNCTIONAL MRI AND MRS TECHNIQUES FOR BRAIN STUDY

3.1 Functional experiments

Several functional experiments in neuroscience aim at correlating brain function and structure by evaluating dynamics of time varying physiological mechanisms/responses. These experiments normally involve the presentation of a stimulus (e.g. visual, auditory), execution of a task, (e.g. motor, attention) or even a simple record of a signal fluctuation over time (as in resting-state fMRI, which reflects physiological fluctuation). The repetition of multiple acquisitions over time allows the monitoring of the mechanism/variable of interest. Several methods based on different physical properties and contrasts offer different temporal and spatial resolutions to probe mechanisms, as shown in Fig. 3.1.

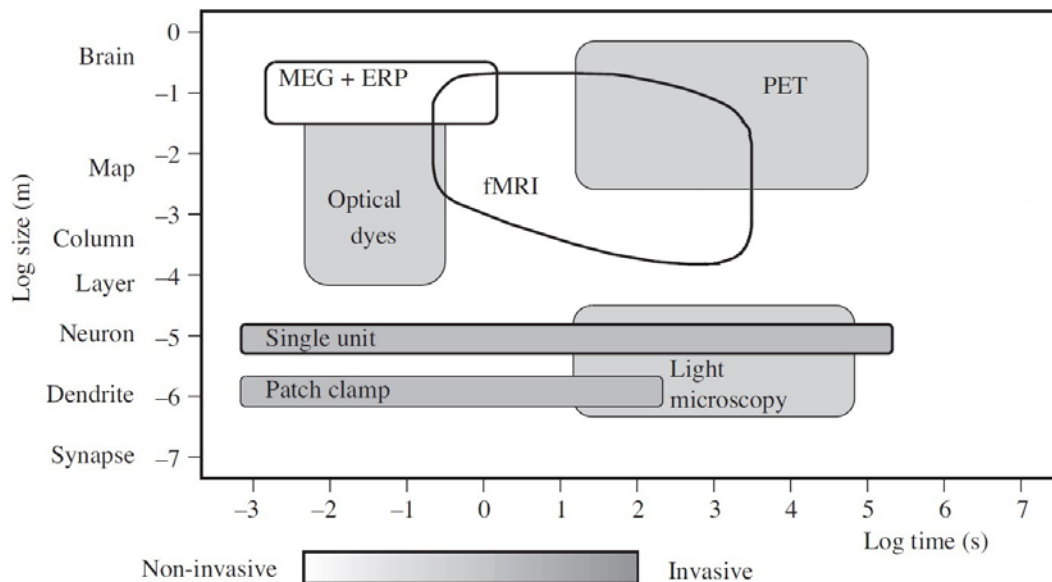


Fig. 3.1. Graphical representation of an estimate of temporal/spatial resolution and degree of invasiveness of different techniques that allow the functional study of the central nervous system or its components. MEG: magnetoencephalography; ERP: event-related potential from EEG measurements; PET: positron emission tomography; 2-deoxyglucose: a specific tracer for PET. Adapted from Jeezard et al (2001).

Electromagnetic-physiological methods based on directing mapping of transient current dipoles generated by depolarization (e.g. EEG, MEG) have potential to record the

underlying neuronal events in almost real time (millisecond scale), but provide relatively poor spatial resolution. In contrast, optical imaging methods involving dyes can provide excellent spatial resolution (in the level of layers and neurons) with temporal resolution in the range of milliseconds, but are restricted to the study of the cortical surface, are invasive and not suitable for human studies. Among the non-invasive techniques, functional MRI occupies a unique niche and has the potential to link high spatial and temporal resolution studies to an understanding of systems organizations across the brain. Modern multislice MRI techniques combined with high magnetic fields for increased signal allow spatial resolution up to a tenths of millimeters and temporal resolution of a seconds during a full brain coverage acquisition (80). In addition, deep structures can also be studied in a non-invasive manner.

The sequential acquisition of multiple image volumes is the basis of fMRI experiments, in which the parameter of interest (e.g. signal, vascular parameter, contrast) is monitored over time. The presentation of a stimulus or execution of a task is commonly performed during acquisitions in order to evaluate how the related changes in the parameter of interest induced by the stimulus/task. The modeling of the MRI signal can provide an indirect measurement of the dynamics of a vascular parameter, such as CBF and the Arterial Spin Labeling technique. In addition, the acquisition of multimodal-fMRI data, which consists on functional images weighted on different parameters (e.g. CBF and CBV), together with mathematical models allow the estimate of variables such as changes in $CMRO_2$. A description of the theoretical framework utilized for estimating $CMRO_2$ changes due to a visual stimulus from fMRI data is provided in Section 3.6.

Similarly to fMRI, functional MRS consists of acquiring multiple MR spectra instead of images. However, since the brain metabolites concentration is approximately 4 orders of magnitude smaller than water concentration in the cerebral tissue, multiple averages are necessary to improve SNR. Hence, the temporal resolution of fMRS is much reduced (in the order of minutes) as compared to fMRI. Details in the sequences for MRS data acquisition are provided in Section 3.7.

3.2 A brief introduction to MRI physics

Nuclear Magnetic Resonance (NMR) is one of the most flexible and non-invasive tools to investigate the human physiology. NMR can indeed provide a broad variety of morphological, physiological and metabolic information. The intrinsic dependence of the NMR signal on multiple mechanisms provides the opportunity of generating multiple contrasts (e.g. relaxation, susceptibility, diffusion, chemical shift). In recognition to its great potential and technological advances, Nobel prizes in medicine, physics and chemistry were rewarded to NMR scientists and researchers over the past decades.

The central concept of NMR phenomenon is the nuclear spin (I), present only in nuclei that contain an odd number of protons and/or neutrons. Nuclei with zero nuclear spin are not visible to NMR techniques. In a semi-classic model, the nuclear spin is considered an angular momentum (\vec{J}) which pictorially represents the nucleus rotation around its own axis. From quantum mechanics principles, the magnetic moment ($\vec{\mu}$) of one particle is related to the angular momentum through the gyromagnetic ratio (γ), which is isotope-specific and given by $\vec{\mu} = \gamma \vec{J}$. The magnetic moment represents the rotation of a nucleus that contains electrical charges distributed on its surface. When exposed to an external static magnetic field (\vec{B}_0), the magnetic moment experiences a torque and exhibits a precession movement (as a gyroscope) under the Larmor frequency (ω_0), defined as $\omega_0 = \gamma B_0$, normally in the radiofrequency (RF) range. If a time-varying magnetic field (\vec{B}_1) containing the Larmor frequency is applied orthogonally to the direction of the static field, the sample will absorb energy in this resonance frequency ω_0 . Normally, B_1 field is considered a perturbation as compared to B_0 .

The macroscopic observable variable is the net magnetization (\vec{M}) generated by the sum of the magnetic moments of the sample per volume unit. Due to the Zeeman Effect, there is a difference in energy and population size between the parallel and anti-parallel spins, which is proportional to the static magnetic field. For a sample of hydrogen nuclei at thermal equilibrium, two population states following the Boltzmann distribution (spin “up” and spin “down”) are present, and the difference between the two at 293K (20°C) and 3T is in the order of 1 ppm. The difference between population states generates the net

magnetization \vec{M} , which is directly proportional to B_0 and the square of γ , but inversely to the temperature. The NMR sensitivity is proportional to this weak net magnetization in the magnetic field strengths used in the clinical practice. The intrinsic relatively low sensitivity is a limitation from NMR techniques that can be partially overcome by the great abundance of ^1H from water molecules in soft tissues of living organisms. However, other elements of interest (e.g. ^{13}C , ^{31}P , ^7Li , ^{23}Na) have much smaller abundance and lower gyromagnetic ratios, and are greatly benefited by the use of stronger magnetic fields ($>3\text{T}$). The study of material/chemical samples can potentially benefit from the use of lower temperatures to increase \vec{M} , however that is not an option for the study of living organism.

In order to detect a NMR signal, \vec{M} should rotate in the transverse plane relative to B_0 direction. This can be accomplished by using an excitation pulse of the mentioned \vec{B}_1 . The behavior of \vec{M} is described by a set of empirical differential equations denominated Bloch equations (81). While \vec{M} returns to equilibrium through relaxation mechanisms (to be discussed below), the bulk magnetization rotates about \vec{B}_0 and its transverse component induces an electromagnetic force in the probe placed in the surroundings of the sample.

The most common sources of contrast in MR arise from tissue specific properties: proton density (PD), longitudinal and transverse relaxation (82). A PD weighted image exhibits a contrast based on the concentration of water molecule H nuclei. Such contrast can be obtained when relaxation effects are minimized by the use of adequate acquisition parameters: echo time (TE) $\ll T_2$ and repetition time (TR) $\gg T_1$. The acquisition parameter TE is defined as the time between an excitation pulse and the signal readout, whereas the parameter TR is defined as the time between two consecutive excitation pulses that characterize one repetition in the acquisition. The constants T_1 and T_2 are tissue-specific and are defined as longitudinal relaxation time and transverse relaxation time, respectively. After an excitation pulse, the transverse magnetization rotates in the transverse plane at the Larmor frequency representing an excited state of the system. The equilibrium state represented by the macroscopic magnetization oriented in B_0 direction is reached by the relaxation mechanisms. The transverse magnetization is a composition of individual spins, exposed to static and slowly fluctuating local magnetic field variations. Thus, inhomogeneities in the external magnetic field and some internal magnetic

interactions between spins lead to slightly different resonance frequencies around the Larmor frequency and loss phase coherence. Hence, the loss of phase coherence results in a decrease of the transverse magnetization amplitude over time. The characteristic transverse relaxation time T2 represents the amount of time necessary for the transverse magnetization decay to 37% of the initial transverse magnetization. More specifically, when the effect of the inhomogeneities in the magnetic field are not cancelled by a radiofrequency refocusing pulse, as in a gradient echo sequence, the effective relaxation time is defined as T2*. As an independent parameter from another relaxation mechanism, the characteristic longitudinal relaxation time T1 represents the amount of time necessary for the longitudinal magnetization recover to 63% of its equilibrium value.

The resonance frequency of a nuclear spin depends on the locally experienced magnetic field, which is the composition between the externally applied magnetic field and the magnetic field generated by the surrounding electrical particles, mainly circulating electrons. The magnetic field created by electrons surrounding the nucleus opposes the main magnetic field, hence causing a small decrease in the effective magnetic field experienced by the nucleus. The chemical shift contrast is based on the slightly different resonance frequencies caused by the “shielding” of the surrounding electrons. Thus, different molecular structures with different electron distribution create different resonance frequencies that can be measured and used to identify/quantify compounds. The chemical shift mechanism is the basis of MRS technique, to be discussed in more details in Section 3.7.

Another widely used MR contrast is diffusion, which is based on the translational motion of molecules (Brownian motion) that results in molecular diffusion (83). Dephasing and rephasing gradients are used to weight the signal on diffusion: as water protons diffuse over the medium, the phase created by the first dephasing gradient is not entirely recovered by the following rephrasing gradient, which results in signal loss. After multiple acquisitions with different gradient orientations, it is possible to estimate the intensity and direction of prevalent diffusion.

More recently, susceptibility weighted imaging (SWI) has provided an innovative source of enhancing contrast to changes in magnetic susceptibility that are common in iron deposits, hemorrhage and calcifications (84). The basic concept of SWI is to use the phase

information from the tissue to weight the final magnitude image after the removal of phase artifacts. In a simplified manner, regions with large variations of susceptibility generate inhomogeneities in the magnetic field that are reflected in the phase measurements.

As discussed in Section 3.1, the sequential acquisition of multiple image volumes is the basis of fMRI experiments. In order to obtain reasonable temporal resolution, MR sequences should be fast enough to acquire several slices or a complete volume within 1 to 2 seconds. The most common readout sequence for this application is the Echo Planar Imaging (EPI), which consists of the sampling of an entire two dimensional k-space matrix following a single RF excitation pulse combined with a magnetic field gradient for slice selection (85). Repeated reversals of the measurement (readout) gradient repeatedly refocus the transverse magnetization to yield a train of gradient echoes (GE). In addition, a large initial phase encode gradient serve to place the first echo at the periphery of the k-space, and subsequent blips of the phase encode gradient serve to increment the acquired echoes through k-space (Fig. 3.2.). After the acquisition of a slice k-space, a spoiler gradient pulse eliminates any remaining transverse magnetization and another RF pulse excites the following slice within the same TR. Considering that each k-space readout usually takes approximately 50 ms in a clinical 3T MR scanner with standard hardware (40 mT/m gradients, slew time of 200 mT/m/ms), up to 20 slices can be easily acquired within a TR of 2 seconds.

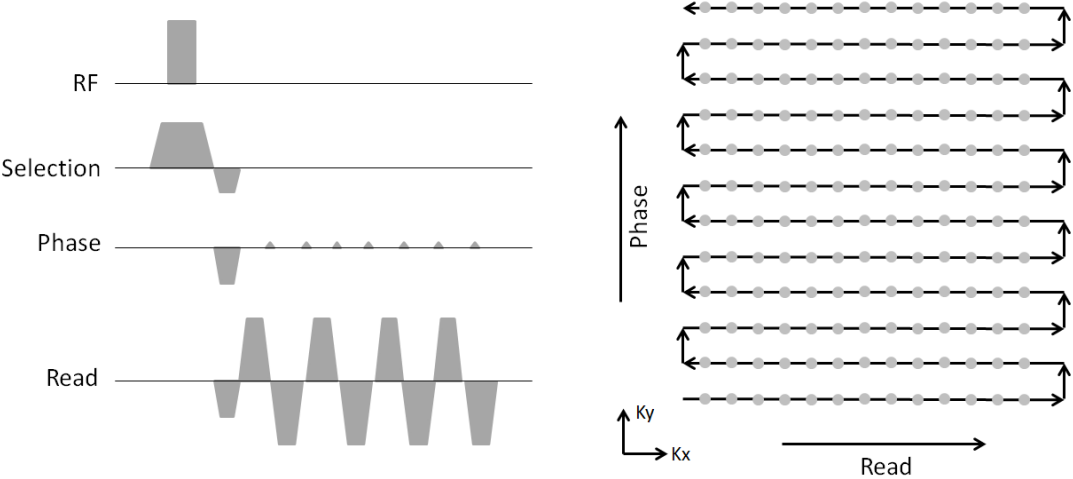


Fig. 3.2. Basic EPI pulse sequence diagram (a) and k-space trajectory generated (b).

The echo formation during EPI readout is generated by a gradient echo scheme, hence the signal acquired is T2*-weighted. One limitation of EPI readout is geometrical

distortions created by off-resonance water spins generated due to inhomogeneities in the main magnetic field as a result of poor shimming and/or susceptibility effects. Although good shimming can reduce the overall level of inhomogeneities of the magnetic field, little can be done to reduce the effects of strong variation in susceptibility. Characterizing the magnetic field inhomogeneities with a B_0 map can be useful for correcting geometric distortions during post-processing (86). Another limitation of EPI readout is the chemical shift artifact generated by off-resonance fat spins in the phase encoding direction due to reduced bandwidth as compared to the read direction. This issue leads to substantial displacements of fat signal, and is partially overcome by selective saturation of fat signal or selective excitation of water signals only.

3.3 Functional MRI: Blood Oxygen Level Dependent contrast

The physiological basis of BOLD fMRI is the rapid and robust increase in CBF subsequent to a neuronal stimulus, typically 2-4 times larger than the associated fractional change in $CMRO_2$ (87). From the OEF perspective, the fraction of delivered oxygen that is extracted from the blood and metabolized decreases during increased neuronal activity, leading to a relative increase in the oxy/deoxyhemoglobin ratio and a fractional decrease in the relative concentration of deoxyhemoglobin. Due to the strong paramagnetic characteristic of deoxyhemoglobin as compared to oxyhemoglobin, its presence alters the local magnetic susceptibility, creating field distortions within and around blood vessels (88,89). The locally distorted magnetic field leads to slightly different resonance frequencies; hence a reduction in the MR signal through the loss of phase coherence between spins. Thus, the fractional reduction of deoxyhemoglobin during increased neuronal activity (as discussed above) causes a reduction in the field distortion and increase of up to 5% in the MR signal. This small BOLD signal change is the mapping signal used in most fMRI applications.

The BOLD response is the combination of both vascular and metabolic events that together generate the observed MR signal time course. A schematic representation is shown in Fig. 3.3. Three characteristics in addition to the main positive response are often observed: the initial dip, the stimulus overshoot and the post stimulus undershoot. First, immediately after increased neuronal activity commences, there is a brief period of 0.5-1s during which the MR signal decreases slightly below baseline, known as the initial dip,

reported in human (90) and animal (91) studies. This effect has been attributed to an immediate stimulus-driven increase in oxygen consumption accompanied by a slight latency in the vascular response. Subsequently, a robust positive response peaks within 5-8 seconds after the start of stimulation. The positive waveform often shows an overshoot on its early stage, and a post-stimulus undershoot after the stimulus cessation. Although it remains not entirely clear the origin of both aspects of the BOLD response, it has been suggested that the slow dynamics of CBV as compared to the fast rise of CBF creates the stimulus overshoot (92), whereas both slow CBV return to baseline and delayed recovery of CMRO₂ are possible sources of the post stimulus undershoot (92,93).

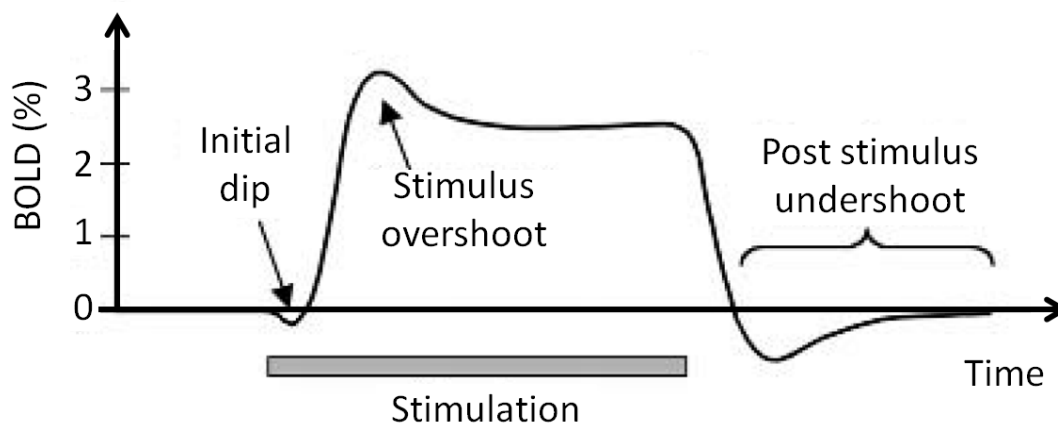


Fig. 3.3. Representation of a typical BOLD response to stimulation and its temporal characteristics. The initial dip, the stimulus overshoot and the post stimulus undershoot are often seen features of the BOLD response. Adapted from Jezzard et al. (2001).

The amplitude of BOLD signal generated by a robust stimulus such as visual or motor is approximately 2-4% at 3T (94). The optimal TE for detection of BOLD signal depends on T2* values during activation and rest. By subtracting T2* decay curves from both states, it is possible to estimate the optimal TE for BOLD detection. In general, the optimal TE is approximately the apparent T2* of the tissue. Since T2* tends to become smaller with field increase, the optimal TE for a higher field is shorter as compared to lower field (95).

The analysis of BOLD fMRI data has as main objective the identification of voxels that show signal changes accordingly to the functional paradigm throughout the acquired images. This process is inherently limited by the fact that signal changes are small, potentially creating false negatives (type II error). In addition, the large number of voxels simultaneously interrogated can generate false positives (type I error). In order to prepare

the data for statistical analysis, a series of steps are performed to pre-process the data. The first step is the slice-timing, which is critical for longer TRs and a large number slices is acquired. It consists of interpolating the data to account for the fact that each slice is acquired in a different moment within the TR (not all at a single time point). The second step is the image realignment using rotation and translation (no distortions), so each volume acquired is aligned to every other volume and small motion amplitude (<3 mm) is corrected. Since functional images are acquired in reduced spatial resolution for time optimization, functional images are usually coregistered (affine, 12 degrees of freedom) to high resolution anatomical images and later overlaid for better anatomical positioning. Spatial blurring is commonly applied to increase signal-to-noise ratio (SNR) of images without affecting the activation signal. When group analyses are desired, images undergo a second affine transformation so a standard space, such as Talairach (96) space or Montreal Neurological Institute (MNI) space (97). Optionally, the removal of low (e.g. linear and slow drifts) and high frequency (e.g. physiological noise) are also performed as a last step. After the pre-processing, a statistical analysis is carried out to determine which voxels are activated during stimulation. The main output of the analysis is statistical map which indicates through a quantitative variable the voxels where the brain has become active in response to the stimulus. The analysis of each voxel's time course independently is the most common procedure, usually with a model-based method (98). A stimulus function is designed as a boxcar function where rest time points are represented as 0 and stimulation periods are 1. In order to obtain the best possible fit, the stimulus function is convolved with the hemodynamic response function (99) to create a detailed model (similar to the waveform from Fig. 3.3). The General Linear Model (GLM) is the standard method to fit the functional data using a model derived from stimulation paradigm (98). For each voxel time series, a linear modeling according to equation 3.1 is performed, where $y(t)$ is the data, $x(t)$ is the model function, β is the parameter to be estimated and $e(t)$ the error in the fitting.

$$y(t) = \beta * x(t) + e(t) \quad (3.1)$$

The ratio $\beta/SE(e(t))$ is often denominated as T and used as quantitative variable for a hypothesis test. SE function represents the standard error. The statistical map from the hypothesis test carries the information of how the time series is similar to the input model.

Thus, T is a good measure of whether β is significantly different from zero considering the error in the regression, i.e. whether there is a reliable activation. A threshold at a given level of significance is used to threshold the T map and define regions that are “activated” (i.e. responded to the stimulus). However, due to the large number of voxels in the image, correction for multiple comparisons (e. g. Bonferroni, false-discovery rate (100)) needs to be performed otherwise certain voxels would be classified as active just by chance.

The dependence of BOLD signal on the evoked vascular response (CBF, CBV, CMRO₂ and baseline physiological state) makes difficult the interpretation of its amplitude change without further information. For this reason, the BOLD effect has been mainly used as a mapping tool based on the detection of signal changes, rather than as a probe of the underlying physiology (9). However, the combination of BOLD signal with other MRI methods for characterizing different components of the vascular response makes possible a much more detailed modeling of the physiological process.

3.4 fMRI: Vascular Space Occupancy contrast

The Vascular Space Occupancy (VASO) fMRI is a non-invasive technique that uses activation-related changes in CBV as a contrast mechanism to conduct functional MRI (101). It allows the dynamical measurement of CBV changes in humans and complements the information provided by other techniques such as oxygenation-based BOLD and CBF-based Arterial Spin Labeling (ASL). When combined, these techniques can provide insights on the neurovascular coupling and help improve our understanding on the cerebral oxygen metabolism (102).

The basis of VASO-fMRI is the selective nulling of blood signal, achieved by a RF pulse that inverts the longitudinal magnetization of water from a parallel state to anti-parallel one, relative to the main static magnetic field. The longitudinal relaxation will cause magnetization to decrease over time and return to the equilibrium value. However, since T_1 from blood and tissue are different, it is possible to select an adequate inversion time (TI) in which the blood signal is zero, but the tissue signal is not nulled and remains detectable, similarly to an Inversion Recovery (IR) sequence. An excitation pulse takes the tissue longitudinal magnetization to the transverse plane and a fast EPI readout is used to acquire an image.

The physiological mechanism that produces the VASO contrast is based on the vasodilatation of small vessels and capillaries during increased neuronal activity (101). It is estimated that for a given volume of cerebral tissue, the fraction of blood at rest is 4.5% (103). During activation, the fraction of blood in the tissue increases as consequence of CBV increase. Since the blood signal is nulled, the fractional increase of blood in the tissue generates a MR signal loss in an opposite manner as observed in BOLD-fMRI signal. The CNR of VASO-fMRI is intrinsically low as compared to BOLD due to the small fraction of blood in the tissue, which yields MR signal changes of approximately 1.5-2% at 3T (102). Yet, it has been shown that VASO-fMRI is capable of detecting stimulus induced CBV changes in human fMRI studies (6,101,104–106).

VASO-fMRI allows the calculation of Δ CBV from VASO signal changes (101). First, it is necessary to define the vascular-space-occupancy of a particular microvessel (ξ_i), defined by equation 3.2, where V_{par} indicates parenchymal volume (ml tissue/g tissue) and CBV is the cerebral blood volume (ml blood/g tissue). Thus, the units of ξ are ml blood/ml parenchyma.

$$\xi_i = \frac{CBV_i}{V_{par}} = \frac{CBV_i}{\left(V_{tissue} + \sum_i CBV_i \right)} \quad (3.2)$$

For pure brain parenchyma, the MR signal (S) is proportional to the sum of the magnetization contributions of microvessel (i =arterioles, capillaries and venules) and pure tissue. For a nonselective IR followed by a slice-selective excitation and GE detection, the signal is given by equation 3.3, in which C is the water density of microvascular blood in ml water/ml blood, $T_{2,blood,i}^*$ and $T_{2,tissue}^*$ are the effective transverse relaxation constants of blood and tissue, respectively.

$$S_{par} = S_{blood} + S_{tissue} \approx \left(\sum_i \xi_i C_{blood} \right) \cdot M_{blood,i}(Ti) \cdot e^{-TE/T_{2,blood,i}^*} + \left(C_{par} - \sum_i \xi_i C_{blood} \right) \cdot M_{tissue}(TI) \cdot e^{-TE/T_{2,tissue}^*} \quad (3.3)$$

For proper blood nulling ($M_{\text{blood},i}(\text{TI})=0$), equation 3.3 can be rewritten as below, where $\xi = \sum_i \xi_i$ is the total microvascular space occupancy.

$$S_{\text{par}} \approx \left(C_{\text{par}} - \sum_i \xi_i C_{\text{blood}} \right) \cdot M_{\text{tissue}}(\text{TI}) \cdot e^{-\text{TE}/T_{2,\text{tissue}}^*} \quad (3.4)$$

The fraction parenchymal signal change during increased neuronal activity can be calculated as:

$$\begin{aligned} \frac{\Delta S}{S} &= \frac{S_{\text{par}}^{\text{act}} - S_{\text{par}}^{\text{rest}}}{S_{\text{par}}^{\text{rest}}} \\ &= \frac{(C_{\text{par}} - \xi^{\text{act}} C_{\text{blood}}) e^{-\text{TE}/T_{2,\text{tissue}}^{\text{act}}} - (C_{\text{par}} - \xi^{\text{rest}} C_{\text{blood}}) e^{-\text{TE}/T_{2,\text{tissue}}^{\text{rest}}}}{(C_{\text{par}} - \xi^{\text{rest}} C_{\text{blood}}) e^{-\text{TE}/T_{2,\text{tissue}}^{\text{rest}}}} \end{aligned} \quad (3.5)$$

The VASO signal change also carries the effect of extravascular BOLD changes. Assuming that at short TE and low field strength, the effect of the extravascular BOLD T2* change in the tissue can be neglected (101) and rewriting

$$e^{-\text{TE}/T_{2,\text{tissue}}^{\text{act}}} = e^{-\text{TE}/T_{2,\text{tissue}}^{\text{rest}}} \cdot e^{-\Delta\text{TE}/T_{2,\text{tissue}}^*} \quad (3.6)$$

the fractional signal change is simplified to the expression from equation 3.7. Thus, it is possible to estimate CBV changes ($\Delta\xi$) based on the relative VASO signal change, the vascular-space occupancy at rest (ξ^{rest}) and the water density of blood (C_{blood}).

$$\frac{\Delta S}{S} = \frac{(\xi^{\text{rest}} - \xi^{\text{act}}) C_{\text{blood}}}{C_{\text{par}} - \xi^{\text{rest}} C_{\text{blood}}} = \frac{-\Delta\xi \cdot C_{\text{blood}}}{(C_{\text{par}} - \xi^{\text{rest}} C_{\text{blood}})} \quad (3.7)$$

One limitation of VASO-fMRI is the limited number of slices that can be read within one TR, since the optimal TI condition is achieved only at single times. One simple strategy suitable for functional experiments (high temporal resolution is desired) is to limit the number of slices to three for each TR, the mid one at the theoretical optimal TI, one 50 ms before (approximately the readout time for a slice) and another 50 ms after the TI, so the contamination of blood signal can be neglected.

3.5 Arterial Spin Labeling

As discussed on chapter 1, the CBF has a fundamental role in brain homeostasis and a good characterization of its features is essential for understanding brain physiology. Arterial Spin Labeling is a quantitative MR technique that offers the great feature of measuring non-invasively the absolute cerebral perfusion, in milliliters of blood per gram of tissue per unit of time, with improved resolution as compared to other traditional techniques such as PET and Single Photon Emission Computerized Tomography. Instead of using contrast injection and ionizing radiation, the water in the blood is magnetically labeled and used as endogenous contrast, which allows multiple repetitions without the limitations associated with dose accumulation or gadolinium bolus tracking MRI (e.g. Dynamic Susceptibility Contrast, Dynamic Contrast Enhancement). An ASL experiment consists of acquiring multiple pairs of labeled and control images using a snapshot imaging technique such as EPI. Labeled images are acquired subsequently to the labeling of the blood water after a time period name post labeling delay. Due to the blood perfusion in the imaging volume, the tissue signal acquired will include a contribution from labeled blood water spins, whereas control images are acquired without blood labeling. The subtraction of the labeled image from the control of each pair results in multiple perfusion-weighted (pw) images (Fig. 3.4) that are averaged in order to increase SNR and then scaled according to quantification models (107) to yield a CBF map in absolute units. A proton density image can be also acquired to be used in the quantification process, however it has been shown that the use of the mean control images yield similar results (108).

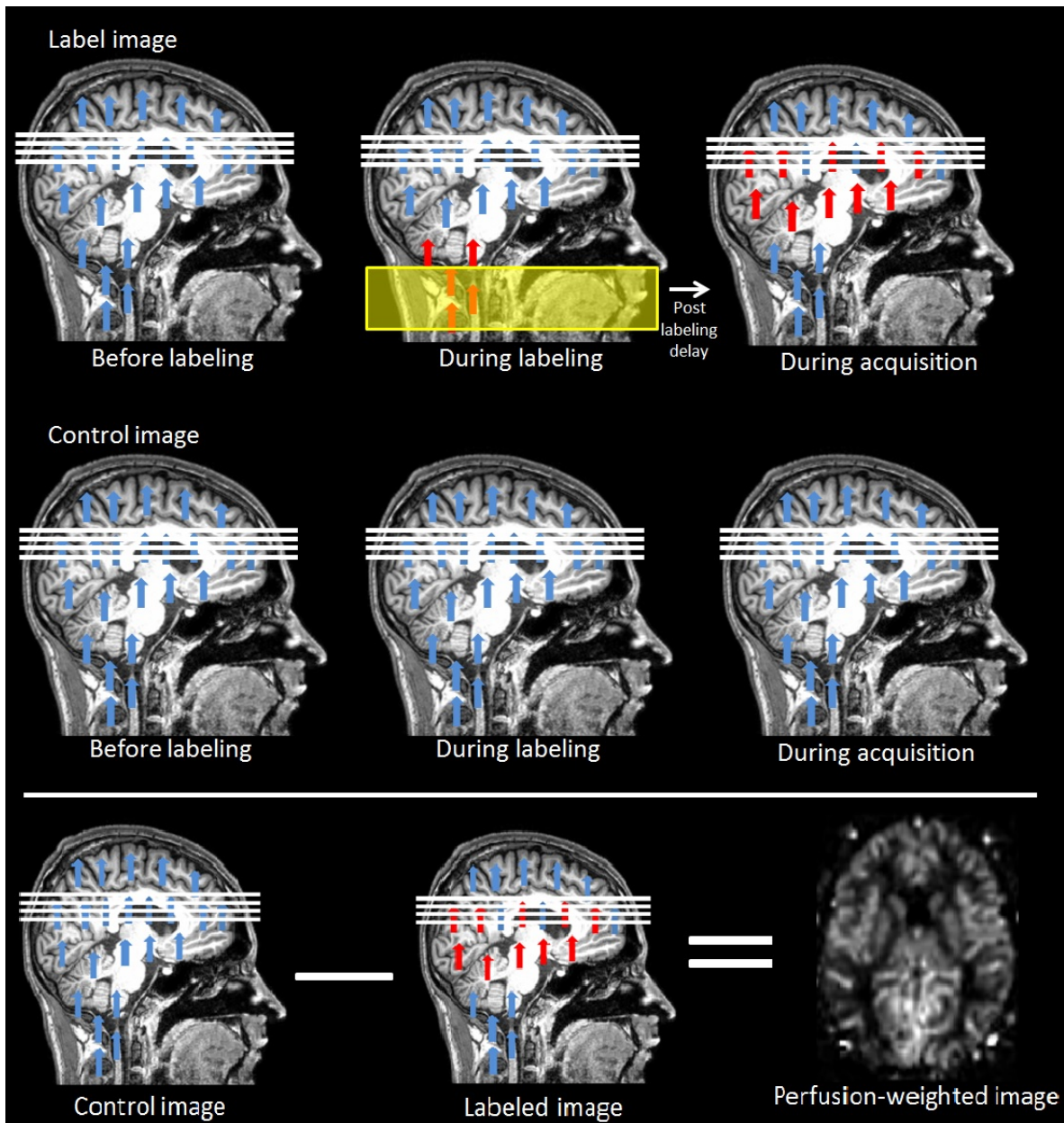


Figure 3.4. A simplified schematic representation of the events during the acquisition of control and labeled images from ASL and the subtraction for the perfusion weighted image. First line contains the image label acquisition events, whereas control image is shown in the second line. The third line shows a representation of the subtraction between control and labeled images and an example of perfusion-weighted image. The image slices positioning is represented by white bars; the labeling band is represented as a yellow rectangle in the neck; arrows indicate the spins and those whose magnetization was inverted are painted in red.

Based on the labeling method, ASL technique can be divided into 3 different categories: Pulsed ASL (PASL), Continuous ASL (CASL) and Pseudo-continuous ASL (pCASL). The PASL technique consists in using a short RF pulse to create a large labeling

band at the neck level and tag a large volume of spins in a single shot. The echo planar imaging and signal targeting with alternating radiofrequency (EPSTAR) was the first pulsed labeling scheme (109) and remains commonly used until the present. A 180° RF pulse is applied together with a gradient to invert the longitudinal magnetization in a slab below the imaging volume (towards the neck). On the arrival time in the tissue, the longitudinal magnetization of the labeled blood will be smaller (i.e. has become less negative as result of the inversion during labeling) due to T1 relaxation, thus different from the fully relaxed magnetization of the tissue. During the control image acquisition, an inversion slab is placed superior to the image where there is no inflowing blood in order to cancel magnetization transfer (MT) effects (110). In the CASL technique, for a few seconds a small RF field (inversion plane) continuously saturates (111) or invert (112) the longitudinal magnetization of water protons in the blood entering the brain. Flowing spins in the arteries move through the field gradient and their resonant frequency increases. As they pass through resonance the magnetization is inverted. The long labeling period as compared to PASL can cause substantial magnetization transfer effects in macromolecules of the static tissue from the image slice, which results in attenuation of the free water signal (113). It is essential that control images have the same MT effect so it can be cancel during the image subtraction, so one solution for this CASL issue is to use a small dedicated coil around the neck for labeling (114) that does not have enough power to saturate the image slice, although it demands extra hardware. Another possibility is a double inversion pulse that will leave the blood water magnetization effectively uninverted (115). Even though CASL generates better contrast to noise ratio (CNR) due to the larger number of spins labeled, the technique yields in large power deposition as compared to PASL, a problem that increases in higher field strengths. Aiming to improve CNR but maintaining power deposition as low as possible, the pCASL technique proposes the use of a train of short pulses in combination with rephased gradients to adiabatically invert the inflowing spins (116), instead of a long rectangular labeling pulse as used in traditional CASL. Wu et al. (2007) compared pCASL with standard PASL and CASL at 3T, and showed that pCASL provides a 50% improvement in SNR compared to PASL and an 18% increase in labeling efficiency compared to CASL. However, both CASL and pCASL demand longer TR (3-5 seconds) as compared to PASL due to the labeling time. This limitation makes PASL more

suitable for functional studies, since better temporal resolution is necessary to characterize the vascular response.

In order to quantify CBF in absolute units, it is necessary to model the difference between control and labeled images (ΔM) as function of sequence and tissue parameters. Assuming water as a freely diffusible tracer ($M_v=M/\lambda$), the longitudinal Bloch equation that includes the effect of tissue perfusion (f) is given by equation 3.8 below (117), where M , M_a and M_v are the longitudinal magnetizations of tissue water, arterial and venous blood, respectively, M_0 in the equilibrium magnetization, T_1 is the longitudinal relaxation time of brain water and λ is the brain-blood partition coefficient of water.

$$\frac{dM(t)}{dt} = \frac{M_0 - M(t)}{T_1} - f M_a(t) - \frac{f}{\lambda} M(t) \quad (3.8)$$

In the absence of inversion (control image), $M_a(t) = M_a^{(0)}$, $M(t=0)=0$ and the time dependent solution to the Bloch equation is $M_{ctrl}(t) = M_0(1 - e^{-t/T_{1app}})$, where the apparent relaxation time is given by $1/T_{1app}=1/T_1+f/\lambda$. When the inversion pulse is applied, the magnetization of arterial blood is inverted, hence relaxing with a T_{1a} . Assuming that T_{1a} is constant throughout the inverted slice, equation 3.8 must be solved under the following conditions: $M_a(t) = M_a^{(0)}(1 - 2\alpha_0 e^{-t/T_{1a}})$, $M(t=0)=0$ and equation 3.9 below:

$$\alpha_0 = \frac{M_a^{(0)} - M_a(t=0)}{2M_a^{(0)}} \quad (3.9)$$

The time dependent magnetization for the inversion condition (labeled images) is given by equation 3.10:

$$M(t) = M_0(1 - e^{-t/T_{1app}}) - 2\alpha_0 M_0 \frac{f(e^{-t/T_{1app}} - e^{-t/T_{1a}})}{\lambda \left(\frac{1}{T_{1a}} - \frac{1}{T_{1app}} \right)} \quad (3.10)$$

Thus, the difference between control and label experiment is given by Equation 3.11 and therefore, CBF (the variable f , tissue perfusion) can be quantified.

$$\Delta M(t) = 2\alpha_0 M_0 \frac{f(e^{-t/T_{1app}} - e^{-t/T_{1a}})}{\lambda \left(\frac{1}{T_{1a}} - \frac{1}{T_{1app}} \right)} \quad (3.11)$$

3.6 Oxygen consumption estimation

The $CMRO_2$ is a physiological parameter of great interest as it is tightly linked to tissue energy utilization rates, hence neuronal activity. However, measuring $CMRO_2$ is not a simple task (9). The current standard method for measuring $CMRO_2$ is PET, yet it requires three separate measurements following injection of ^{15}O labeled O_2 , water and carbon monoxide and analysis of the dynamic tissue concentration curves within a theoretical framework that accounts for the combined effects of $CMRO_2$, CBF and CBV on the observed tracer kinetics (118). One complication for deriving $CMRO_2$ from PET experiments arises from the fact that it is not possible to differentiate oxygen nuclei in O_2 form or in the water molecule, after being metabolized.

More recently, NMR techniques have also allowed the measurement of $CMRO_2$. Even though ^{17}O NMR has received little attention as compared to other nuclei, it offers the unique feature of measuring non-invasively $CMRO_2$ (119). Despite its high cost, more studies have focused on exploring the possibilities offered by ^{17}O NMR (119,120). A more popular NMR approach involves the mathematical modeling of blood oxygenation in combination with CBF and BOLD measurements in the so called calibrated-BOLD technique (29). The most utilized mathematical framework is the Davis model (13), which is based on physical reasoning and Monte Carlo simulations. Despite its relative simplicity as compared to more sophisticated models that require a larger number of variables as input, it has proven to be more robust than one might have expected given the restrictive assumptions that relies on (121). The Davis model assumes that the BOLD effect manifests through changes in transverse relaxation rate ($\Delta R2^*$), which is linearly dependent on the blood volume fraction (f_v) and dependent on magnetic susceptibility difference between blood and tissue ($\Delta\chi$), raised to power β . The susceptibility difference is proportional to dHb and has a supralinear effect: linear large vessel component is combined with small vessel contributions. Monte Carlo NMR simulations revealed that $\beta=1.5$ fits the simulated $\Delta R2^*$ versus $\Delta\chi$ curve (122). The mass-balance principle reveals that oxygen delivery is proportional to both CBF and arteriovenous oxygen difference, thus Fick's law can be used to describe conservation of oxygen delivery and uptake: $dHb \propto CMRO_2/CBF$, or in terms of physiological variables:

$$\Delta R_2^*(t) \propto f_v(t) \left(\frac{CMRO_2(t)}{CBF(t)} \right)^\beta - f_v(0) \left(\frac{CMRO_2(0)}{CBF(0)} \right)^\beta \quad (3.12)$$

Defining B_t , F_t , V_t and $rCMRO_2$ as the BOLD signal, CBF signal, CBV at time t normalized by ratio to a baseline period, and assuming small change in relaxivity ($TE \cdot \Delta R_2^* \ll 1$) so the BOLD signal is $B_t \cong 1 - TE \Delta R_2^*(t)$, equation 3.12 can be rewritten as:

$$B_t - 1 \propto f_v(0) \left(\frac{CMRO_2(0)}{CBF(0)} \right)^\beta \left[1 - V_t \left(\frac{rCMRO_2(t)}{F_t} \right)^\beta \right] \quad (3.13)$$

CBV can be expressed in terms of CBF using the Grubb coefficient (α) (123): $V_t = F_t^\alpha$, and the baseline values are usually aggregated into a single calibration parameter $M \propto f_v(0) (CMRO_2(0)/CBF(0))^\beta$. In order to remove the proportionality of the expression, it would be necessary to add constants for magnetic susceptibility of dHb, susceptibility effects on transverse relaxation and echo time dependence. M is dependent on baseline tissue dHb and other baseline parameters; hence it may vary between trials and brain regions. In order to estimate M , a hypercapnic experiment is performed where CO_2 inhalation is used to evoke a vascular response without increase in neuronal activity, yet assuming there is no significant increase in metabolic rate over baseline (124,125). Equation 3.13 can be adapted to determine its implicit proportionality constant including baseline values:

$$M = \frac{B^H - 1}{1 - F^{H-(\beta-\alpha)}} \quad (3.14)$$

where B^H and F^H are BOLD and CBF ratios obtained during the hypercapnic experiment. Once M is known, normalized BOLD and CBF time courses from a functional experiment can be used to compute dynamic changes of $rCMRO_2$ using equation 3.15:

$$rCMRO_2(t) = F(t)^{1-\alpha/\beta} \left(1 - \frac{B(t) - 1}{M} \right)^{\frac{1}{\beta}} \quad (3.15)$$

Unlike the parameters α and β which are usually assumed to be constants, it is critical to measure M for each brain location and particular experimental acquisition. Indeed M depends on baseline physiology (baseline venous CBV, hematocrit) and sequence

parameters (e.g. TE, field strength). The assumption that hypercapnia does not alter $CMRO_2$ remains controversial (126–128), although if necessary it can be taken into account during M calculation. Other limitations of the Davis model are: it only considers extravascular signals (122); it neglects the possibility that changes in dHb containing CBV (capillary and venous) may be proportionally smaller than the arterial CBV (21,129); and it ignores the possibility that differences in the intrinsic signal between blood and tissue may change the overall signal upon neuronal activation (volume exchange effects) (130–132). Another critical limitation from the Davis model is the assumption that the arterial blood saturation is 100% and all dHb in the venous blood is generated through OEF and oxidative metabolism. However, in conditions such as hypoxic hypoxia, the dHb content in the arterial blood is not zero, and consequently not all dHb in the venous blood comes from metabolism.

Lu et al. (2004) proposed the acquisition of BOLD, CBF and CBV (using VASO technique) and a more complex theoretical framework to estimate $CMRO_2$. Considering two microvasculature compartments, namely an arterial one (a, 30%) in which the effective relaxation rate (R_{2a}^*) does not change during activation and a venular one (v, 70%) where the relaxation rate (R_{2v}^*) is sensitive to OEF change during activation, the BOLD signal can be written as:

$$S \approx 0.3xM_a e^{-R_{2a}^*TE} + 0.7xM_v e^{-R_{2v}^*TE} + (1-x)M_t e^{R_{2t}^*TE} \quad (3.16)$$

where x is the water fraction of the blood in the voxel, R_{2t}^* is the effective transverse relaxation rate in pure tissue, TE is the echo time. M_i (i=a,v or t) are magnetizations defined by sequence and tissue characteristics:

$$M_i = \frac{1 - e^{-R_{1i}TR}}{1 - \cos(FA) e^{-R_{1i}TR}} \sin(FA) \quad (3.17)$$

where R_{1i} is the longitudinal relaxation rate ($1/T_{1i}$), FA is the flip angle and TR is the repetition time. During neuronal activation the BOLD signal change is given by Equation 18. Indexes act and rest indicate activation and rest, respectively.

$$\frac{\Delta S}{S} = \frac{0.3 \Delta x M_a e^{-R_{2a}^*, rest TE} + 0.7 M_v (x^{act} e^{-R_{2v}^*, act TE} - x^{rest} e^{-R_{2v}^*, rest TE})}{0.3 x^{rest} M_a e^{-R_{2a}^*, rest TE} + 0.7 x^{rest} M_v e^{-R_{2v}^*, rest TE} + (1 - x^{rest}) M_i e^{-R_{2i}^*, rest TE}} + \frac{M_i e^{-R_{2i}^*, rest TE} [e^{-\Delta R_{2i}^* TE} (1 - x^{act}) - (1 - x^{rest})]}{0.3 x^{rest} M_a e^{-R_{2a}^*, rest TE} + 0.7 x^{rest} M_v e^{-R_{2v}^*, rest TE} + (1 - x^{rest}) M_i e^{-R_{2i}^*, rest TE}} \quad (3.18)$$

Using the expression below, Δx can be calculated from VASO signal changes (101):

$$\Delta x = x^{act} - x^{rest} = \left(\frac{C_{par} - CBV_{rest} C_{blood}}{C_{par}} \right) \frac{\Delta VASO}{VASO} \quad (3.19)$$

where C_{par} and C_{blood} are the water contents in ml water/ml substance for parenchyma and blood, respectively. The water fraction x can be calculated using CBV_{rest} values from literature (133) and the expression $x = CBV_{rest} \cdot C_{blood} / C_{par}$. The R_{2i}^* can be estimated from arterial (Y_a) and venous (Y_v) blood oxygenation (134):

$$R_{2i}^* = 17.5 + 39.1(1 - Y_i) + 119(1 - Y_i^2) \quad (3.20)$$

ΔR_{2i}^* can be also calculated using Y_v and the expression below (135):

$$\Delta R_{2i}^* = 0.7 \gamma B_0 \frac{4}{3} \pi \Delta \chi Hct (CBV_{act} (1 - Y_v^{act}) - CBV_{rest} (1 - Y_v^{rest})) \quad (3.21)$$

in which $\Delta \chi$ is the susceptibility difference between fully oxygenated and deoxygenated blood (136), and Hct is the hematocrit fraction of blood in microvasculature (137,138). By measuring Y_a , using previously measured Y_v^{rest} (104) and combining equations 3.17, 3.19, 3.20 and 3.21 to solve equation 3.18, it is possible to obtain Y_v^{act} . By using equation 3.22, one can estimate OEF (139):

$$(1 - Y_v) = 1 - Y_a + OEF \cdot Y_a \quad (3.22)$$

Since OEF represents the ratio between oxygen consumption and oxygen delivery, equation 3.23 can be modified when oxygen content ($Y \times Hct$) is constant to finally derive the $\Delta CMRO_2$ estimate, given by equation 3.24.

$$OEF = \frac{\text{oxygen consumption}}{\text{oxygen delivery}} = \frac{CMRO_2}{CBF \cdot Y \cdot Hct} \quad (3.23)$$

$$\left(1 + \frac{\Delta OEF}{OEF} \right) \left(1 + \frac{\Delta CBF}{CBF} \right) = \left(1 + \frac{\Delta CMRO_2}{CMRO_2} \right) \quad (3.24)$$

3.7 Magnetic Resonance Spectroscopy

While MRI focuses on providing structural and morphological information, MRS data offers a unique opportunity of non-invasively quantifying the concentration of metabolites, thus generating metabolic information about either healthy or diseased tissue. MRS from hydrogen nuclei (^1H -MRS) has been the most explored spectroscopic technique in the field of neurosciences, due to the relative large abundance of ^1H and higher gyromagnetic ratio as compared to other elements. However, other nuclei (e.g. ^{31}P , ^{13}C , ^3Li) can also allow the quantification of important metabolites and provide further information about the metabolism of the brain. Here we focus on single voxel ^1H -MRS, since higher SNR allows better temporal resolution, which is critical for functional studies.

The basis of MRS is the chemical shift contrast. As described in Section 3.1, the magnetic field created by electrons surrounding the nucleus opposes the main magnetic field, hence causing a small decrease in the effective magnetic field in the nucleus. Slightly different resonance frequencies are caused by this “shielding” of the surrounding electrons. Thus, different molecular structures with different geometry, nuclei position on the molecule and charge distribution generate resonance frequencies that can be measured and used to identify/quantify compounds. By convention, the chemical shift (δ) is defined by equation 3.25, where ω and ω_{ref} are the compound resonance frequency and the reference resonance frequency, respectively. Tetramethylsilane protons are often used as a reference compound as it produces a singlet and has great stability.

$$\delta = \frac{\omega - \omega_{ref}}{\omega_{ref}} \times 10^6 \quad (3.25)$$

The chemical shift allows the differentiation of molecules based on their resonance frequencies in the spectrum. Besides the electronic environment, the nucleus resonance frequency can also be affected by the magnetic moment of neighbor nuclei in a process called nuclear coupling. Interactions can occur directly through space (dipolar coupling) and also through electrons in chemical bounds (scalar or J-coupling) (140). Dipolar interactions are the main source of relaxation in liquids, although there is no net interaction between nuclei since rapid molecular tumbling averages the dipolar interactions to zero.

However, the scalar coupling is not averaged to zero, resulting in ordered division of the spectrum into triplets, quadruplets, doublet of doublet, etc (for a detailed review refer to deGraaf et al. (2007)) that can also be used to identify and characterize molecules. The scalar coupling constant characterizes the split of the peaks, which ranges between 1-15Hz for ^1H - ^1H interactions, and it is independent from the magnetic field.

Since the water concentration in the cerebral tissue is approximately 10.000 times larger than the metabolite concentrations, the water signal is suppressed during the acquisition of metabolic spectra. Indeed, the presence of water signal can distort ^1H spectra and make quantification much less reliable. The Variable Pulse power and Optimized Relaxation Delays (VAPOR) technique suppresses the water signal by employing a train of 8 narrow band chemical shift selective RF pulses centered on the water frequency and followed by a crusher gradient (141,142). The eight pulses power and delays are optimized such to reduce the water signal approximately to zero prior to the localization sequence. In addition to water signal suppression in the volume of interest (VOI), outer volume suppression (OVS) techniques (143) can be used to suppress any unwanted signal from outside the VOI. OVS bands, where a 90° excitation pulse is applied simultaneously with a magnetic field gradient, are strategically positioned around the VOI to suppress the magnetization that could potentially contaminate the signal coming from inside the VOI during its selection. Thus, OVS bands selectively remove unwanted signal and also reduce the demand of spoiling gradients during the localization sequence (141).

MRS signal acquisition involves specific pulse sequences for selecting the VOI, from which an echo is acquired and the spectrum generated after a Fourier transformation. The most common sequences for VOI selection are the Point Resolved Spectroscopy (PRESS) and Stimulated Echo Acquisition Mode (STEAM). The PRESS sequence consists of a spin echo sequence (SE) with an additional refocusing pulse (Fig. 3.5). The excitation and refocusing slice-selective pulses are applied orthogonally along the three logical gradients in order to only generate transversal magnetization in the VOI. Differently from imaging where gradients are also used for phase encoding, in single-voxel MRS all RF pulses are combined with magnetic field gradients for VOI selection and no gradient is used during the signal readout.

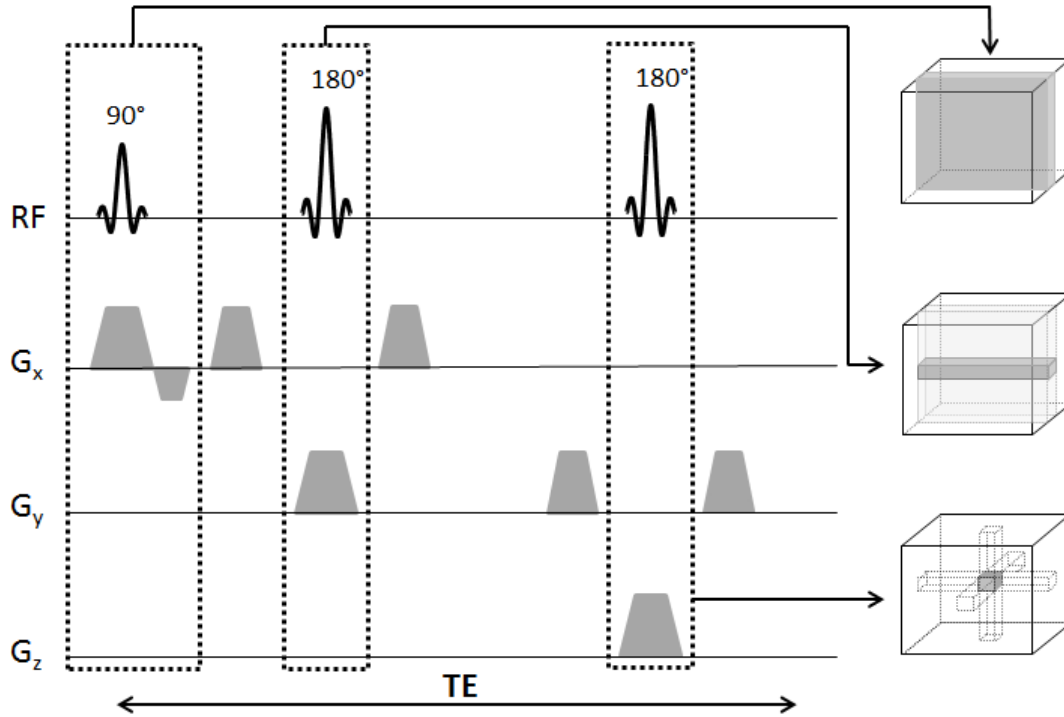


Fig. 3.5. Schematic representation of a single voxel PRESS pulse sequence.

The first echo obtained after SE contains the signal from a column generated by the intersection of the two orthogonal slices selected by the first two pulses. The last refocusing pulse selects the signal in the last remaining direction from the previously selected column and finally define the desired VOI. The PRESS sequence acquires the full signal intensity from the VOI, while no transverse magnetization remains outside the VOI due to the rapidly dephasing caused by the crusher gradients.

The STEAM sequence is composed by three orthogonal slice-selective 90° pulses that produce a stimulated echo from the VOI (Fig. 3.6).

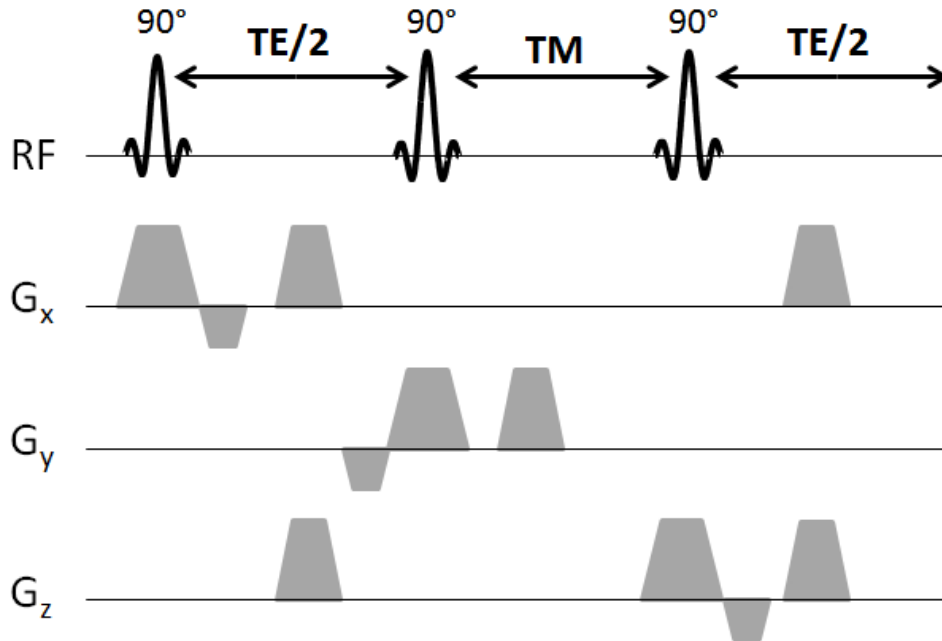


Fig. 3.6. Schematic representation of a single voxel STEAM pulse sequence.

The first excitation generates transverse magnetization in a plane of interest, and the second pulse flips the magnetization in the intersection column back to the original direction. During the mixing time (TM), crusher gradients are applied to rapidly dephase the remaining magnetization in the transverse plane while the signal of interest remains in the longitudinal plane. Finally, the last excitation rotates the remaining magnetization to the transverse plane. In between the second and third RF pulses, the longitudinal magnetization does not undergo R_2 relaxation, hence making STEAM recommended for the study of short T_2 compounds. One advantage of STEAM over PRESS is the possibility to achieve short TE, since STEAM does not use relatively long 180° pulses. TEs <10 ms are easily achieved using STEAM, minimizing the phase evolution of J-coupled resonances and signal loss through transversal relaxation (141). However, STEAM acquires only half of the total magnetization since the other half is dephased during TM.

The PRESS sequence offers much better SNR with a reasonable shortest TE (25-35ms depending on the scanner hardware) as compared to STEAM. However, the limited bandwidth of 180° pulses makes chemical shift displacement increase as the magnetic field gets stronger (>3 T). For this reason, the early human ^1H -MRS experiments at 7T were mainly conducted using STEAM despite the loss of signal (144,145). Better suited for high magnetic fields, the semi-LASER sequence (146) arises from a modification of

Localization by Adiabatic Selective Refocusing (LASER) sequence (147). The LASER sequence has its basic structure very similar to a PRESS sequence, but each excitation pulses is replaced by a pair of Adiabatic Full Passage (AFP) pulses (148), which have much broader bandwidth and are B1 insensitive, thus reducing the chemical shift artifact displacement. The semi-LASER sequence enables localization with full signal intensity, but with relatively shorter minimal TE (~ 30 ms with a surface coil) (149) as compared with traditional LASER sequence, since the first pair of AFP pulses is replaced by 90° slice-selective excitation pulse (Fig. 3.7). The semi-LASER sequence also carries the advantage that apparent T_2 relaxation times of metabolites are longer than those measured with conventional Hahn SE sequences (150), resulting in less signal attenuation in longer TEs. In addition, J-coupling evolution is minimized due to the series of 180° pulses that favors signal retention (149).

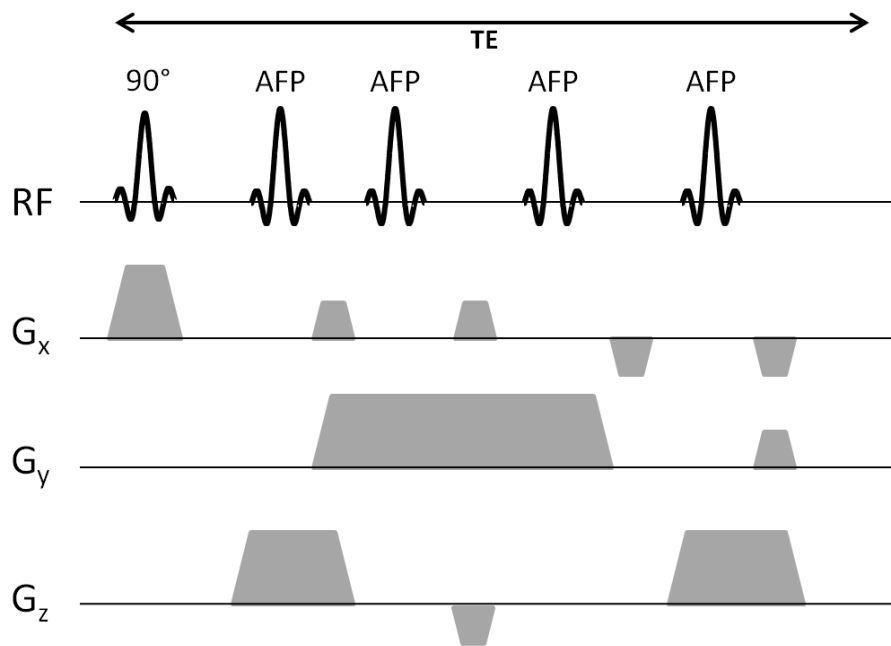


Fig. 3.7. Schematic representation of a single voxel Semi-LASER pulse sequence.

The use of high magnetic field is markedly beneficial for reliable quantification of metabolites due to increased SNR and larger chemical shift dispersion. It has been shown that at 7 T, a robust and accurate quantification up to 17 brain metabolites is feasible, which is very difficult to achieve at lower fields (145). This level of sensitivity is essential for fMRS studies, since stimulus-induced metabolic concentration changes are expected to be relatively small even as compared to the baseline concentrations, which are technically

demanding to be detected. Significant concentration changes of approximately 0.2 $\mu\text{mol/g}$ could be observed for several metabolites in the activated visual cortex during prolonged visual stimulation (151–154).

Prior to spectra analysis, certain post-processing steps are necessary in order to ensure reliable and accurate metabolite quantification. The intrinsic poor SNR caused by the low concentrations of metabolites of interest demands the acquisition of multiple FIDs that are averaged to result in a single spectrum. Physiological noise such as subject motion or frequency variations due to small breathing movements might result in frequency drift and phase variation along the repetition of multiple acquisitions, hence fine adjustment on phase and frequency between each individual scan is necessary for achieving optimal linewidths. After Fourier transformation, a robust singlet in the spectrum (e. g. NAA or Cr) can be used as a reference for alignment among all spectra. Phase correction can be performed with a multiple iteration algorithm that minimizes the residue between each iteration phase step and the temporary averaged spectrum.

Eddy currents rising from the rapid magnetic field variation generated by gradients can also introduce distortions in the spectra and increase linewidths. The acquisition of a free induction decay (FID) with unsuppressed water signal can be used in the post-processing to eliminate residual eddy current (155).

A typical ^1H spectrum at 7 T is acquired with 2048 points and a bandwidth of 4 kHz, resulting in a spectral resolution of approximately 2Hz. This resolution might be low for certain procedures, such as subtraction of spectra between two conditions. A commonly used method for artificially increase spectral resolution is to add zero points at the end of the FID, a processed called zero filling. No additional metabolic information is added to the spectrum after zero filling, but the gain in resolution can potentially improve mathematical procedures and the quantification process. Apodization is another mathematical tool to artificially increase SNR exploring the prior knowledge that FIDs are expected to be an exponential decaying function. It employs the product of the acquired signal with a filter function that enhances the signal of the FID simultaneously to attenuating the noise component. A typical filter function is the Lorentz-Gaussian transformation given by the term $e^{t/\alpha} e^{-t^2/\beta^2}$, where α and β are two adjustable parameters that affect the linewidth or the resolution, respectively. The apodization tool can also be used to manipulate and match

spectral linewidths, since events that cause changes in local susceptibility (e.g. BOLD effect, hypoxia) alters the linewidths due to T_2 variation, hence introducing bias in mathematical operations between spectra and the metabolic quantification.

In order to extract quantitative information about metabolites from MR spectra, it is necessary to calculate the area under the curve of a resonance peak, which is proportional to the metabolite concentration, within other factors (e.g. protons of the molecular structure, hardware gain). Analysis can be carried in the time or frequency domain using popular algorithms such as AMARES (Advanced Method for Accurate, Robust and Efficient Spectral) from MRUI (Magnetic Resonance User Interface, <http://www.jmrui.eu>) or a linear combination model of spectra from LCMoDel (156) software, respectively. The algorithm AMARES treats the acquired FID as a mixture of different decaying sinusoids that are characterized by frequency, a decaying constant, phase and amplitude. Constraints can be set for the characterization individual signals, but no prior knowledge is required as input. The time domain analysis benefits with the advantage of allowing the selection of specific ranges of the data for analysis, potentially avoiding unwanted areas with signal contaminations, but the quantification of highly overlapped signal and j-coupled resonances can become problematic. The linear combination method implemented in the software LCMoDel includes a large amount of prior information in the data base of spectrum models (basis set), which is B_0 and sequence dependent, but not subject or brain region specific. A complete basis set that provide good coverage of the neurochemical profile (including macromolecule and lipid signal characteristics from the region of interest) allows reliable metabolite quantification and reduces systematic errors in the fitting model (157).

The concentration of metabolites can be calculated by utilizing a reliably quantifiable resonance as an internal reference, such as water, total creatine or N-acetylaspartate (158). Water is the preferred reference as in vivo metabolite concentrations may be altered by different pathological conditions, age and brain region. A FID with no water suppression and OVS is commonly acquired so the water peak can be used as internal reference for absolute metabolite quantification.

Metabolite changes induced by stimulation can be investigated using fMRS. However, the demanding challenge of reliable and accurate quantification contributed to somewhat controversial results, in particular for lactate, until high fields had been utilized.

In summary, the different reports of brain lactate changes during stimulation range from the absence of changes to 2.5 fold increase (52,159–162). The inconsistencies of metabolite concentration changes due to activation is likely to arise from different factors: the low concentrations signals spread over several multiplets; concentration changes are small under activation; the small spectral range of $^1\text{H-MRS}$ inevitably leads to the overlap of resonances, hence making the quantification more complex. In addition to these issues, the lactate quantification can potentially suffer with lipid contamination from extra cerebral fat tissue at a similar spectral position. Therefore, an optimized MR system and a precise acquisition protocol are required for high sensitivity and reliable quantification. B_0 inhomogeneities must be minimized and efficient shimming procedure has crucial importance to take advantage of the gains provided by high field. Spectral quality must be guaranteed with specific requirements regarding sequence design (i.e. optimal crusher gradient order, OVS order), water suppression and chemical shift displacement.

CHAPTER 4 - MOTIVATION AND OBJECTIVES

A tight control of cerebral perfusion and oxygen supply is essential for brain function, since oxidative metabolism is the primary means of energy production of the human brain (11). Despite the devastating effects of intense hypoxia to cerebral tissue, moderate oxygen deprivation through short periods of time is frequent in chronic disorders such as obstructive sleep apnea, which affects 2 to 4% of adult population, and has been suggested to be a risk factor for morbidities such as hypertension and stroke (163–165). Moreover, hypoxic preconditioning, such as hypoxic training (166), and high altitudes (167) are common exposures to reduced oxygen availability. Yet, the effect of reduced oxygen availability in the bioenergetics of the brain is poorly understood.

Controlled mild hypoxia has been applied safely in human MRI studies of cerebral physiology. Studies have shown that hemodynamics, metabolism and higher brain functions are not disrupted even down to oxygen arterial saturation of 0.8 (1,168,169). Mild hypoxic hypoxia regulated by an inspired gas mixture containing 12% O₂ has been safely applied in studies in the past decade, leading to arterial oxygen saturation levels of approximately 85% without any related historic of discomfort (11,170–172). Few human brain studies have analyzed how physiological parameters related to the vascular response, such as BOLD, CBF, CBV and CMRO₂ are affected by mild hypoxia, both at baseline (i.e., in absence of external stimuli) and during increased neuronal activity (6,11,170–173). However, no studies have attempted to measure BOLD, CBF, CBV and CMRO₂ during the same experimental session within the same group of subjects. Results from literature are controversial: the amplitude of CBF and CBV responses is not affected by hypoxia (6,11,170–172), although BOLD amplitude has been reported to be not significantly affected (170,172) or decreased (6). Activated areas decrease in BOLD-fMRI during hypoxia as compared to normoxia is a consistent finding between studies (6,170–172), although CBF and CBV areas changes were reported to remain unaltered (11,170) or decrease (6,170–173) during hypoxia. Finally, two recent studies calculated estimates of Δ CMRO₂ due to stimulation based on the calibrated BOLD technique, which revealed a reduction of Δ CMRO₂ during mild hypoxia as compared to normoxia (174,175).

The characterization of the neurochemical profile of the activated cortex during mild hypoxia has been performed using ^{31}P and ^1H -fMRS at 3 and 1.5T, respectively (170,176). However, detecting functional concentration changes even without gas paradigms is remarkably difficult with the sensitivity provided by lower magnetic fields ($\leq 3\text{T}$). Hence, the use of ultra-high magnetic fields ($>3\text{T}$) combined with highly optimized sequences is extremely important to achieve greater sensitivity and reliably detect small metabolite concentration changes. The use of ultra-high magnetic fields together with functional designs have not been applied to investigate the effects of mild hypoxia in the human brain.

In this work we aimed at evaluating the impact of mild hypoxia on neurovascular coupling and metabolic outcomes. Our first objective was to characterize the impact of mild hypoxia on vascular parameters from a group of healthy young adult subjects (18-40 years old). More specifically, the characterization involved measurements of BOLD signal, CBF, CBV and CMRO_2 estimates in the visual cortex using quantitative fMRI techniques. The second objective was to characterize the impact of mild hypoxia in the neurochemical profile of the activated human brain visual cortex as measured by ^1H -fMRS, taking advantage of improved sensitivity of 7T in a similar group of healthy young adult subjects. The rationale for using a visual stimulation paradigm relies on the opportunity of evaluating whether oxygen availability is a limiting factor during increased energetic demands (i.e. increasing consumption to reduce even further oxygen availability). The visual cortex is commonly accepted to embody the general properties of cortical function. In addition, the anatomy of the human brain and the visual cortex is convenient from an experimental point of view, especially for fMRS experiments.

Identifying the impact of mild hypoxia on functional brain metabolism and vascular parameters in the healthy human brain is a crucial step for understanding basics aspects of cerebral bioenergetics that remains poorly understood and could potentially provide new insights for generating hypotheses in multiple patient populations that experience hypoxia as consequence of their pathological condition.

CHAPTER 5 - CHARACTERIZATION OF THE VASCULAR RESPONSE DURING HYPOXIA USING FMRI EXPERIMENTS

5.1 Methodology

5.1.1 Participants

Twelve subjects (mean age 27.4 ± 3.4 years, 10 males, 2 females) without history of neurological and respiratory abnormalities participated in the study. All subjects involved in this study were young adults in order to avoid potential age depend variability. The study was approved by the local ethics committee from University of Sao Paulo and all subjects gave written consent prior to their participation in the study.

5.1.2 Experimental design

Subjects were comfortably fitted with a mouthpiece and nose clip, and breathed a gas mixture containing adjustable content of high purity ($>99.99\%$) medical grade nitrogen and oxygen delivered through a closed plastic hose circuit. Two oxygenation states were created by adjusting the fraction of inspired oxygen: normoxia (room air equivalent – 21% oxygen) and mild hypoxia (equivalent to an altitude of approximately 4000 m – 12%). After normoxia acquisition, a 5 min interval (without removing the subject from the scanner and coil) was performed in order to have the subjects arterial blood oxygen saturation (SaO_2) stabilized into a new steady state (variations $<2\%$). A timeline diagram with the main events of an experimental session is shown in Fig. 5.1. A total flow of approximately 32 l/min was used in order to avoid gas rebreath. SaO_2 , heart and respiratory rates were monitored using a vital signs monitor (Veris, Medrad) over the entire experiment. Expired end-tidal CO_2 pressure (P_{ETCO_2}) was also measured, although due to the high flow available to the subject, the absolute P_{ETCO_2} value measured was partially diluted in the exciding gas flow. Three runs of visual stimulation in each of the two oxygenation states were performed, and fMRI data described in the section below were acquired.

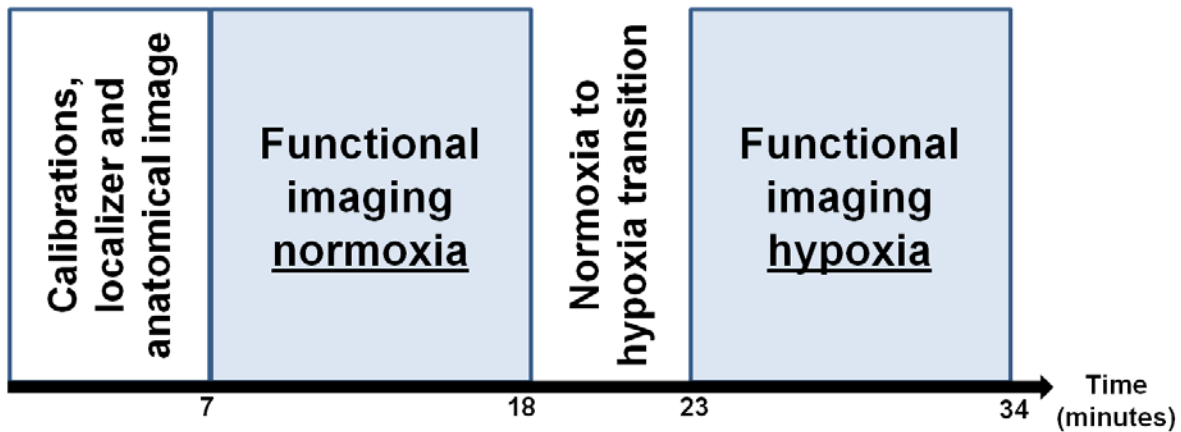


Fig. 5.1. Timeline diagram of events during an experimental session after subject positioning in the scanner.

Visual stimulus consisted of a black and white checkerboard flickering at 8 Hz, presented with use of Esys fMRI system (Esys fMRI, Invivo). Subjects were instructed to fixate on the center of the stimulus, and each run consisted of 7 blocks of 32 s each, alternating sequentially between rest and visual stimulation blocks. A black was presented during rest periods. The compliance to the research protocol was verified at the end of the experiment by asking the subject to report how many times a white cross positioned at the center of had become red over the entire experiment.

5.1.3 Data acquisition

MR experiments were performed using a 3 T scanner (Achieva, Philips Medical Systems, Best, The Netherlands) and a 8-channel volume head coil. High resolution three dimensional Magnetization-Prepared Rapid Gradient-Echo images (TR= 2500 ms, TE=3.2 ms, 7 ms echo time spacing, TI=900 ms, flip angle= 8°, isotropic resolution of 1x1x1 mm³ and 170 slices) were acquired and used to position the functional imaging volumes aligned to the calcarine sulcus to cover the visual cortex. Functional images (BOLD, ASL and VASO) were acquired using a GE and single shot EPI readout sequence and shared the same following parameters: TR=2000 ms, Sensitivity Encoding factor=2 and resolution of 3x3x5 mm³. Specific parameters: BOLD images had a TE=40 ms and 5 slices; ASL images were acquired using EPSTAR (177) labeling scheme (post labeling delay=1500 ms, labeling volume of 200 mm positioned at the neck level), TE=18 ms and 3 slices; VASO images were acquired using an inversion pulse and TI of 700 ms for nulling blood signal

(101), TE=18 ms and 3 slices. BOLD and VASO consisted of 112 volumes each, whereas ASL consisted of 56 pairs of control/label images for each oxygenation state. Functional runs were acquired in a pseudo-randomized scheme within each oxygenation state. The length of the periods in normoxia and mild hypoxia were approximately 18 and 16 minutes, respectively.

5.1.4 Data analysis

All processing was performed using SPM8 (Wellcome Department, University College London, UK) and in-house built Matlab (Matlabworks, Natick, MA) routines. All functional images were corrected for motion, coregistered to the anatomical image and normalized to the MNI standard brain space. Perfusion-weighted difference images from ASL (pwASL) were calculated by the pair-wise difference between control and label images. Due to lower SNR of pwASL, all functional images from the 3 different modalities were smoothed using a Gaussian kernel (full width at half-maximum of 5 mm) (170,171). BOLD activation maps were generated using a general linear model and the standard hemodynamic response function implemented on SPM8, whereas GLM for VASO and pwASL data had the standard 1st order gamma function from SPM8 as regressor. The activation threshold was set to $t=2.7$ for BOLD and VASO, whereas a threshold of $t=2.3$ was used for ASL due to reduced signal-to-noise ratio of pwASL data (170–172). Only voxels activated in all the three imaging techniques for each gas condition were used for the extraction of the mean time courses of BOLD, pwASL and VASO signals for each subject and the calculation of stimulus-induced changes of BOLD, CBF and CBV relative to baseline. Mean BOLD and VASO time courses were down-sampled to the same number of points from pwASL. Temporal smoothing using a moving average of 12 seconds (3 points) was performed in the time series. Finally, all series were normalized with respect to the last 24 seconds of baseline, which was defined as the first block of each run of visual stimulation. Relative CBF changes were defined as the normalized pwASL time course, and relative CBV changes were calculated using the normalized VASO signal time course and a model previously proposed (101). The BOLD signal change was extracted from the BOLD-fMRI images. The amplitude change of evoked BOLD, CBF and CBV responses due to visual stimulation were calculated by averaging the time course points from the last

20 s from each stimulation block in order to avoid the first transition seconds of the vascular response.

Relative CMRO₂ changes due to stimulation were calculated using the methodology proposed by (104) for both oxygenation states (equations 3.17 to 3.21). Constants used in the methodology are shown in Table 5.1. After temporal smoothing using a moving window of 16 seconds (4 points), the averaged time courses from the 50 voxels displaying activation with highest t-values in the overlapping region was used to calculate mean ΔBOLD, ΔCBF and ΔVASO relative changes (20). A correction for mild hypocapnia effect caused by the absence of CO₂ in the gas mixture was applied, which takes into account a 2.5% reduction of baseline CBV, a 10% increase in baseline CMRO₂ and 13% decrease in baseline CBF as previously shown in literature (127,178). In addition, previous studies reported an 18% increase in baseline CMRO₂ due to mild hypoxia (174,175), which was also taken into account in our calculations of stimulus induced changes.

Table 5.1. Constants used in Lu et al. (2004) methodology for CMRO₂ calculation

Variable	Value	Reference
Hematocrit	0.44	(137,138)
CBV during rest	0.05	(179)
R ₁ arterial blood in normoxia	0.61 s ⁻¹	(180)
R ₁ venous blood in normoxia	0.64 s ⁻¹	(180)
R ₁ tissue in normoxia	0.89 s ⁻¹	(134)
R ₂ tissue rest in normoxia	21.3 s ⁻¹	(134)
Venous blood saturation during rest in normoxia	0.49	Adapted from (121)
R ₁ arterial blood in hypoxia	0.62 s ⁻¹	(6)
R ₁ venous blood in hypoxia	0.68 s ⁻¹	(6)
R ₁ tissue in hypoxia	0.89 s ⁻¹	Same as normoxia (no ref.)
R ₂ tissue rest in hypoxia	23.90 s ⁻¹	(134)
Venous blood saturation during rest in hypoxia	0.33	Adapted from (121)
Arterial blood fraction	0.30	(181,182)
Venous blood fraction	0.70	(181,182)
C _{blood} (ml water / ml blood)	0.87	(101)
C _{tissue} (ml water / ml tissue)	0.89	(101)

5.1.5 Statistical analysis

Paired two-tailed t-test was used to determine the statistical significance of changes in amplitude and extension of the evoked BOLD, CBF and CBV responses between oxygenation states. A p-value inferior to 0.05 was considered to be significant. All reported values are given as mean \pm standard error of the mean unless otherwise specified.

5.2 Results

5.2.1 Physiological variables

The level of mild hypoxia used was well tolerated subjects, except for one subject that could not breathe comfortably through the mouthpiece and did not want to proceed with acquisitions. Two subjects reported a mild feeling of breathless during the beginning of the transition to mild hypoxia, which was completely overcome at the end of the transition period after the adaptation, and no other complains were reported. Hypoxia increased heart rate from 72.7 ± 3.8 to 78.6 ± 3.8 beats/min ($p < 0.01$), and SaO_2 decreased from $96.8 \pm 0.3\%$ to $81.1 \pm 0.4\%$ ($p < 0.01$). Mean respiratory rate and partial $\text{P}_{\text{ET}}\text{CO}_2$ during normoxia were 9.6 ± 0.5 breaths/min and 9.9 ± 0.7 mmHg for normoxia and 9.6 ± 0.6 breaths/min and 10.2 ± 0.7 mmHg for mild hypoxia, respectively. Both respiratory rate and $\text{P}_{\text{ET}}\text{CO}_2$ were not significantly affected by hypoxia.

5.2.2 Functional MRI

Complete data sets from 2 subjects were excluded due to excessive motion ($> 3\text{mm}$). The signal to noise ratio in the occipital lobe of functional images acquired during normoxia was not statistically different from those acquired during mild hypoxia. A non-significant trend for decrease of 2% in baseline EPI signal from BOLD images in the occipital cortex was observed during hypoxia as compared to normoxia. Typical BOLD, ASL and VASO images from a subject during normoxia are shown in Fig. 5.2.

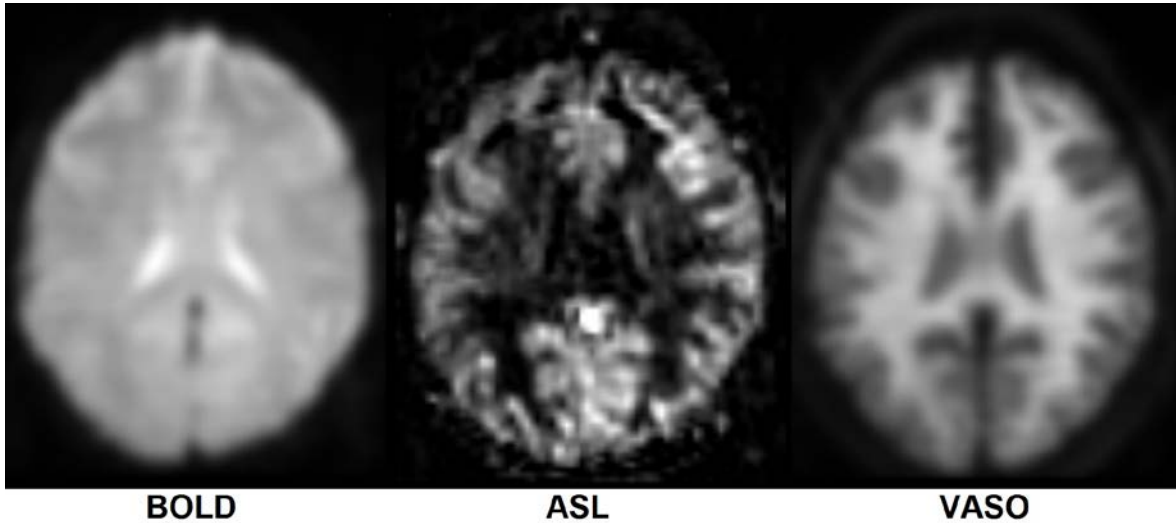


Fig. 5.2. BOLD, ASL and VASO images from a subject in normoxia.

Typical activation masks during normoxia and hypoxia for the 3 functional techniques are presented in Fig. 5.3. Areas recruited by visual stimulation were smaller during mild hypoxia as compared to normoxia: $-42.7 \pm 8.4\%$ for BOLD (N=9), $-33.1 \pm 8.0\%$ for ASL (N=9) and $-31.9 \pm 5.9\%$ for VASO images (N=7). Two VASO data sets were discarded due to software issues during the acquisition.

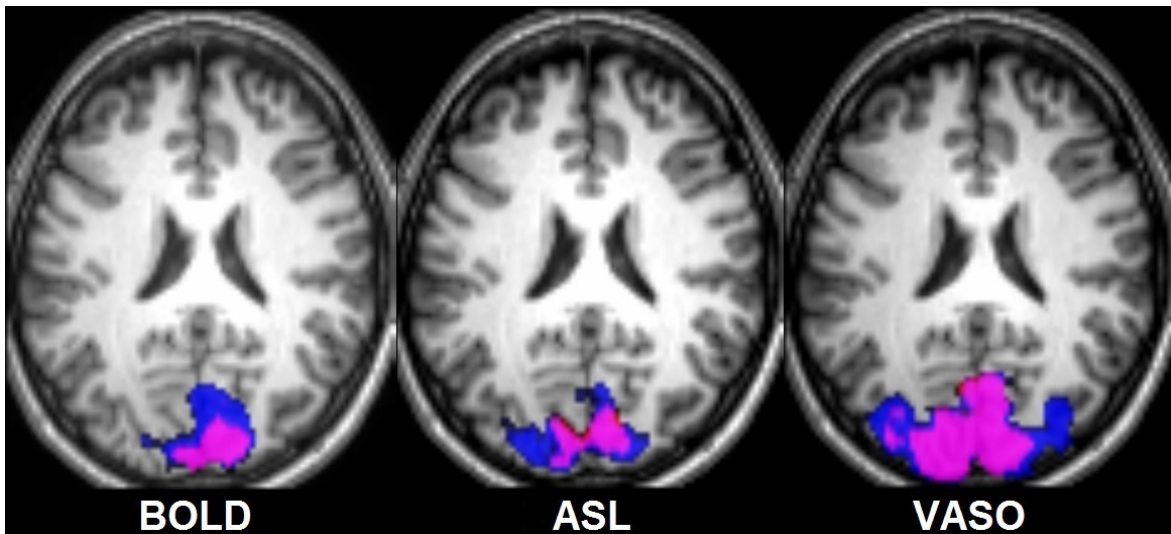


Fig. 5.3. Example of activation masks from BOLD, ASL and VASO from a single subject during normoxia (blue), mild hypoxia (red) and the overlap between areas (pink). Note that the hypoxia mask is almost entirely contained within normoxia mask, and red areas are practically absent.

Interestingly, the time courses extracted from common active areas to the three imaging contrasts during hypoxia revealed robust responses with similar amplitude for CBF

and CBV, but not for BOLD signal, which had amplitude notably reduced, as shown by Fig. 5.4. Percent changes of BOLD, CBF and CBV in both gas conditions are summarized in Table 5.2. No changes in the shape of evoked responses were observed. No statistically significant changes in baseline CBF were observed during mild hypoxia.

Table 5.2. Amplitude of evoked vascular changes due to visual stimulation

	BOLD (%)	Δ CBF (%)	Δ CBV (%)
Normoxia	4.1±0.6	61.7±16.1	29.2±16.7
Hypoxia	2.5±0.8 *	58.4±18.7	37.9±20.6

* $p < 0.01$, normoxia vs hypoxia, paired t-test. Mean \pm SD, $n=9$ for BOLD and Δ CBF, $n=7$ for Δ CBV.

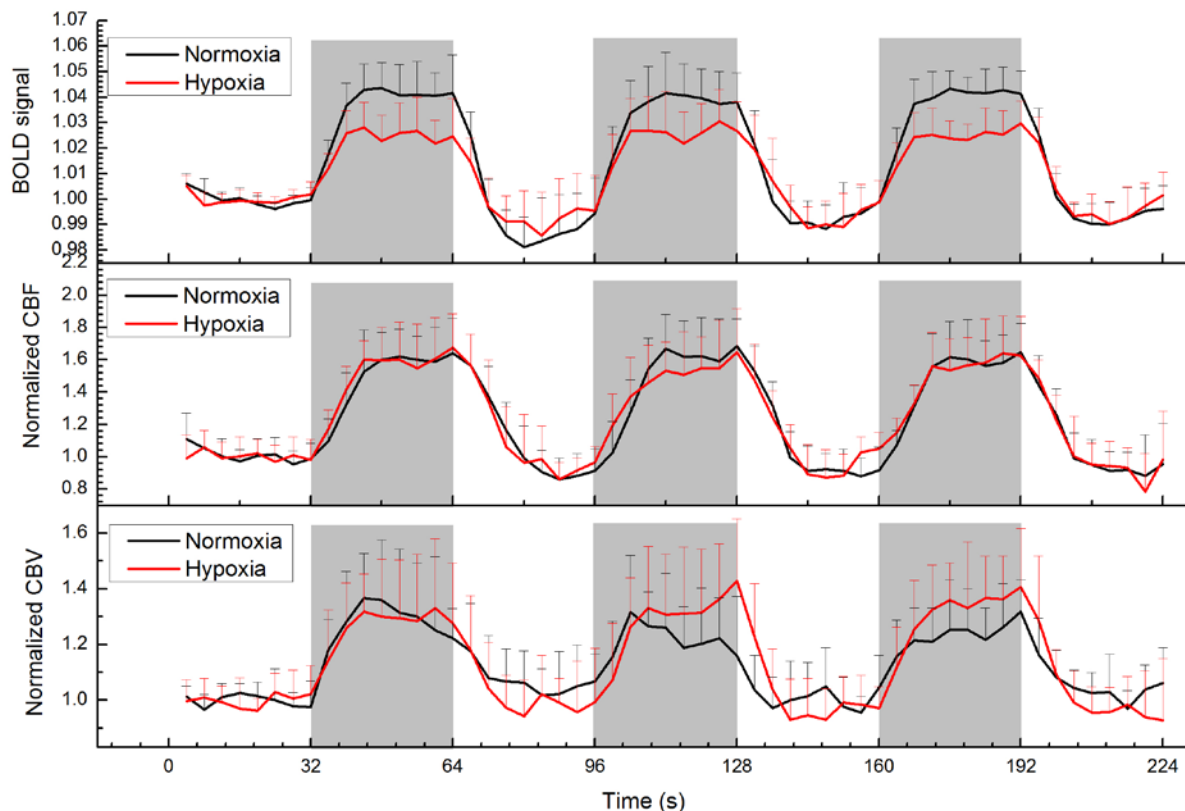


Fig. 5.4. Time courses of BOLD (N=9), CBF (N=9) and CBV (N=7) from the overlapping area between the 3 techniques for each gas condition averaged across trials and subjects. Data shown as mean \pm standard deviation. Areas in gray represent periods of stimulation.

5.2.3 Quantification of $CMRO_2$

The calculation of evoked $CMRO_2$ response due to visual stimulation using the methodology proposed by Lu et al. (2004) resulted in $\Delta CMRO_2$ of 15.5±5.7% in normoxia

and $3.1 \pm 1.9\%$ during hypoxia, which indicates a trend ($p=0.04$) of reduction during mild hypoxia.

5.3 Discussion

We examined the evoked BOLD, CBF, CBV and $CMRO_2$ responses to visual stimulus during normoxia and mild hypoxia. Our study focused on acquiring data sets from the 3 techniques from each subject within a single session in order to minimize variability. We observed a significant decrease in the extension of activated areas during mild hypoxia in all 3 imaging contrasts. Despite the extension decrease, only BOLD signal had reduced amplitude during hypoxia in the common active areas, whereas CBF and CBV responses had similar amplitude. The observation of smaller activated areas during hypoxia by using the same activation threshold (i.e. t-value) from normoxia suggests that areas active in normoxia but not in hypoxia (the blue areas visible in Fig. 5.3) did not exhibit a significant vascular response at the sensitivity level of our experimental conditions. Hence, a much smaller or absent vascular response was present in those areas during hypoxia, potentially indicating an altered neurovascular coupling.

A similar BOLD amplitude decrease during mild hypoxia has been observed in previous studies (6,176). One potential mechanism that could explain the baseline signal trend and the BOLD signal decreases during mild hypoxia is the intrinsic susceptibility change induced by reduced SaO_2 , which leads to a relative increase of deoxyhemoglobin concentration in the vascular compartments. Due to its inherent strong paramagnetic behavior, both baseline and stimulus induced BOLD signal changes can be affected (183).

Harris et al. (2013) reported a statistically significant increase of baseline CBF after a 20 minute mild hypoxia exposure, which was not detected in our data. The pseudo-randomized order of our acquisitions combined with a shorter mild hypoxic period did not allow us to detect and reproduce such finding.

Few studies performed multimodal-fMRI simultaneously to mild hypoxia in the same group of subjects (6,170–172), and most utilized only two of the three imaging techniques used in the present study. Sharing the same degree of mild hypoxia from our experiments, pioneer studies from Tuunanen et al. (2006) (170,172) reported similar decrease in the extension of the BOLD active areas, however unaltered amplitude changes

in the human motor and visual cortex in all active voxels, respectively. Additionally, another two studies reported changes in BOLD extension and amplitude in the visual cortex that are in good agreement with our findings (6,169,176). Regarding CBF, both fMRI (170,172) and PET studies (11) reported no changes in amplitude of the evoked response. Tuunanen et al. (2006) reported no amplitude changes in the visual cortex (170), although a 77% area reduction was observed in the motor cortex (172). Unaltered CBV amplitude in response to mild hypoxia is a consensus between studies (6,171,173), and extension changes reported by Ho et al. (2008) and Shen et al. (2012) are in excellent agreement with our results. Together with reports from literature, our findings suggest a reduction of the stimulus-recruited area during mild hypoxia as compared to normoxia, shown by our results of BOLD, ASL and VASO-fMRI. However, the recruited areas remain with similar evoked vascular response. Even though BOLD amplitude is altered, it is likely that such result is partially caused by a susceptibility effect. The trend for baseline EPI signal reduction of BOLD images itself does not explain the reduction on BOLD signal amplitude.

The combination of four potential mechanisms could be involved in the observed results: (i) a reduction of the neuronal population recruited by the visual stimulus; (ii) a heterogeneous reduction of oxygen metabolism in certain cortical regions, (iii) unwanted contribution of mild hypocapnia induced by the gas paradigm and (iv) a reduction of MR techniques sensitivity during mild hypoxia.

Mechanisms (i) and (ii): Tuunanen et al. (2006) reported no changes in visual evoked potential during mild hypoxia (170), and together with the observed BOLD extension reduction and unaltered CBF area extension, the authors suggest a highly heterogeneous oxygen extraction fraction (and consequently $CMRO_2$) throughout the cortex. Hence, there would be a lesser mismatch between CBF and $CMRO_2$ during mild hypoxia. However, previous studies that focused on analyzing the effects of mild hypoxia in the brain electrical activity showed both event-related brain potentials and reaction times altered during mild hypoxia as compared to normoxia (184–187). In another study, Tuunanen et al. (2006) reported a large decrease in both CBF and BOLD activated areas in motor cortex (172), which is compatible with our data from the visual cortex. In addition, invasive methods able to quantify partial pressure of oxygen in the cerebral tissue and CBF

provided findings that suggest a mismatch between metabolic and hemodynamic responses in the activated cortex (188).

Mechanism (iii): increased respiratory rate could potentially lead mild hypoxia and hence alter the vascular response. Mintun et al. (2001) observed a decrease in $P_{ET}CO_2$ by 2 mmHg during a similar degree of hypoxia utilized in this study as compared to normoxia, possibly caused by hyperventilation. However, in our study both respiratory rate and $P_{ET}CO_2$ were not affected by the oxygen availability since a high gas flow was provided to subjects. Even though we cannot rule out a small contribution of mild hypocapnia to the experiment, both gas conditions lead to similar ventilation responses. Therefore, we anticipate similar isocapnic states for both normoxia and mild hypoxia periods.

Mechanism (iv): as it pertains to the sensitivity of the techniques, it should be noted that the SNR of functional images were not affected by oxygen availability, thus we do not expect differences of sensitivity between normoxia and mild hypoxia periods. A higher deoxy/oxyhemoglobin ratio during mild hypoxia could potentially shorten baseline parenchymal T_2^* . Using a similar range of S_aO_2 , Tuunanen et al. (2006) observed a tendency for parenchymal T_2^* by 2 ms (170), which was argued to be too small to affect GRE-EPI sensitivity between the two different states and hence explain the BOLD related results.

A limited number of studies evaluated the effect of mild hypoxia in baseline $CMRO_2$, mainly due its technical complexity. Gold standard PET measurements are limited by the invasiveness, radiation exposure and dependence on complex mathematical models, whereas MRI methods involve acquisitions of multiple imaging contrasts and also relies on mathematical modeling. Sicard et al. (2005) reported unaffected baseline $CMRO_2$ in rats when exposed to 12% oxygen, however a large decrease was observed when oxygen level was lowered to 9%. In humans, Xu et al. (2012) reported a 5% increase in baseline $CMRO_2$ due to mild hypoxia, and decrease of 10 and 17% during hyperoxia with a gas mixture containing 50 and 98% of oxygen, respectively. Using a 2-day exposure to mild hypoxia, Smith et al. (2012) reported an 18% increase of baseline $CMRO_2$ in humans, which was postulated to be driven by a reduction of $P_{ET}CO_2$ due to ventilatory acclimatization. A trend of decrease in stimulus-induced $\Delta CMRO_2$ in the remaining active areas was observed during mild hypoxia in our data. Similar trends of reduction were

observed during prolonged 2 and 7-day high altitude hypoxia exposure (174,175). Interestingly, a more pronounced reduction was observed in the 2-day period, whereas acclimatization mechanisms might have played an important role in the longer 7-day period. Assuming the exact same increase in energy consumption due to stimulation from normoxia, the increased baseline CMRO₂ alone does not explain the reduced Δ CMRO₂ during mild hypoxia. Using ¹⁹F in anesthetized rats, Duong et al. (2001) confirmed that mild hypoxia reduces the oxygen availability not only in the vascular compartments, but also in the cerebral tissue. In addition, a hypercapnia induced CBF increase of 100% increased pO₂ in the tissue by 50%. The authors suggest that a neuronal induced CBF increase would elevate cerebral tissue pO₂ by 25% or more, since the increased oxygen consumption would facilitate diffusion. This finding supports the notion that a robust CBF increase is capable of promoting a large increase in oxygen concentration in the cerebral tissue. Our results indicate that during mild hypoxia, the similarly intense CBF response in the recruited areas would be capable of compensate for the reduced oxygen availability, despite the observed decrease in Δ CMRO₂.

It remains unclear whether smaller neuronal populations are recruited during hypoxia, in which case the energetic cost of activation is expected to be also reduced, or whether mild-hypoxia results in a different neurovascular coupling, in which case the functional energy demands should remain unchanged. Additional studies will be necessary to evaluate if the results herein presented are caused only by an altered vascular response or there are underlying neuronal and metabolic alterations.

5.4 Conclusion

Mild hypoxia did not augment the vascular response as if oxygen availability had become a critical limitation. In fact, mild hypoxia during visual stimulation produced substantial reductions in the activated volumes detected by BOLD, ASL and VASO images. However, active common areas to all three imaging contrasts showed unaltered CBF and CBV responses, but smaller BOLD signal. The source of BOLD signal decrease during mild hypoxia is possibly related to susceptibility effects generated by an increase in deoxy/oxyhemoglobin ratio and a lesser mismatch between oxygen delivery and oxygen consumption. In addition, stimulus-induced Δ CMRO₂ was smaller as compared to

normoxia in the remaining active areas. Yet, it remains unclear whether changes in the extension of vascular response are directly linked to reduced neuronal recruitment or to a new neurovascular coupling with similar neuronal recruitment but altered vascular response. The data presented herein suggest that a transitory ischemic event, which could potentially generate short term mild hypoxia, does not have a critical effect on the vascular response and oxygen metabolism of the core activated areas in healthy young adult subjects.

CHAPTER 6 - CHARACTERIZATION OF THE METABOLIC RESPONSE DURING HYPOXIA USING FMRS EXPERIMENTS

6.1 Methodology

6.1.1 Participants

Sixteen male subjects with perfect vision and no history of neurological and respiratory abnormalities were enrolled in this study. Four subjects did not feel comfortable in the scanner during mild hypoxia and the acquisitions were not complete. The data from twelve subjects (mean age 26 ± 6 years) was utilized in this study. The inclusion of only male subjects was a condition imposed by the Institutional Review Board in order to avoid the potential risk of exposing unaware pregnant women to mild hypoxia. All subjects involved in this study were also young adults in order to avoid potential age depend variability similarly to the study described in the previous chapter. All subjects gave informed consent using procedures, which followed the Code of Federal Regulations, approved by the Institutional Review Board: Human Subjects Committee of the University of Minnesota.

6.1.2 Experimental design

A tight regulation of O_2 and CO_2 levels was achieved by using a feed-forward gas delivery system (RespirActTM, Thornhill, Research Inc., Canada) that allows independent control of $P_{ET}CO_2$ and end-tidal partial pressure of O_2 ($P_{ET}O_2$) by manipulating the gas input on a breath-by-breath basis. Prior to entering the scanner room, subjects were fitted with a specialized rebreathing circuit and facemask (Thornhill, Research Inc., Toronto, Can.). The contact between mask and skin was sealed using adhesive dressing (Tegaderm 3M Healthcare, St. Paul, MN, USA) in order to prevent gas leakage. Subjects were familiarized with the experimental setup and had their initial baseline $P_{ET}CO_2$ measured before entering the scanner room. Participants respiratory rate (RR) was cued at 10 breaths/min using an auditory metronome played at the scanner room. Two gas conditions were defined based on the targeted $P_{ET}O_2$: normoxia (100 mmHg) and hypoxia (40-45 mmHg). The defined $P_{ET}O_2$ target for normoxia was selected to simulate room air oxygen concentration,

whereas the target for hypoxia was selected to generate arterial blood oxygen saturations in the range of 80 to 85%, similarly to the previous study. During both conditions $P_{ET}CO_2$ was held constant to each individual initial baseline value previously, and a 5 min adaptation period was performed during the transition from normoxia to hypoxia. Subject's heart rate (HR) and arterial blood oxygen saturation (SaO_2) were monitored using Magnetic Resonance (MR) compatible pulse oximeter (Nonin 7500 FO, Nonin Medical Inc., Minnesota, USA). The respiratory rate, $P_{ET}CO_2$ and $P_{ET}O_2$ data were recorded by RespirAct. One run of data acquisition was performed for each of the two oxygenation states, and MR data was acquired as described in the section below.

For the visual stimulation periods (STIM), subjects visualized a black and red checkerboard flickering at 7.5 Hz, presented with use of a LCD projector and a screen fixated in the head coil visible to the subject through an adjustable mirror. During rest conditions (REST), a black screen was utilized. Subjects were instructed to look to a fixation point at the center of the stimulus and the compliance to the research protocol was verified by asking the subject to press a button every time the fixation point rotated 45 degrees, present both at rest and stimulation periods.

6.1.3 Data acquisition

MR experiments were performed using a 7 T/90 cm magnet (Agilent/Magnex Scientific, Abington, UK) equipped with a gradient/shim coil (SC72, maximum gradient strength of 70 mT/m; maximum 2nd-order shim strength of 7 mT/m²; Siemens Medical Systems, Erlangen, Germany) that was interfaced to a Siemens Syngo console (Siemens Medical Systems). A half-volume quadrature transceiver RF coil combined with an 8-kW RF amplifier provided the transmit $B1^+$ field just above 40 μ T in the center of the occipital lobe.

High-resolution three dimensional Magnetization-Prepared Rapid Gradient Echo images (TR=2500 ms, TE=2.42 ms, 7.0 ms echo spacing, 1500 ms inversion time, and isotropic resolution of 1 mm³) were obtained to visualize the anatomical structure of the occipital cortex. The functional ¹H-MRS data were acquired using the full signal-intensity semi-LASER localization sequence (149) optimized for 7 T (TE=26ms and TR=5 seconds), combined with outer volume saturation and VAPOR water suppression (141). A VOI of

$2 \times 2 \times 2 \text{ cm}^3$ was carefully positioned in the primary visual cortex based on the anatomic landmarks discernible on high resolution anatomical images (Fig. 6.1).

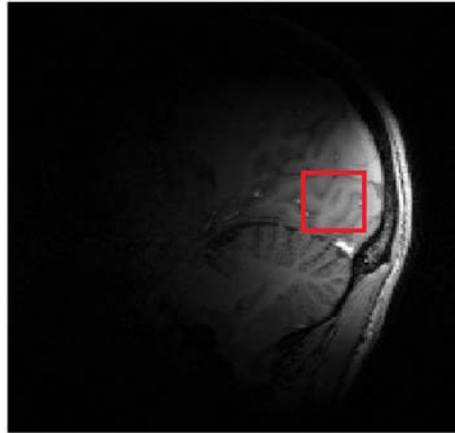


Fig. 6.1. Representation of VOI positioning in the occipital lobe.

The B0 field homogeneities were adjusted at the beginning of the experimental session using an echo-planar version of FASTMAP shimming method (189). In order to assess the BOLD effect on the water signal, a series of unsuppressed water spectra was acquired with the same semi-LASER sequence during a short visual stimulation session consisting of REST–STIM paradigm. The duration of each block was 30 s, and 6 scans were acquired per block. Finally, the metabolite spectra were collected during a 10 min fMRS visual stimulation paradigm, also consisting of a REST–STIM paradigm. The duration of each block was 5 min and 64 scans were acquired per block. In addition, four unsuppressed water signals were acquired and used as internal reference for absolute metabolite quantification and correction for effects of residual eddy currents. The acquisition of unsuppressed water signals for BOLD assessment, the metabolite spectra and the internal references were acquired under normoxia and hypoxia conditions. The timeline of main events from an experimental session of this study is shown in Fig. 6.2.

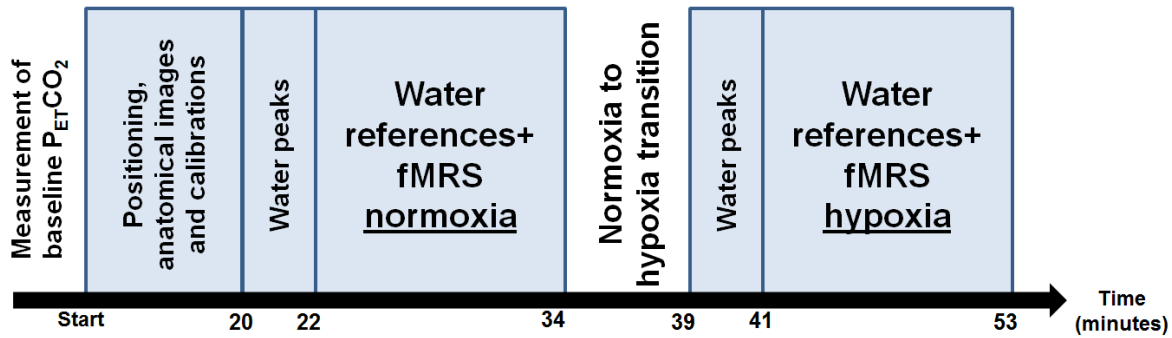


Fig. 6.2. Timeline diagram of events during an experimental session.

6.1.4 Data analysis

Acquired single scan FIDs were first corrected for small frequency and phase fluctuations, then summed (over 32 scans for each subject) and finally corrected for residual eddy currents (155) using in-house developed Matlab (MathWorks, Natick, MA) scripts. The intensity of the residual water signals was consistently below the level of metabolite resonances, hence the water signal removal was not necessary and potential baseline distortions were avoided. In order to avoid bias during quantification due to linewidth differences caused by susceptibility effects, all REST and STIM spectra from both gas conditions had linewidths matched to hypoxia REST (hypREST) spectrum linewidth by applying the necessary linewidth broadening estimated by calculating the linewidth difference between the two conditions. Linewidth estimation and broadening were performed using the same methodology previously described (154) that aimed at correcting the BOLD effect in spectra.

Metabolites were quantified from 32 scans spectra using LCModel (<http://www.s-provencher.com/pages/lcmodel.shtml>) with a basis set of 19 brain metabolite spectra simulated using a density-matrix approach plus a spectrum of fast relaxing macromolecules previously acquired (154). The unsuppressed water signal was used as an internal reference assuming 80% brain water content and 9% CSF fraction within the VOI (190). The metabolite concentrations were also corrected for transverse relaxation using simplified approximations (water $T_2 = 64$ ms, metabolites $T_2 = 107$ ms). For all metabolites except glucose (Glc), only concentration values quantified with Cramèr-Rao lower bounds (CRLB) below 50% were included into further analysis. Since the quantification of glucose at 7T is particularly challenging (145), we used slightly different selection criteria: an

average CRLB < 50% among the 4 representative spectra was utilized. From all metabolites included in the basis set, alanine and glycine were excluded entirely from the analysis following the CRLB criteria.

Finally, similarly to previous visual stimulation studies (151,154,191), all fMRS data acquired during the second halves of STIM and following REST periods from all subjects were summed accordingly, resulting in two spectra, STIM and REST, with 352 averages each (thus combined over 32 scans x 11 subjects) for both normoxia and hypoxia (group-level spectra). These spectra were used to generate activation-induced difference spectra. In order to eliminate the BOLD line-narrowing effect, an exponential multiplication was applied to the STIM FID data set to match the linewidth of the REST spectrum prior to the calculation of the difference spectrum. To confirm possible baseline metabolic concentration changes between normoxia and hypoxia, a baseline difference spectrum between normREST and hypoxia REST (hypREST) was calculated similarly to the activation-induced difference spectra previously described. Due to the line-broadening effect of hypoxia, normREST had its linewidth broadened and matched to hypREST, similarly to the BOLD line-narrowing effect correction. Metabolite quantification from the activation-induced difference spectra was performed by LCModel analysis with the basis set reduced to 4 metabolites (Aspartate (Asp), Glutamate (Glu), Lactate (Lac) and Glc), where two of them (Asp and Glc) were inverted. For the baselines difference spectrum quantification, a basis set with Asp, inverted Glu and glutamine (Gln) was utilized. The choice of metabolites to fit the difference spectra previously described was based on single subject analysis results and by the visual inspection of the difference spectra.

6.1.5 Statistical analysis

To determine whether physiological and metabolite changes between STIM and REST conditions were significant, paired two-tailed t-test ($\alpha = 0.05$) was utilized. In order to avoid possible transient effects in the metabolic responses, we averaged metabolite levels quantified only from the second half of the two STIM or following REST conditions (32 scans each) during the functional paradigm.

6.2 Results

6.2.1 Physiological variables

The mean difference between $P_{ET}CO_2$ during normoxia and hypoxia was 0.6 ± 1.9 mmHg, which demonstrates an excellent control of CO_2 levels in the gas mixture achieved by the computer-controlled gas blender. Average $P_{ET}O_2$ decreased from 106.0 ± 5.4 mmHg during normoxia to 44.2 ± 3.5 mmHg during hypoxia, which yielded on a SaO_2 reduction from $98.4 \pm 0.8\%$ to $82.1 \pm 1.4\%$ ($p < 10^{-5}$), similarly to the results obtained in the fMRI experiment. HR was significantly higher during hypoxia, varying from 69 ± 12 bpm during normoxia to 83 ± 17 bpm ($p = 0.002$) in hypoxia, whereas the respiratory rate was not affected by the gas condition (10.7 ± 1.4 bpm and 10.8 ± 1.1 bpm for normoxia and hypoxia, respectively). The mean baseline $P_{ET}CO_2$ was measured the scanner was 41.3 ± 3.0 mmHg. An increase in respiratory and heart rates are normal physiological responses to decreased SaO_2 during mild hypoxia, although only the second was observed in this study since subjects respiratory rate were cued by a metronome at 10 bpm in both gas conditions.

6.2.2 MRS findings

The data set from one subject was excluded from analysis due to lipid contamination that spoiled the spectra quantification quality. Effects of both stimulus-induced BOLD and susceptibility effects caused by hypoxia itself (i.e. higher deoxy/oxyhemoglobin ratio) were observed in spectra linewidths, as shown in Fig. 6.3. Linewidths of water peaks utilized for BOLD assessment were consistently larger in hypoxia as compared to normoxia during rest periods ($p < 10^{-4}$), with mean values of 13.9 ± 1.0 Hz and 15.3 ± 0.8 Hz, respectively. Concomitant creatine methyl signal linewidths were also increased during hypoxia (11.4 ± 0.8 Hz versus 12.5 ± 0.8 H, $p < 10^{-4}$). The BOLD effect on water peaks produced significant activation-induced linewidth changes during both gas conditions, although changes during hypoxia were significantly smaller than the observed in normoxia (0.45 ± 0.30 Hz and 0.21 ± 0.19 Hz, respectively, $p = 0.002$).

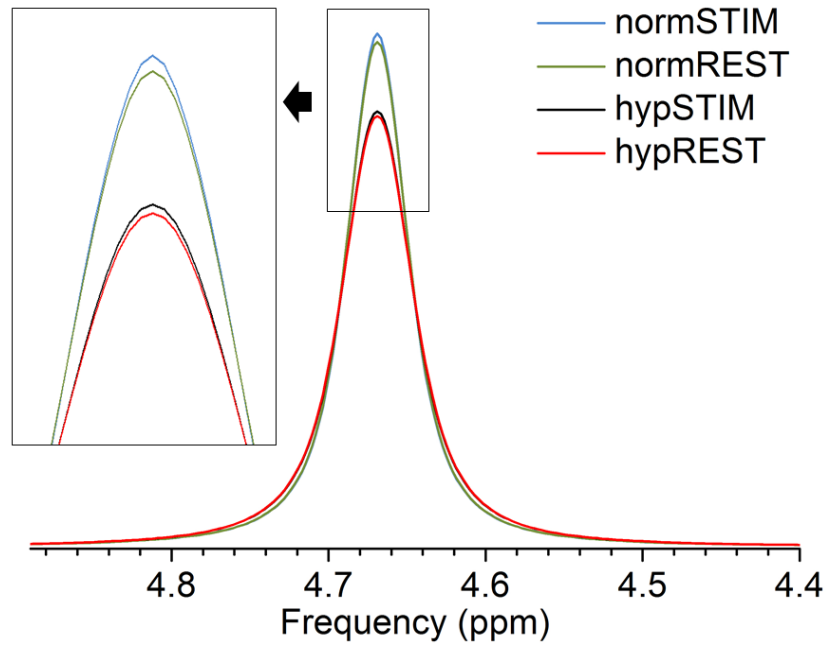


Fig. 6.3. Example of mean water peaks from a single subject exhibiting different linewidths due to BOLD and susceptibility effects generated by mild hypoxia during normoxia at rest (normREST), normoxia during visual stimulation (normSTIM), mild hypoxia at rest (hypREST) and mild hypoxia during visual stimulation (hypSTIM)

Fig. 6.4. shows the absolute metabolic concentrations and associated CRLB obtained from the LCMoel quantification of a typical representative spectra from normoxia. The metabolite spectra presented excellent signal to noise and spectral resolution in both gas condition, as shown by Fig 6.5.

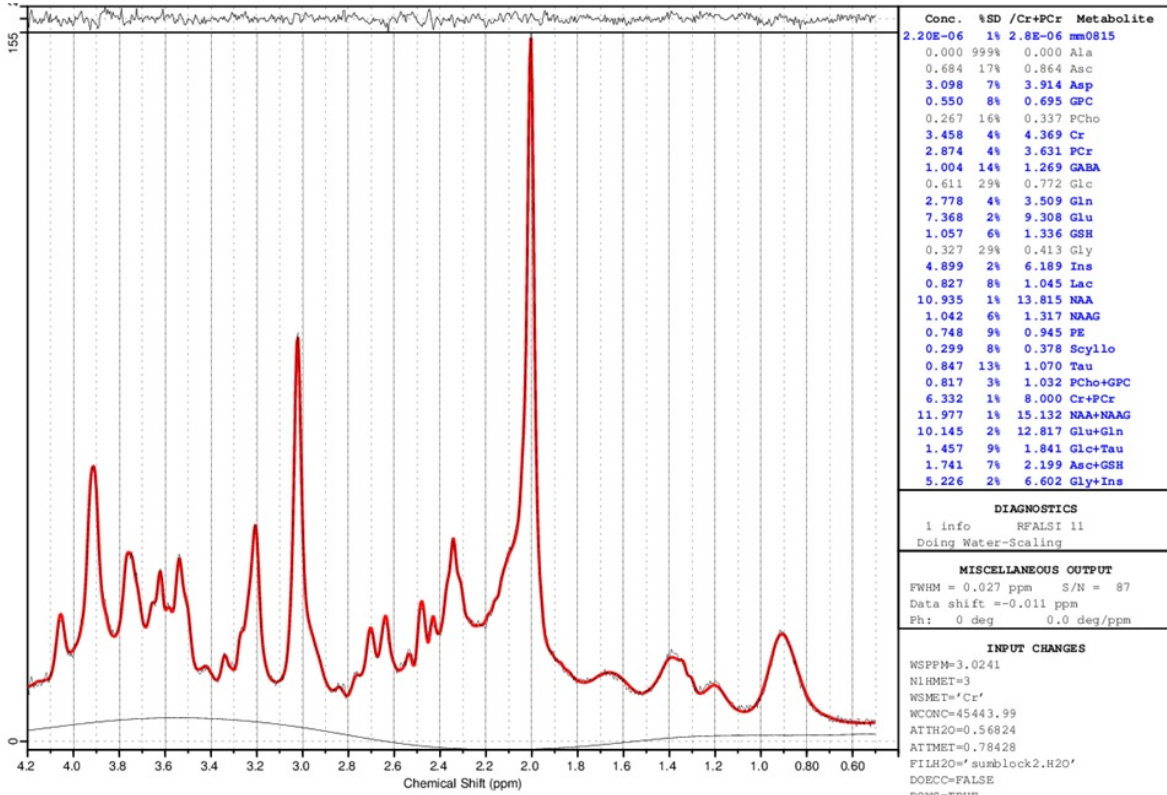


Fig. 6.4. LCMoDel quantification of a typical representative spectra from normoxia

Spectra quantification in the subject level revealed baseline concentrations of Asp and Gln reduced during hypoxia as compared to normoxia, as shown in Table 6.1.

Table 6.1. Absolute metabolic concentrations during baseline

	Aspartate (mM)	Glutamine (mM)	Glutamate (mM)
Normoxia	2.84±0.47	2.57±0.29	7.25±0.25
Hypoxia	2.54±0.45 *	2.38±0.26 *	7.35±0.24

*p<0.05, normoxia vs hypoxia, paired t-test. Mean ± SD.

Despite not exhibiting a significant trend at the subject level analysis (p=0.12), a negative residue at approximately 2.35 ppm was fitted as an inverted signal of Glu (Fig. 6.5), corroborated by the quantification of the group-level spectra, which showed a small negative difference (normREST-hypREST) of 0.15 mM between Glu at baselines. The findings at the subject level were confirmed by the LCMoDel quantification of the difference spectrum (normREST - hypREST). Based on visual inspection of the corrected difference spectrum, a linewidth broadening of 1.2 Hz was utilized to minimize linewidth differences between the two spectra, similarly to the BOLD line-narrowing effect correction previously described. However, it was not possible to entirely remove the large

resonances residue (n-acetylaspartate, creatine and choline) as it was performed during STIM-REST subtraction of normoxia or hypoxia, possibly due to a non-pure line shape caused by hypoxia.

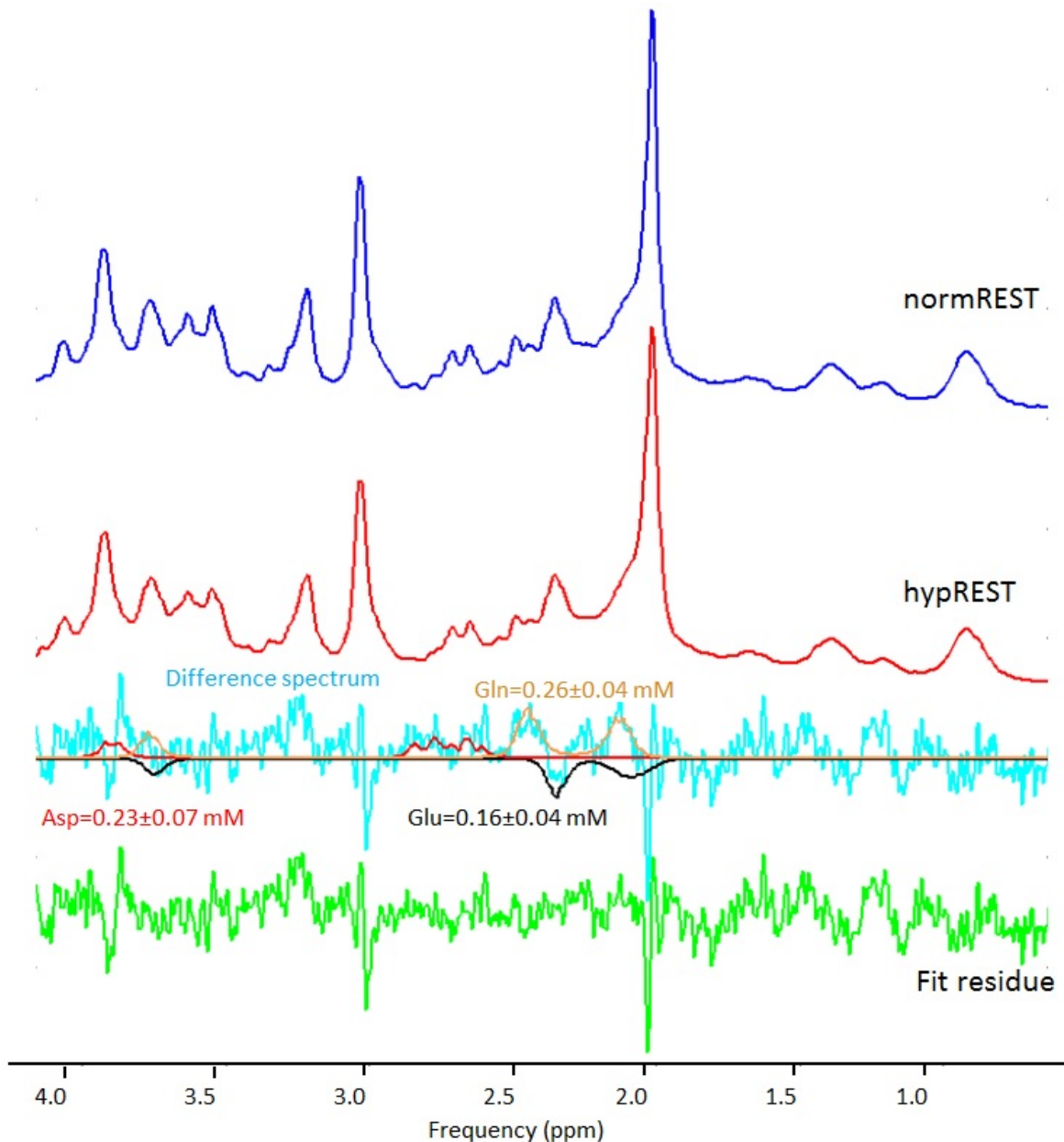


Fig. 6.5. Example of spectra acquired at normoxia during rest (normREST, in blue) and during mild hypoxia at rest (hypREST, in red) from a single subject. LCMoDel analysis of the difference spectrum ($N=10$, normREST – hypREST, in cyan), LCMoDel fit components: aspartate (Asp, red), glutamine (Gln, orange) and glutamate (Glu, black). Fit residue (green). Concentrations are given as mean \pm CRLB. Gaussian filter ($\sigma=0.15$ Hz) was applied on the difference spectrum and fit residue for display purposes.

Stimulus-induced metabolic changes measured in normoxia were in excellent agreement with previously reports from fMRS studies in the visual cortex using 7T scanners (151,153,154), with significant changes of Asp ($p=0.03$) (151,152,154), Glu ($p=0.001$) (151–154), Lac ($p=0.03$) (151–154), as shown in Table 6.2. Glucose has also been reported to decrease with stimulation (153,154), but the observed trend in our data was not statistically significant. During hypoxia, only stimulus-induced changes of Glu and Lac were significant ($p<0.001$ and $p=0.01$, respectively), being these the most common findings from fMRS studies in normoxia using 7T scanners (151–154).

Table 6.2. Absolute metabolic concentration differences (STIM-REST) due to stimulation

	Aspartate (mM)	Glutamate (mM)	Lactate (mM)	Glucose (mM)
Normoxia	-0.25 ± 0.23 *	0.29 ± 0.16 *	0.19 ± 0.23 *	-0.15 ± 0.33
Hypoxia	-0.12 ± 0.29	0.24 ± 0.10 *	0.16 ± 0.13 *	-0.09 ± 0.33

* $p<0.05$, STIM vs REST, paired t-test. Mean \pm SD. Glucose at normoxia exhibited a trend with $p=0.07$.

Average quantified concentrations over all subjects for both gas and stimulus conditions of significantly altered metabolites are summarized in Fig. 6.6. Other metabolites were not affected by oxygen reduction or visual stimulation. Stimulus-induced metabolic changes of Glu and Lac in normoxia were not significantly different from those induced during hypoxia.

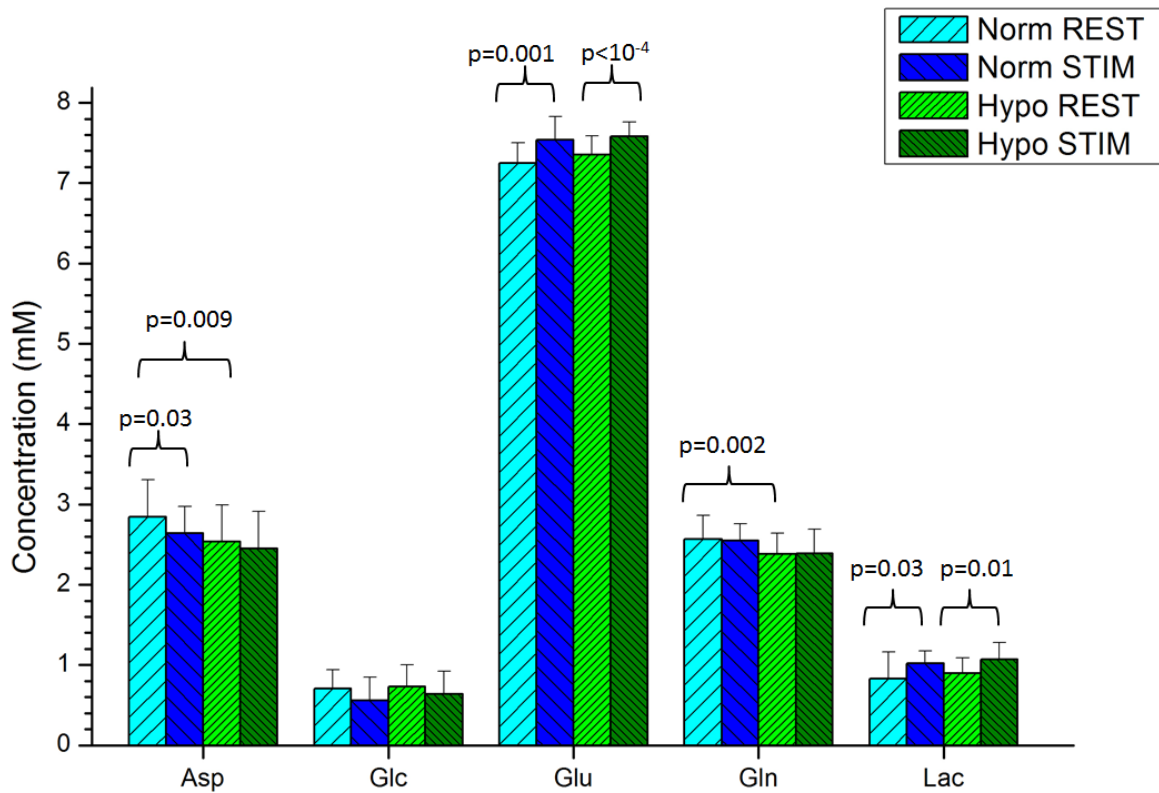


Fig. 6.6. Average metabolic concentrations during fMRS paradigm over subjects (N=11). P-values were calculated using paired two-tailed t-test. Error bars represent the standard deviation. Asp, aspartate; Glc, glucose; Glu, glutamate; Gln, glutamine; Lac, lactate. NormREST, mild hypoxia during normoxia at rest; NormSTIM, normoxia during visual stimulation; HypREST, mild hypoxia at rest; HypSTIM, mild hypoxia during visual stimulation.

The difference spectrum (STIM - REST) for both gas conditions confirmed findings observed at the subject level for both normoxia and hypoxia conditions, as shown by Fig. 6.7. A line broadening of 0.41 Hz in normSTIM was necessary to make the difference spectrum BOLD-free, whereas a 0.19 Hz line broadening was used at hypSTIM spectrum.

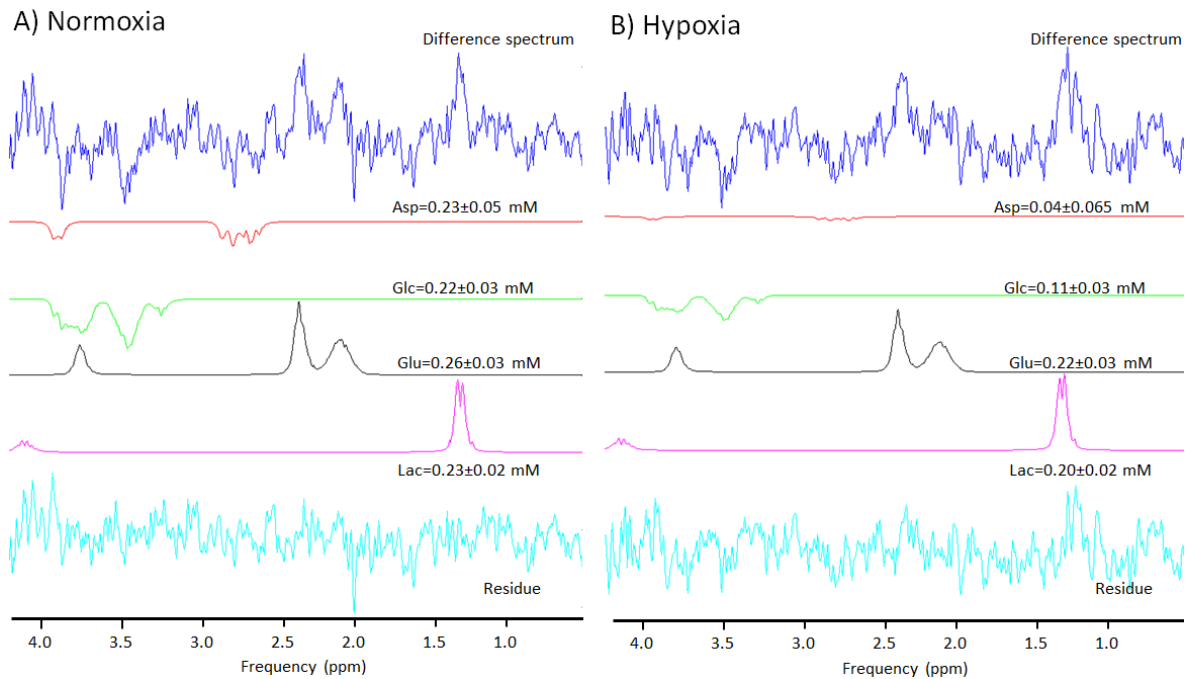


Fig. 6.7. LCMoDel analysis of the difference spectrum (STIM - REST) from normoxia (A) and mild hypoxia (B). From top to bottom: difference spectrum (blue) to be fitted in LCMoDel. LCMoDel fitted components: aspartate (red), glucose (green), glutamate (black), lactate (magenta) and the fit residue (cyan). Concentrations given as mean \pm CRLB. Gaussian filter ($\sigma=0.15$ Hz) was applied on the difference spectrum and the residue for display purposes.

6.3 Discussion

Oxygen and carbon dioxide play important roles in the energetic metabolism and regulation of the evoked vascular response, respectively. In this study we utilized a tight manipulation of O_2 levels to induce mild hypoxia without the bias of possible effects caused by CO_2 variation.

A lower partial pressure of oxygen in the gas mixture was utilized to reduce oxygen availability in the blood, hence increasing the deoxy/oxyhemoglobin ratio. Due to the strong paramagnetic properties of deoxyhemoglobin, a consistent linewidth increase of both water and metabolic peaks was observed in mild hypoxia as compared to normoxia, through shortening of T_2 that is reflected at the full width at half maximum of peaks. Even though linewidth differences in the range of 1 to 1.5 Hz might be comparable to the inter-subject variability range, it has been shown that metabolite quantifications can be differently affected by linewidth changes of up to 0.5 Hz (144). Therefore, the linewidth matching procedure performed in this study aimed at reducing bias of estimated absolute

concentrations from different linewidth spectra. Importantly, the stimulus and mild hypoxia induced differences in absolute concentration were very similar with or without linewidth matching.

The smaller BOLD effect on linewidth changes of water peaks during mild hypoxia is in excellent agreement with imaging results that showed reduced BOLD signal amplitude during mild hypoxia as compared to normoxia, possibly due to the lesser mismatch between oxygen delivery and extraction (6,176). These studies have also shown that the area displaying BOLD activation during mild hypoxia was smaller than the area activated in normoxia (6,170,171,176), which could also have contribute to a smaller linewidth change (i.e. less active tissue within the VOI).

Stimulus-induced metabolic changes in Asp, Glu and Lac measured in normoxia were in good agreement with recent reports of fMRS at 7T (151–154). Such findings were attributed to a new steady state of increased oxidative metabolism during sustained neuronal activation (151). During mild hypoxia, stimulus-induced significant changes were observed in only Glu and Lac, with similar amplitude as compared to normoxia. The STIM-REST difference spectrum (Fig. 6.7) shows reduced Asp and Glc components during mild hypoxia, but yet those are not significant findings at the subject level (hypREST vs hypSTIM), possibly due to the reduced amplitude change associated with inter-subject variability. No stimulus-induced metabolic changes in normoxia were significantly different from mild hypoxia. In front of these findings, we do not see strong evidence that suggests altered stimulus-induced metabolic changes during mild hypoxia as compared to normoxia, and hence it is likely that the oxidative metabolism increase capacity remains unaltered despite the reduced oxygen availability. Previous fMRI studies have reported reduced active areas during mild hypoxia as compared to normoxia (6,170–172), which could be interpreted as reduced neuronal recruitment. However, our spectroscopy data acquired during hypoxia indicate similar stimulus-induced Glu and Lac changes during hypoxia, which are known to be robust markers of increased oxidative metabolism and hence neuronal activation (154). Thus, we do not expect different neuronal recruitment during stimulation in mild hypoxia.

Despite unchanged stimulus-induced metabolic concentrations, changes in Asp, Glu and Gln were observed between baseline conditions (Fig 6.2), suggesting altered baseline

metabolism between normoxia and mild hypoxia. The concentration differences had a similar magnitude to those detected due to visual stimulation. Glutamine is the most abundant amino acid in blood and the second carbon source of energy production and anabolic processes. It plays an essential role as part of the Glu-Gln cycle, which prevents extracellular Glu reaching toxic levels, and also interconnects TCA cycles from both neurons and astrocytes. The link between TCA cycles is critical, since the amount of TCA intermediates is relatively low as compared to the carbon flux in the TCA cycle and the cytosolic pools of Glu, Gln and Asp (192). Thereby, the removal of TCA cycle intermediates (e.g. biosynthesis of biomolecules, net conversion of α -ketoglutarate to Glu) must be closely matched by the introduction of intermediates by other means. The link between TCA cycles through Glu-Gln cycle allows the loss of neuronal intermediates to be compensated by astrocytic metabolism. Therefore, the Gln concentration change observed in our study during mild hypoxia could be potentially related to the maintenance of neuronal TCA cycle intermediates, by adjusting concentrations to a new steady state. It is unlikely that the level of mild hypoxia utilized in this study was capable of triggering adaptive reactions observed in acute hypoxia, such as stimulation of hypoxia-inducible factors (193), especially when considering that stimulus-induced metabolic changes were preserved during mild hypoxia.

6.4 Conclusion

We conclude that mild hypoxia did not affect stimulus-induced glutamate and lactate metabolic responses commonly observed at 7T fMRS studies, which are robust markers of increased oxidative metabolism and hence neuronal activation. Therefore, we do not see evidence that supports altered neuronal recruitment during mild hypoxia. Analysis of the neurochemical profiles during rest periods revealed significant changes in aspartate, glutamate and glutamine during hypoxia. Further analysis will be necessary to elucidate the role played by these metabolic changes in the new steady state achieved during mild hypoxia.

CHAPTER 7 - CONCLUSIONS AND OUTLOOK

In this thesis we focused on evaluating the impact of reduced oxygen availability on the neurovascular and metabolic coupling of the healthy human brain. Multimodal fMRI combined with improved sensitivity of MRS at 7T were used on two different studies to characterize the vascular and metabolic responses, respectively. Obtaining new insights of the in vivo human brain about the role played by oxygen on the functional brain metabolism is crucial for understanding the basics aspects of cerebral energetics and its relationship with the neurovascular system. Mild hypoxic hypoxia was safely utilized in this study through the control of the inspired gas mixture, by a simple flow balance between O₂ and N₂ as in the fMRI study, or by a computer-controlled gas blender as in the fMRS study. Despite the relative low level of induced mild hypoxia (equivalent to approximately 4000 m altitude, which yielded in arterial blood oxygen saturation of 80%) for a period of time inferior to 30 minutes, changes in both vascular variables and baseline metabolic concentrations were observed. From our fMRI study, mild hypoxia produced substantial reductions in the common activated volumes detected by BOLD, ASL and VASO images. However, these areas showed unaltered CBF and CBV responses, but smaller BOLD signal. In addition, a trend for stimulus-induced ΔCMRO_2 reduction was observed in mild hypoxia. These findings potentially suggest smaller neuronal recruitment, but yet it remains unclear whether mild-hypoxia could result in a different neurovascular coupling. From the fMRS study, stimulus-induced metabolic changes of glutamate and lactate during mild hypoxia were not significantly different from normoxia, suggesting unaltered oxidative metabolism and hence neuronal recruitment. Finally, the combination of the data from the two studies herein presented suggests that mild hypoxia does not result in reduced neuronal recruitment to visual stimulation despite the altered vascular evoked response. Therefore, an heterogeneity in the neurovascular coupling is observed during mild hypoxia. Additionally, our spectroscopy data also reveals the existence of baseline metabolism changes between normoxia and mild hypoxia. Further analysis will be necessary to elucidate how the new steady state concentrations of aspartate, glutamate and glutamine could be linked to physiological mechanism that potentially alters the neurovascular response.

WORK AND PUBLICATIONS

Awards

- ISMRM Merit Award - Magna cum laude, International Society for Magnetic Resonance in Medicine, 2015.

Grants received

- Translational Technologies and Resources Core Usage Program, by the application of the proposal “Metabolic changes in the activated human visual cortex during mild hypoxia”.

Peer-reviewed journal articles

- **Barreto, F.**; Mangia, S.; Salmon, C. Effects of reduced oxygen availability on the vascular response and CMRO₂ of the activated human visual cortex. Manuscript in preparation.
- **Barreto, F.**; Bednařík, P.; Tkac, I.; Evanoff, N.; Dengel, D.; Deelchand, D.; Salmon, C.; Mangia, S. Metabolic changes in the activated human visual cortex during mild hypoxia. Manuscript in preparation.
- Bednařík, P.; Tkac, I.; Giove, F.; Eberly, L.; Deelchand, D.; **Barreto, F.**; Mangia, S. Neurochemical and BOLD Responses in Activated Blob and Interblob Neuronal Populations Measured in the Human Visual Cortex at 7T. Manuscript in preparation.
- Mangia, S.; Bednařík, P.; Deelchand, D.; **Barreto, F.**; Eberly, L.; Giove, F.; Michaeli, S.; Tkac, I. Functional MRS at 7 T and long TE. Manuscript in preparation.

Peer-reviewed abstract at international conferences

- **Barreto, F.**; Mangia, S.; Salmon, C. Temporal and spatial changes of BOLD signal, CBF and CBV in the activated human visual cortex during mild hypoxia. Proc. ISMRM 23rd Scientific Meeting, Canada, 2015. (ISMRM Merit Award)
- Bednařík, P. ; Tkac, I. ; Giove, F. ; Deelchand, D. ; Eberly, L. ; **Barreto, F.**; Mangia, S. Neurochemical and BOLD responses in activated blob and interblob neuronal populations measured in the human visual cortex at 7T. Proc. ISMRM 23rd Scientific Meeting, Canada, 2015.
- **Barreto, F.**; Evanoff, N.; Dengel, D.; Bednařík, P.; Tkac, I.; Eberly, L.; Salmon, C. Metabolic changes in the activated human visual cortex during mild hypoxia. Proc. ISMRM 24th Scientific Meeting, Singapore, 2016.

- **Barreto, F.**; Li, X.; Moheet, A.; Kumar, A.; Eberly, L.; Seaquist, E.; Esposito, F.; Mangia, S. Accuracy and inter-subject reproducibility of default mode networks identified from ASL data. Proc. ISMRM 24th Scientific Meeting, Singapore, 2016.
- Bednařik, P. ; Tkac, I. ; Deelchand, D. ; **Barreto, F.**; Eberly, L. ; Shalom, M.; Mangia, S. Functional MRS at 7T and long TE. Proc. ISMRM 24th Scientific Meeting, Singapore, 2016.

REFERENCES

1. Siesjo BK. Brain energy metabolism. In New York: Wiley; 1978. p. 101–30.
2. Lennie P. The cost of cortical computation. *Curr Biol*. 2003;13:493–7.
3. Iadecola C. Neurovascular regulation in the normal brain and in Alzheimer’s disease. *Nat Rev Neurosci*. 2004;5:347–60.
4. Muoio V, Persson PB, Sendeski MM. The neurovascular unit - concept review. *Acta Physiol*. 2014;210(4):790–8.
5. Eccles J. Some aspects of Sherrington’s contribution to neurophysiology. *R Soc J Hist Sci*. 1957;2:216–25.
6. Ho Y-CL, Vidyasagar R, Shen Y, Balanos GM, Golay X, Kauppinen RA. The BOLD response and vascular reactivity during visual stimulation in the presence of hypoxic hypoxia. *Neuroimage*. 2008 Jun;41(2):179–88.
7. Chugani H, Phelps M, Mazziotta J. Positron emission tomography study of human brain functional development. *Ann Neurol*. 1987;1:487–97.
8. Gruetter R, Ugurbil K, Seaquist E. Steady-state cerebral glucose concentrations and transport in the human brain. *J Neurochem*. 1998;70:397–408.
9. Buxton RB. Interpreting oxygenation-based neuroimaging signals: the importance and the challenge of understanding brain oxygen metabolism. *Front Neuroenergetics*. 2010;2:1–16.
10. Ito H, Ito K, Kato C, Sasaki T, Ouchi Y, Iida A, et al. Database of normal human cerebral blood flow, cerebral blood volume, cerebral oxygen extraction fraction and cerebral metabolic rate of oxygen measured by positron emission tomography with ¹⁵O-labelled carbon dioxide or water, carbon monoxide and oxygen. *Eur J Nucl Med Mol Imaging*. 2004;31:635–43.
11. Mintun MA, Lundstrom BN, Snyder AZ, Vlassenko AG, Shulman GL, Raichle ME. Blood flow and oxygen delivery to human brain during functional activity: theoretical modeling and experimental data. *Proc Natl Acad Sci U S A*. 2001 Jun 5;98(12):6859–64.
12. Chen WEI, Novotny EJ, Zhu X, Rothman DL, Shulman RG. Localized ¹H NMR measurement of glucose consumption in the human brain during visual stimulation. *Magn Reson Med*. 1993;30:989–900.
13. Davis TL, Kwong KK, Weisskoff RM, Rosen BR. Calibrated functional MRI: mapping the dynamics of oxidative metabolism. *Proc Natl Acad Sci U S A*. 1998 Feb 17;95(4):1834–9.
14. Kim SG, Ugurbil K. Comparison of blood oxygenation and cerebral blood flow

effects in fMRI: estimation of relative oxygen consumption change. *Magn Reson Med.* 1997;38:59–65.

15. Leithner C, Royl G, Offenhauser N, Füchtmeier M, Kohl-Bareis M, Villringer A, et al. Pharmacological uncoupling of activation induced increases in CBF and CMRO₂. *J Cereb blood flow Metab.* 2010;30:311–22.
16. Lin A-L, Fox PT, Hardies J, Duong TQ, Gao J-H. Nonlinear coupling between cerebral blood flow, oxygen consumption, and ATP production in human visual cortex. *Proc Natl Acad Sci U S A.* 2010 May 4;107(18):8446–51.
17. Madsen PL, Hasselbalch SG, Hagemann LP, Olsen KS, Bülow J, Holm S, et al. Persistent resetting of the cerebral oxygen/glucose uptake ratio by brain activation: evidence obtained with the Kety-Schmidt technique. *J Cereb blood flow Metab.* 1995;15:485–91.
18. Wey H-Y, Wang DJ, Duong TQ. Baseline CBF, and BOLD, CBF, and CMRO₂ fMRI of visual and vibrotactile stimulations in baboons. *J Cereb blood flow Metab.* 2011;31:715–24.
19. Zhu X-H, Zhang N, Zhang Y, Uğurbil K, Chen W. New insights into central roles of cerebral oxygen metabolism in the resting and stimulus-evoked brain. *J Cereb blood flow Metab.* 2009 Jan;29(1):10–8.
20. Uludağ K, Dubowitz DJ, Yoder EJ, Restom K, Liu TT, Buxton RB. Coupling of cerebral blood flow and oxygen consumption during physiological activation and deactivation measured with fMRI. *Neuroimage.* 2004 Sep;23(1):148–55.
21. Chen JJ, Pike GB. BOLD-specific cerebral blood volume and blood flow changes during neuronal activation in humans. *NMR Biomed.* 2009 Dec;22(10):1054–62.
22. Liang CL, Ances BM, Perthen JE, Moradi F, Liao J, Buracas GT, et al. Luminance contrast of a visual stimulus modulates the BOLD response more than the cerebral blood flow response in the human brain. *Neuroimage.* 2013;64:104–11.
23. Attwell D, Iadecola C. The neural basis of functional brain imaging signals. *Trends Neurosci.* 2002;25:621–5.
24. Gnaiger E, Lassnig B, Kuznetsov A, Rieger G, Margreiter R. Mitochondrial oxygen affinity, respiratory flux control and excess capacity of cytochrome c oxidase. *J Exp Biol.* 1998;201:1129–39.
25. Moradi F, Buračas GT, Buxton RB. Attention strongly increases oxygen metabolic response to stimulus in primary visual cortex. *Neuroimage.* 2012;59(1):601–7.
26. Moradi F, Buxton RB. Adaptation of cerebral oxygen metabolism and blood flow and modulation of neurovascular coupling with prolonged stimulation in human visual cortex. *Neuroimage.* 2013;82:182–9.
27. Perthen JE, Lansing AE, Liao J, Liu TT, Buxton RB. Caffeine-induced uncoupling

- of cerebral blood flow and oxygen metabolism: A calibrated BOLD fMRI study. *Neuroimage*. 2008;40:237–47.
28. Griffeth VEM, Perthen JE, Buxton RB. Prospects for quantitative fMRI: investigating the effects of caffeine on baseline oxygen metabolism and the response to a visual stimulus in humans. *Neuroimage*. 2011 Aug 1;57(3):809–16.
 29. Blockley NP, Griffeth VEM, Simon AB, Buxton RB. A review of calibrated blood oxygenation level-dependent (BOLD) methods for the measurement of task-induced changes in brain oxygen metabolism. *NMR Biomed*. 2013 Aug;26(8):987–1003.
 30. Aanerud J, Borghammer P, Chakravarty MM, Vang K, Rodell AB, Jónsdóttir KY, et al. Brain energy metabolism and blood flow differences in healthy aging. *J Cereb blood flow Metab*. 2012 Jul;32(7):1177–87.
 31. Mangia S, Tkáč I, Uğurbil K. Investigation of the activated human primary visual cortex (V1) by functional MRS. In: Portocello TA, Velloti RB, editors. *Visual cortex: new research*. Hauppauge, NY: Nova Science Publisher; 2008. p. 251–68.
 32. Preibisch C, Sorg C, Förchler A, Grimmer T, Sax I, Wohlschläger AM, et al. Age-related cerebral perfusion changes in the parietal and temporal lobes measured by pulsed arterial spin labeling. *J Magn Reson imaging*. 2011 Dec;34:1295–302.
 33. Hodgkin A, Huxley A. A quantitative description of membrane current and its application to conductance and excitation. *J Physiol*. 1952;117:500–44.
 34. Baker P, Connelly C. Some properties of the external activation site of the sodium pump in crab nerve. *J Physiol*. 1966;185:270–97.
 35. Hertz L, Schousboe A. Ion and energy metabolism of the brain at the cellular level. *Int Rev Neurobiol*. 1975;18:141–211.
 36. Mata M, Fink D, Gainer H, Smith C, Davidsen L, Savaki H, et al. Activity-dependent energy metabolism in rat posterior pituitary primarily reflects sodium pump activity. *J Neurochem*. 1980;34:213–5.
 37. Sokoloff L, Reivich M, Kennedy C, DesRosiers M, Patlak C, Pettigrew K, et al. The [¹⁴C]deoxyglucose method for the measurement of local cerebral glucose utilization: Theory, procedure, and normal values in the conscious and anesthetized albino rat. *J Neurochem*. 1977;28:897–916.
 38. Levy D, Sidtis J, Rottenberg D, Jarden J, Strother S, Dhawan V, et al. Differences in cerebral blood flow and glucose utilization in vegetative versus locked-in patients. *Ann Neurol*. 1987;22:673–82.
 39. Sibson NR, Mason GF, Shulman RG. Functional Energy Metabolism : In vivo ¹³C-NMR Spectroscopy Evidence for Coupling of Cerebral. 1998;20:321–30.
 40. Duarte J, Gruetter R. Glutamatergic and GABAergic energy metabolism measured in the rat brain by ¹³C NMR spectroscopy at 14.1 T. *J Neurochem*. 2013;126:579–90.

41. Arriza JL, Fairman WA, Wadiche JI, Murdoch GH, Kavanaugh P, Amara SG. Functional Comparisons of Three Glutamate Cloned from Human Motor Cortex Transporter. *J Neurosci.* 1994;14:5559–69.
42. Zwingmann C, Leibfritz D. Regulation of glial metabolism studied by ¹³C-NMR. *NMR Biomed.* 2003;16:370–99.
43. Blomqvist G, Seitz RJ, Sjogren I, Halldin C, Stone-Elander S, Widen L, et al. Regional cerebral oxidative and total glucose consumption during rest and activation studied with positron emission tomography. *Acta Physiol Scand.* 1994;151:29–43.
44. Barinaga M. Neuroscience: what makes brain neurons run. *Science* (80-). 1997;11:196–8.
45. Mathews P, Bland J, Gadian D, Radda G. The steady-state rate of ATP synthesis in the perfused rat heart measured by ³¹P NMR saturation transfer. *Biochem Biophys Res Commun.* 1981;103:1052–9.
46. Balaban R, Kantor H, Katz L, Briggs R. Relation between work and phosphate metabolites in he in vivo paced mamalian heart. *Science* (80-). 1986;232:1121–3.
47. Detre J, Koretsky A, Williams D, Ho C. Absence of pH changes during altered work in the in vivo sheep heart: a ³¹P-NMR investigation. *J Mol Cell Cardiol.* 1990;22:543–53.
48. Wyss M, Smeitink J, Wevers R, Wallimann T. Mitochondrial creatine kinase: a key enzyme of aerobic energy metabolism. *Biochim Biophys Acta.* 1992 Sep 25;1102:119–66.
49. Roth K, Weiner M. Determination of cytosolic ADP and AMP concentrations and the free energy of ATP hydrolysis in human muscle and brain tissues with ³¹P NMR. *Magn Reson Med.* 1991;22:505–11.
50. Mora B, Narasimhan P, Ross B. ³¹P magnetization transfer studies in the monkey brain. *Magn Reson Med.* 1992;26:100–15.
51. Fedosov S. Creatine-creatine phosphate shuttle modeled as two-compartment system at different levels of creatin kinase activity. *Biochim Biophys Acta.* 1994;1208:237–46.
52. Sappey-Marinier D, Calabrese G, Fein G, Hugg J, Biggins C, Weiner M. Effect of Photic Stimulation on Human Visual Cortex Lactate and Phosphates Using ¹H and ³¹P Magnetic Resonance Spectroscopy. 1992;(1991):584–92.
53. Kato T, Murashita J, Shioiri T, Hamakawa H, Inubushi T. Effect of photic stimulation on energy metabolism in the human brain measured by ³¹P-MR spectroscopy. *J Neuropsychiatry Clin Neurosci.* 1996;8:417–22.
54. Murashita J, Kato T, Shioiri T, Inubushi T, Kato N. Age-dependent alteration of metabolic response to photic stimulation in the human brain measured by ³¹P MR-

- spectroscopy. *Brain Res.* 1999 Feb 6;818:72–6.
55. Rango M, Bozzali M, Prella A, Scarlato G, Bresolin N. Brain activation in normal subjects and in patients affected by mitochondrial disease without clinical central nervous system involvement: a phosphorus magnetic resonance spectroscopy study. *J Cereb blood flow Metab.* 2001 Jan;21:85–91.
 56. Chen W, Zhu X, Adriany G, Ugurbil K. Increase of creatine kinase activity in the visual cortex of human brain during visual stimulation: a ³¹P magnetization transfer study. *Magn Reson Med.* 1997 Oct;38(4):551–7.
 57. Gjedde A. Modulation of substrate transport to the brain. *Acta Neurol Scand.* 1983;67:3–25.
 58. Desagher S, Glowinski J, Premont J. Pyruvate protects neurones against hydrogen peroxide-induced toxicity. *Neuroscience.* 1997;17:9060–7.
 59. Silver I, Erecińska M. Extracellular glucose concentration in mammalian brain: Continuous monitoring of changes during increased neuronal activity and upon limitation in oxygen supply in normo-, hypo-, and hyperglycemic animals. *J Neurosci.* 1994;14:5068–76.
 60. Gibbs E, Lennox W, Nims L, Gibbs F. Arterial and cerebral venous blood; arterial-venous differences in man. *J Biol Chem.* 1942;144:325–32.
 61. Himwich H, Fazekas J. Effect of hypoglycemia on metabolism of brain. *Endocrinology.* 1937;21:800–7.
 62. Himwich W, Himwich H. Pyruvic acid exchange of brain. *J Neurophysiol.* 1946;9:133–6.
 63. Rich PR. The molecular machinery of Keilin's respiratory chain. *Biochem Soc Trans.* 2003;31:1095–105.
 64. Magistretti PJ, Pellerin L. Cellular mechanisms of brain energy metabolism and their relevance to functional brain imaging. *Philos Trans R Soc Lond B Biol Sci.* 1999;354(1387):1155–63.
 65. Nehlig A, Wittendorp-Rechenmann E, Lam C. Selective uptake of [¹⁴C]2-deoxyglucose by neurons and astrocytes: high-resolution microautoradiographic imaging by cellular ¹⁴C-trajectory combined with immunohistochemistry. *J Cereb Blood Flow Metab.* 2004;24(9):1004–14.
 66. Gruetter R. Glycogen, the forgotten cerebral energy store. *J Neurosci Res.* 2003;74(2):179–83.
 67. Shetty PK, Galeffi F, Turner DA. Cellular links between neuronal activity and energy homeostasis. *Front Pharmacol.* 2012;3:1–14.
 68. Schuchmann S, Kovacs R, Kann O, Heinemann U, Buchheim K. Monitoring

- NAD(P)H autofluorescence to assess mitochondrial metabolic functions in rat hippocampal-entorhinal cortex slices. *Brain Res Protoc.* 2001;7:267–76.
69. Hu Y, Wilson G. Rapid changes in local extracellular rat brain glucose observed with an in vivo glucose sensor. *J Neurochem.* 1997;68:1745–52.
 70. Foster K, Beaver C, Turner D. Interaction between tissue oxygen tension and NADH imaging during synaptic stimulation and hypoxia in rat hippocampal slices. *Neuroscience.* 2005;132:645–57.
 71. Denton R. Regulation of mitochondrial dehydrogenases by calcium ions. *Biochim Biophys Acta.* 2009;1787:1309–16.
 72. Chan P. Role of oxidants in ischemic brain damage. *Stroke.* 1996;27:1124–9.
 73. Gilany K, Vafakhah M. Hypoxia : a Review. *J Paramed Sci.* 2010;1:43–60.
 74. Wenger R. Mammalian oxygen sensing, signaling and gene regulation. *J Exp Biol.* 2000;203:1253–63.
 75. Lopez-Barneo J, Pardal R, Ortega-Saenz P. Cellular Mechanism of Oxygen Sensing. *Annu Rev Physiol.* 2001;63:259–87.
 76. Kemp P, Peers C. Oxygen sensing by ion channels. *Essays Biochem.* 2007;43:77–90.
 77. Yuan X, Tod M, Rubin L, Blaustein M. Contrasting effects of hypoxia on tension in rat pulmonary and mesenteric arteries. *Am J Physiol Hear Circ Phisiology.* 1990;259(2):H281–9.
 78. Peers C, Kemp PJ. Acute oxygen sensing: diverse but convergent mechanisms in airway and arterial chemoreceptors. *Respir Res.* 2001;2(3):145–9.
 79. Boutilier RG. Mechanisms of cell survival in hypoxia and hypothermia. *J Exp Biol.* 2001;204:3171–81.
 80. Moeller S, Yacoub E, Olman C a, Auerbach E, Strupp J, Harel N, et al. Multiband multislice GE-EPI at 7 tesla, with 16-fold acceleration using partial parallel imaging with application to high spatial and temporal whole-brain fMRI. *Magn Reson Med.* 2010 May;63:1144–53.
 81. Bloch F. Nuclear induction. *Phys Rev.* 1946;70:460–73.
 82. Nitz WR, Reimer P. Contrast mechanisms in MR imaging. *Eur Radiol.* 1999;9:1032–46.
 83. Schaefer PW, Grant PE, Gonzalez RG. Diffusion-weighted MR Imaging of the Brain. *Radialogy.* 2000;217:331–45.
 84. Gasparotti R, Pinelli L, Liserre R. New MR sequences in daily practice: susceptibility weighted imaging. A pictorial essay. *Insights Imaging.* 2011;2:335–47.

85. Stehling M, Turner R, Mansfield P. Echo planar imaging: magnetic resonance imaging in a fraction of a second. *Science* (80-). 1991;254:43–50.
86. Jezzard P, Balaban R. Correction for geometric distortion in echo planar images from B0 field variations. *Magn Reson Med*. 1995;34:65–73.
87. Buxton RB, Griffeth VEM, Simon AB, Moradi F. Variability of the coupling of blood flow and oxygen metabolism responses in the brain: A problem for interpreting BOLD studies but potentially a new window on the underlying neural activity. *Front Neurosci*. 2014;8:1–6.
88. Kwong KK, Belliveau JW, Chesler DA, Goldberg IE, Weisskoff RM, Poncelet BP, et al. Dynamic magnetic resonance imaging of human brain activity during primary sensory stimulation. *Proc Natl Acad Sci U S A*. 1992 Jun 15;89(12):5675–9.
89. Ogawa S, Lee TM, Kay AR, Tank DW. Brain magnetic resonance imaging with contrast dependent on blood oxygenation. *Proc Natl Acad Sci U S A*. 1990 Dec;87(24):9868–72.
90. Menon R, Ogawa S, Tank D, Ugurbil K. 4 Tesla gradient recalled echo characteristics of photic stimulation-induced signal changes in the human primary visual cortex. *Magn Reson Med*. 1993;30:380–6.
91. Malonek D, Grinvald A. Interactions between electrical activity and cortical microcirculation revealed by imaging spectroscopy: implications for functional brain mapping. *Science* (80-). 1996;272:551–4.
92. Buxton RB, Wong EC, Frank LR. Dynamics of blood flow and oxygenation changes during brain activation: the balloon model. *Magn Reson Med*. 1998;39(17):855–64.
93. Frahm J, Krüger G, Merboldt K, Kleinschmidt A. Dynamic uncoupling and recoupling of perfusion and oxidative metabolism during focal brain activation in man. *Magn Reson Med*. 1996;35:143–8.
94. Clare S, Francis S, Morris P, Bowtell R. Single-shot T2* measurement to establish optimum echo time for fMRI: Studies of the visual, motor, and auditory cortices at 3T. *Magn Reson Med*. 2001;45(5):930–3.
95. Fera F, Yongbi MN, Van Gelderen P, Frank JA, Mattay VS, Duyn JH. EPI-BOLD fMRI of Human Motor Cortex at 1.5 T and 3.0 T: Sensitivity Dependence on Echo Time and Acquisition Bandwidth. *J Magn Reson Imaging*. 2004;19(1):19–26.
96. Lancaster JL, Woldorff MG, Parsons LM, Liotti M, Freitas CS, Rainey L, et al. Automated Talairach Atlas labels for functional brain mapping. *Hum Brain Mapp*. 2000;10(3):120–31.
97. Mazziotta JC, Toga AW, Evans A, Fox P, Lancaster J. A probabilistic atlas of the human brain: theory and rationale for its development. The International Consortium for Brain Mapping (ICBM). Vol. 2, *NeuroImage*. 1995. p. 89–101.

98. Friston K, Holmes A, Worsley K, Poline J, Frith C, Frackowiak R. Statistical Parametric Maps in Functional Imaging : A General Linear Approach. *Hum Brain Mapp.* 1995;2:189–210.
99. Lindquist MA, Meng Loh J, Atlas LY, Wager TD. Modeling the hemodynamic response function in fMRI: efficiency, bias and mis-modeling. *Neuroimage.* 2009;45:1–25.
100. Worsley K, Liao C, Aston J, Petre V, Duncan G, Morales F, et al. A general statistical analysis for fMRI data. *Neuroimage.* 2002;15:1–15.
101. Lu H, Golay X, Pekar JJ, Van Zijl PCM. Functional magnetic resonance imaging based on changes in vascular space occupancy. *Magn Reson Med.* 2003 Aug;50(2):263–74.
102. Lu H, van Zijl PCM. A review of the development of Vascular-Space-Occupancy (VASO) fMRI. *Neuroimage.* 2012;62(2):736–42.
103. Lu H, Golay X, van Zijl P. Inter-voxel heterogeneity of event-related fMRI responses as function of T1-weighting. *Neuroimage.* 2002;17:943–55.
104. Lu H, Golay X, Pekar JJ, Van Zijl PCM. Sustained poststimulus elevation in cerebral oxygen utilization after vascular recovery. *J Cereb blood flow Metab.* 2004 Jul;24(7):764–70.
105. Wu WC, Fernández-Seara M, Detre JA, Wehrli FW, Wang J. A theoretical and experimental investigation of the tagging efficiency of pseudocontinuous arterial spin labeling. *Magn Reson Med.* 2007;58:1020–7.
106. Poser B a, Norris DG. Application of whole-brain CBV-weighted fMRI to a cognitive stimulation paradigm: robust activation detection in a stroop task experiment using 3D GRASE VASO. *Hum Brain Mapp.* 2011 Jun;32(6):974–81.
107. Calamante F, Thomas DL, Pell GS, Wiersma J, Turner R. Measuring cerebral blood flow using magnetic resonance imaging techniques. *J Cereb blood flow Metab.* 1999 Jul;19(7):701–35.
108. Chen Y, Wang Z, Detre J. Impact of equilibrium magnetization of blood on ASL quantification. In: *Proceedings of 19th Scientific Meeting and Exhibition of the International Society for Magnetic Resonance in Medicine.* 2011. p. 300.
109. Edelman R, Siewert B, Darby D, Thangaraj B, Nobre A, Mesulam M, et al. Qualitative mapping of cerebral blood flow and functional localization with echo planar MR imaging and signal targeting with alternating radio frequency. *Radiology.* 1994;192:513–20.
110. Wong E, Buxton R, Frank L. Implementation of quantitative perfusion imaging techniques for functional brain mapping using pulsed arterial spin labeling. *NMR Biomed.* 1997;10:237–49.

111. Detre J, Leigh J, Williams D, Koretsky A. Perfusion Imaging. *Magnetic Reson Med.* 1992;23:37–45.
112. Williams DS, Detre J a, Leigh JS, Koretsky a P. Magnetic resonance imaging of perfusion using spin inversion of arterial water. *Proc Natl Acad Sci U S A.* 1992 Jan 1;89(1):212–6.
113. Wolff S, Balaban R. Magnetization transfer contrast (MTC) and tissue water proton relaxation in vivo. *Magn Reson Med.* 1989;10:135–44.
114. Zhang W, Silva A, Williams D, Koretsky A. NMR measurement of perfusion using arterial spin labelling without saturation of macromolecules. *Magn Reson Med.* 1995;33:370–6.
115. Alsop D, Detre J. Multisection cerebral blood flow MR imaging with continuous arterial spin labeling. *Radiology.* 1998;208:410–6.
116. Dai W, Garcia D, de Bazelaire C, Alsop DC. Continuous flow-driven inversion for arterial spin labeling using pulsed radio frequency and gradient fields. *Magn Reson Med.* 2008 Dec;60:1488–97.
117. Calamante F, Williams S, van Bruggen N, Kwongs K, Turner R. A Model for Quantification of Perfusion in Pulsed Labelling Techniques. *NMR Biomed.* 1996;8:79–83.
118. Mintun M, Raichle M, Martin W, Herscovitch W. Brain oxygen utilization measured with ¹⁵O radiotracers and positron emission tomography. *J Nucl Med.* 1984;25:177–87.
119. Zhu X-H, Chen W. In vivo oxygen-17 NMR for imaging brain oxygen metabolism at high field. *Prog Nucl Magn Reson Spectrosc.* 2011 Nov;59(4):319–35.
120. Zhu X-H, Qiao H, Du F, Xiong Q, Liu X, Zhang X, et al. Quantitative imaging of energy expenditure in human brain. *Neuroimage.* Elsevier Inc.; 2012 May 1;60:2107–17.
121. Griffeth VEM, Buxton RB. A theoretical framework for estimating cerebral oxygen metabolism changes using the calibrated-BOLD method: modeling the effects of blood volume distribution, hematocrit, oxygen extraction fraction, and tissue signal properties on the BOLD signal. *Neuroimage.* 2011;58(1):198–212.
122. Boxerman JL, Hamberg LM, Rosen BR, Weisskoff RM. Mr contrast due to intravascular magnetic susceptibility perturbations. *Magn Reson Med.* 1995 Oct;34(4):555–66.
123. Grubb RL, Raichle ME, Eichling JO, Ter-Pogossian MM. The Effects of Changes in PaCO₂ Cerebral Blood Volume, Blood Flow, and Vascular Mean Transit Time. *Stroke.* 1974 Sep 1;5(5):630–9.
124. Horvath I, Sandor NT, Ruttner Z, McLaughlin a C. Role of nitric oxide in regulating

- cerebrocortical oxygen consumption and blood flow during hypercapnia. *J Cereb blood flow Metab.* 1994;14:503–9.
125. Yang SP, Krasney J a. Cerebral blood flow and metabolic responses to sustained hypercapnia in awake sheep. *J Cereb blood flow Metab.* 1995;15:115–23.
 126. Zappe a. C, Uludağ K, Oeltermann A, Uğurbil K, Logothetis NK. The influence of moderate hypercapnia on neural activity in the anesthetized nonhuman primate. *Cereb Cortex.* 2008;18(11):2666–73.
 127. Chen J, Pike B. MRI measurement of the BOLD-specific flow-volume relationship during hypercapnia and hypocapnia in humans. *Neuroimage.* 2010 Nov 1;53(2):383–91.
 128. Xu F, Uh J, Brier MR, Hart J, Yezhuvath US, Gu H, et al. The influence of carbon dioxide on brain activity and metabolism in conscious humans. *J Cereb blood flow Metab.* 2011;31:58–67.
 129. Kim T, Kim S-G. Temporal dynamics and spatial specificity of arterial and venous blood volume changes during visual stimulation: implication for BOLD quantification. *J Cereb blood flow Metab.* 2011;31(5):1211–22.
 130. Buxton RB, Uludağ K, Dubowitz DJ, Liu TT. Modeling the hemodynamic response to brain activation. *Neuroimage.* 2004;23:220–33.
 131. Leontiev O, Buracas GT, Liang C, Ances BM, Perthen JE, Shmuel A, et al. Coupling of cerebral blood flow and oxygen metabolism is conserved for chromatic and luminance stimuli in human visual cortex. *Neuroimage.* 2013;68:221–8.
 132. Obata T, Liu TT, Miller KL, Luh WM, Wong EC, Frank LR, et al. Discrepancies between BOLD and flow dynamics in primary and supplementary motor areas: Application of the balloon model to the interpretation of BOLD transients. *Neuroimage.* 2004;21:144–53.
 133. Leenders K, Perani D, Lammertsma A, Heather J, Buckingham P, Healy M, et al. Cerebral blood flow, blood volume and oxygen utilization. Normal values and effect of age. *Brain.* 1990;113:27–47.
 134. Zhao JM, Clingman CS, Närväinen MJ, Kauppinen R a, van Zijl PCM. Oxygenation and hematocrit dependence of transverse relaxation rates of blood at 3T. *Magn Reson Med.* 2007 Sep;58(3):592–7.
 135. Yablonskiy D, Haacke M. Theory of NMR signal behaviour in magnetically inhomogeneous tissues: the static dephasing regime. *Magn Reson Med.* 1994;32:749–63.
 136. Golay X, Silvennoinen MJ, Zhou J, Clingman CS, Kauppinen R a, Pekar JJ, et al. Measurement of tissue oxygen extraction ratios from venous blood T2: increased precision and validation of principle. *Magn Reson Med.* 2001 Aug;46(2):282–91.

137. Chanarin I. Blood and its diseases. 3rd editio. Edinburgh: Churchill Livingstone; 1984. 333 p.
138. Hua J, Donahue MJ, Zhao JM, Grgac K, Huang AJ, Zhou J, et al. Magnetization transfer enhanced vascular-space-occupancy (MT-VASO) functional MRI. *Magn Reson Med*. 2009 Apr;61(4):944–51.
139. van Zijl P, Eleff S, Ulatowski J, Oja J, Uluğ A, Traystman R, et al. Quantitative assessment of blood flow, blood volume and blood oxygenation effects in functional magnetic resonance imaging. *Nat Med*. 1998;4:159–67.
140. Ramsey N, Purcell E. Interactions between nuclear spins in molecules. *Phys Rev Lett*. 1952;85:143–4.
141. Tkáč I, Starcuk Z, Choi IY, Gruetter R. In vivo ¹H NMR spectroscopy of rat brain at 1 ms echo time. *Magn Reson Med*. 1999 Apr;41(4):649–56.
142. Tkac I, Rao R, Georgieff M, Gruetter R. Developmental and regional changes in the neurochemical profile of the rat brain determined by in vivo ¹H NMR spectroscopy. *Magn Reson Med*. 2003;50:24–32.
143. Sauter R, Mueller S, Weber H. Localization in in vivo ³¹P NMR spectroscopy by combining surface coils and slice-selective saturation. *J Magn Reson*. 1987;75:167–73.
144. Mangia S, Tkáč I, Gruetter R, Van De Moortele P-F, Giove F, Maraviglia B, et al. Sensitivity of single-voxel ¹H-MRS in investigating the metabolism of the activated human visual cortex at 7 T. *Magn Reson Imaging*. 2006 May;24(4):343–8.
145. Tkáč I, Oz G, Adriany G, Uğurbil K, Gruetter R. In vivo ¹H NMR spectroscopy of the human brain at high magnetic fields: metabolite quantification at 4T vs. 7T. *Magn Reson Med*. 2009 Oct;62(4):868–79.
146. Scheenen TWJ, Klomp DWJ, Wijnen JP, Heerschap A. Short echo time ¹H-MRSI of the human brain at 3T with minimal chemical shift displacement errors using adiabatic refocusing pulses. *Magn Reson Med*. 2008 Jan;59(1):1–6.
147. Garwood M, DelaBarre L. The return of the frequency sweep: designing adiabatic pulses for contemporary NMR. *J Magn Reson*. 2001 Dec;153(2):155–77.
148. Tannus A, Garwood M. Adiabatic pulses. *NMR Biomed*. 1997;10:423–34.
149. Oz G, Tkáč I. Short-echo, single-shot, full-intensity proton magnetic resonance spectroscopy for neurochemical profiling at 4 T: validation in the cerebellum and brainstem. *Magn Reson Med*. 2011 Apr;65(4):901–10.
150. Michaeli S, Garwood M, Zhu XH, Delabarre L, Andersen P, Adriany G, et al. Proton T₂ relaxation study of water, N-acetylaspartate, and creatine in human brain using Hahn and Carr-Purcell spin echoes at 4T and 7T. *Magn Reson Med*. 2002;47:629–33.

151. Mangia S, Tkáč I, Gruetter R, Van de Moortele P-F, Maraviglia B, Uğurbil K. Sustained neuronal activation raises oxidative metabolism to a new steady-state level: evidence from ¹H NMR spectroscopy in the human visual cortex. *J Cereb blood flow Metab.* 2007 May;27(5):1055–63.
152. Lin Y, Stephenson MC, Xin L, Napolitano A, Morris PG. Investigating the metabolic changes due to visual stimulation using functional proton magnetic resonance spectroscopy at 7 T. *J Cereb blood flow Metab.* 2012 Aug;32(8):1484–95.
153. Schaller B, Mekle R, Xin L, Kunz N, Gruetter R. Net increase of lactate and glutamate concentration in activated human visual cortex detected with magnetic resonance spectroscopy at 7 Tesla. *J Neurosci Res.* 2013 Aug;91(8):1076–83.
154. Bednařík P, Tkáč I, Giove F, DiNuzzo M, Deelchand DK, Emir UE, et al. Neurochemical and BOLD responses during neuronal activation measured in the human visual cortex at 7 Tesla. *J Cereb Blood Flow Metab.* 2015;31(35):1–10.
155. Klose U. In vivo proton spectroscopy in presence of eddy currents. *Magn Reson Med.* 1990;14:26–30.
156. Provencher SW. Automatic quantitation of localized in vivo ¹H spectra with LCMoDel. *NMR Biomed.* 2001;14:260–4.
157. Schaller B, Xin L, Gruetter R. Is the macromolecule signal tissue-specific in healthy human brain? A ¹H-MRS study at 7 tesla in the occipital lobe. *Magn Reson Med.* 2014;72:934–40.
158. Kreis R, Ernst T, Ross BD. Absolute quantification of water and metabolites in the human brain. II. Metabolite concentrations. *J Magn Reson Ser B.* 1993;102:9–19.
159. Prichard J, Rothmans D, Novotny E, Petroff O, Kuwabara T, Avisonf M, et al. Lactate rise detected by ¹H NMR in human visual cortex during physiological stimulation. *Proc Natl Acad Sci U S A.* 1991;88(July):5829–31.
160. Boucard CC, Mostert JP, Cornelissen FW, De Keyser J, Oudkerk M, Sijens PE. Visual stimulation, ¹H MR spectroscopy and fMRI of the human visual pathways. *Eur Radiol.* 2005;15:47–52.
161. Merboldt KD, Bruhn H, Hanicke W, Michaelis T, Frahm J. Decrease of glucose in the human visual cortex during photic stimulation. *Magn Reson Imaging.* 1992;25:187–94.
162. Sandor P, Dydak U, Schoenen J, Kollias S, Hess K, Boesiger P, et al. MR-spectroscopic imaging during visual stimulation in subgroups of migraine with aura. *Cephalgia.* 2005;25:507–18.
163. Nieto FJ, Young TB, Lind BK, Shahar E, Samet JM, Redline S, et al. Association of sleep-disordered breathing, sleep apnea, and hypertension in a large community-based study. *J Am Med Assoc.* 2000;284(14):1829–36.

164. Epstein LJ, Kristo D, Strollo PJ, Friedman N, Malhotra A, Patil SP, et al. Clinical Guideline for the Evaluation, Management and Long-term Care of. *J Clin Sleep Med*. 2009;5(3):263–76.
165. Parra O, Arboix A, Bechich S, García-erolas L, Montserrat JM, Lopez JA, et al. Time Course of Sleep-related Breathing Disorders in First-Ever Stroke or Transient Ischemic Attack. *Am J Respir Crit Care Med*. 2000;161:375–80.
166. Woorons X, Gamelin FX, Lamberto C, Pichon A, Richalet JP. Swimmers can train in hypoxia at sea level through voluntary hypoventilation. *Respir Physiol Neurobiol*. 2014;190:33–9.
167. Peacock AJ. Oxygen at high altitude. *Br Med J*. 1998;317:1063–6.
168. Shimojyo S, Scheinberg P, Kogure K, Reinmuth O. The effects of graded hypoxia upon transient cerebral blood flow and oxygen consumption. *Neurology*. 1968;18:127–33.
169. Rostrup E, Larsson HBW, Born AP, Knudsen GM, Paulson OB. Changes in BOLD and ADC weighted imaging in acute hypoxia during sea-level and altitude adapted states. *Neuroimage*. 2005 Dec;28(4):947–55.
170. Tuunanen PI, Murray IJ, Parry NRA, Kauppinen RA. Heterogeneous oxygen extraction in the visual cortex during activation in mild hypoxic hypoxia revealed by quantitative functional magnetic resonance imaging. *J Cereb blood flow Metab*. 2006;26:263–73.
171. Tuunanen PI, Vidyasagar R, Kauppinen RA. Effects of mild hypoxic hypoxia on poststimulus undershoot of blood-oxygenation-level-dependent fMRI signal in the human visual cortex. *Magn Reson Imaging*. 2006;24(8):993–9.
172. Tuunanen PI, Kauppinen RA. Effects of oxygen saturation on BOLD and arterial spin labelling perfusion fMRI signals studied in a motor activation task. *Neuroimage*. 2006;30(1):102–9.
173. Shen Y, Ho Y-CL, Vidyasagar R, Balanos G, Golay X, Pu IM, et al. Gray matter nulled and vascular space occupancy dependent fMRI response to visual stimulation during hypoxic hypoxia. *Neuroimage*. 2012;59(4):3450–6.
174. Smith ZM, Krizay E, Guo J, Shin DD, Scadeng M, Dubowitz DJ. Sustained high-altitude hypoxia increases cerebral oxygen metabolism. *J Appl Physiol*. 2012;677:11–8.
175. Simon AB, Smith Z, Buxton RB, Dubowitz DJ. Application of quantitative, multimodal fMRI to the estimation of the cerebral metabolic response to CO₂ and a visual stimulus in hypoxia. In: *Proceedings of the International Society of Magnetic Resonance in Medicine*. 2015. p. 212.
176. Vidyasagar R, Kauppinen R. ³¹P magnetic resonance spectroscopy study of the human visual cortex during stimulation in mild hypoxic hypoxia. *Exp brain Res*.

2008 May;187(2):229–35.

177. Golay X, Petersen ET, Hui F. Pulsed star labeling of arterial regions (PULSAR): a robust regional perfusion technique for high field imaging. *Magn Reson Med.* 2005 Jan;53(1):15–21.
178. Chen JJ, Pike GB. Global cerebral oxidative metabolism during hypercapnia and hypocapnia in humans: implications for BOLD fMRI. *J Cereb blood flow Metab.* 2010;30(6):1094–9.
179. Griffeth VEM, Blockley NP, Simon AB, Buxton RB. A New Functional MRI Approach for Investigating Modulations of Brain Oxygen Metabolism. *PLoS One.* 2013;8.
180. Lu H, Clingman C, Golay X, van Zijl PCM. Determining the longitudinal relaxation time (T1) of blood at 3.0 Tesla. *Magn Reson Med.* 2004 Sep;52(3):679–82.
181. Kim M, Ward D, Cartwright C, Kolano J, Chlebowski S, Henson LC. Estimation of jugular venous O2 saturation from cerebral oximetry or arterial O2 saturation during isocapnic hypoxia. *J Clin Monit Comput.* 2000;16:191–9.
182. Kim S-G, Ogawa S. Biophysical and physiological origins of blood oxygenation level-dependent fMRI signals. *J Cereb blood flow Metab.* 2012;32(7):1188–206.
183. Hoge RD, Atkinson J, Gill B, Crelier GR, Marrett S, Pike GB. Investigation of BOLD signal dependence on cerebral blood flow and oxygen consumption: the deoxyhemoglobin dilution model. *Magn Reson Med.* 1999 Nov;42(5):849–63.
184. Fowler B, Kelso B. The effects of hypoxia on components of the human event-related potential and relationship to reaction time. *Aviat Sp Environ Med.* 1992;63(6):510–6.
185. Fowler B, Prlic H. A comparison of visual and auditory reaction time and P300 latency thresholds to acute hypoxia. *Aviat Sp Environ Med.* 1995;66(7):645–50.
186. Fowler B, Nathoo A. Slowing due to acute hypoxia originates early in the visual system. *Aviat Sp Environ Med.* 1997;68(10):886–9.
187. Schneider S, Strüder HK. Monitoring effects of acute hypoxia on brain cortical activity by using electromagnetic tomography. *Behav Brain Res.* 2009;197(2):476–80.
188. Thompson JK, Peterson MR, Freeman RD. High-resolution neurometabolic coupling revealed by focal activation of visual neurons. *Nat Neurosci.* 2004;7(9):919–20.
189. Gruetter R, Tkáč I. Field mapping without reference scan using asymmetric echo-planar techniques. *Magn Reson Med.* 2000 Feb;43(2):319–23.
190. Emir UE, Raatz S, Mcpherson S, Hodges JS, Torkelson C, Tawfik P, et al. Noninvasive quantification of ascorbate and glutathione concentration in the elderly

human brain. *NMR Biomed.* 2011;24(7):888–94.

191. Mangia S, Tkáč I, Logothetis NK, Gruetter R, Van de Moortele P-F, Uğurbil K. Dynamics of lactate concentration and blood oxygen level-dependent effect in the human visual cortex during repeated identical stimuli. *J Neurosci Res.* 2007;85(15):3340–6.
192. Hertz L, Dienel G. Energy metabolism in the brain. *Int Rev Neurobiol.* 2002;51:1–102.
193. Semena G, Wang G. A nuclear factor induced by hypoxia via de novo protein synthesis binds to the human erythropoietin gene enhancer at a site required for transcriptional activation. *Mol Cell Biol.* 1992;12:5447–54.

APPENDIX A – ETHICS COMMITTEE APPROVAL –
UNIVERSITY OF SÃO PAULO



Universidade de São Paulo
Faculdade de Filosofia, Ciências e Letras de Ribeirão Preto
Comitê de Ética em Pesquisa

Campus de Ribeirão Preto

Of.CEtP/FFCLRP-USP/092-vjmc

Ribeirão Preto, 25 de novembro de 2013

Prezado Pesquisador,

Comunicamos a V. Sa. que o projeto de pesquisa intitulado "ESTUDO DA DINÂMICA DO ACOPLAMENTO NEUROVASCULAR E METABÓLICO EM CONDIÇÕES DE NORMÓXIA E HIPÓXIA EM SUJEITOS JOVENS SAUDÁVEIS SOB ESTIMULAÇÃO VISUAL E MOTORA" foi reanalisado pelo Comitê de Ética em Pesquisa da FFCLRP-USP, em sua 126ª Reunião Ordinária, realizada em 21.11.2013, e enquadrado na categoria: **APROVADO** (CAAE n.º 22077513.3.0000.5407).

Solicitamos que eventuais modificações ou emendas ao projeto de pesquisa sejam apresentadas ao CEP, de forma sucinta, identificando a parte do projeto a ser modificada e suas justificativas, e que relatórios parciais e final sejam entregues, via Plataforma Brasil, conforme os itens X.1.3.d e XI.2.d, da Res. CNS nº 466/2012.

Atenciosamente,


Prof.ª Dr.ª ANDRÉIA SCHMIDT
Coordenadora

Ao Senhor
Felipe Rodrigues Barreto
Programa de Pós-Graduação em Física Aplicada à Medicina e Biologia da FFCLRP
USP

C/C:
Prof. Dr. Carlos Ernesto Garrido Salmon
Departamento de Física da FFCLRP USP

CEP - Comitê de Ética em Pesquisa da FFCLRP USP
Fone: (16) 3602-4811
Fax: (16) 3633-2660 (direto) ou 3633-5015
Avenida Bandeirantes, 3900 - bloco 3 - sala 16 - 14040-901 - Ribeirão Preto - SP - Brasil
Homepage: <http://www.ffclrp.usp.br> - e-mail: coetp@ffclrp.usp.br

APPENDIX B – ETHICS COMMITTEE APPROVAL –
UNIVERSITY OF MINNESOTA

UNIVERSITY OF MINNESOTA

Twin Cities Campus

*Human Research Protection Program
Office of the Vice President for Research*

*D528 Mayo Memorial Building
420 Delaware Street S.E.
MMC 820
Minneapolis, MN 55455
Office: 612-626-5654
Fax: 612-626-6061
E-mail: irb@umn.edu or ibc@umn.edu
Website: <http://research.umn.edu/subjects/>*

July 24, 2015

Silvia Mangia
Magnetic Resonance Research
Mayo MMC 292 C8292B
420 Delaware St SE
Minneapolis, MN 55455

RE: "Metabolic changes in the activated human visual cortex during mild hypoxia"
IRB Code Number: 1503M65382

Dear Dr. Mangia:

The Institutional Review Board (IRB) received your response to its stipulations. Since this information satisfies the federal criteria for approval at 45CFR46.111 and the requirements set by the IRB, final approval for the project (protocol date July 22, 2015) is noted in our files. Upon receipt of this letter, you may begin your research.

IRB approval of this study includes the consent form dated July 22, 2015 and recruitment materials received June 24, 2015.

The IRB has made a determination of non-significant risk (NSR) regarding the use of the devices in this study. Any changes to the study device require prospective IRB review and approval. Researchers conducting NSR research must follow the abbreviated IDE requirements at 21 CFR 812.2(b).

The IRB would like to stress that subjects who go through the consent process are considered enrolled participants and are counted toward the total number of subjects, even if they have no further participation in the study. Please keep this in mind when calculating the number of subjects you request. This study is currently approved for 30 subjects. If you desire an increase in the number of approved subjects, you will need to make a formal request to the IRB.

On July 16, 2015 the IRB approved the referenced study through July 14, 2016 inclusive.

The Assurance of Compliance number is FWA00000312 (Fairview Health Systems Research FWA00000325, Gillette Children's Specialty Healthcare FWA00004003). Research projects are subject to continuing review and renewal. You will receive a report form two months before the expiration date. If you would like us to send certification of approval to a funding agency, please tell us the name and address of your contact person at the agency.

As Principal Investigator of this project, you are required by federal regulations to:

*Inform the IRB of any proposed changes in your research that will affect human subjects, changes should not be initiated until written IRB approval is received.

APPENDIX C – GRANT AWARD LETTER

UNIVERSITY OF MINNESOTA

Twin Cities Campus

*Clinical and Translational Science Institute
Academic Health Center*

*717 Delaware St. S.E.
Minneapolis, MN 55414
Office: 612-625-2874 (CTSI)
Fax: 612-625-2695
E-mail: ctsi@umn.edu
<http://www.ctsi.umn.edu>*

April 10, 2015

Dear Dr. Mangia:

On behalf of the Office of Discovery and Translation (ODAT), we are pleased to inform you that your application “Metabolic changes in the activated human visual cortex during mild hypoxia,” submitted to the ODAT Translational Technologies and Resources (TTR) Core Usage Program, has been selected for funding.

For your information, we are enclosing a copy of the critique of your application. Each application was assigned to internal peer reviewers who were asked to consider the translational potential, feasibility and the likelihood of obtaining future extramural funding. Applications were also assessed by the TTR leadership team using these criteria.

As stated in the funding agreement, funded investigators are required to use funds as outlined in the application and agreed upon by the appropriate Core Director. Funding cannot be released until all necessary regulatory approvals have been obtained. Thus, if you have not yet received any necessary IRB, IACUC and/or IBC approval, please initiate this process to avoid a delay in funding.

We wish to offer our sincerest congratulations and look forward to a productive partnership that will assist your team in generating data to support an external grant submission or patent application.

Sincerely,



Christopher Pennell, PhD
TTR Director
Office of Discovery and Translation
Clinical and Translational Science Institute
University of Minnesota



Tucker W. LeBien, PhD
Vice Dean for Research – Medical School
Associate Vice President for Research – AHC
Professor of Laboratory Medicine/Pathology
University of Minnesota Medical School